Measurement of the Spin Asymmetry $A_{||}$ in the Photoproduction of High-p_T Hadron Pairs

by

Jeffery William Martin

B.Sc. (Hons.) Physics
University of Manitoba
June 1995

Submitted to the Department of Physics
in partial fulfillment of the requirements for the degree of

Doctor of Philosophy

at the

MASSACHUSETTS INSTITUTE OF TECHNOLOGY

February 2000

Author ....
Department of Physics
October 4, 1999

Certified by ....
Professor Richard G. Milner
Professor of Physics
Thesis Supervisor

Accepted by ....
Professor Thomas J. Greytak
Professor
Associate Department Head for Education

Measurement of the Spin Asymmetry $A_{||}$ in the Photoproduction of High-p_T Hadron Pairs

by

Jeffery William Martin

Submitted to the Department of Physics
on October 4, 1999, in partial fulfillment of the
requirements for the degree of
Doctor of Philosophy

Abstract

A measurement of the spin asymmetry $A_{||}$ in the quasi-real photoproduction of high-p_T hadron pairs is presented. Data were accumulated by the HERMES experiment in 1996 and 1997 using a polarized atomic hydrogen target internal to the 27.6 GeV polarized HERA positron beam. At high transverse hadron momenta, the data show a negative asymmetry: for h^+h^- pairs with $p_T^{h_1} > 1.5$ GeV/c and $p_T^{h_2} > 1.0$ GeV/c, the measured asymmetry is $A_{||} = -0.28 \pm 0.12$ (stat.) $\pm$ 0.02 (syst.). This negative value is in contrast to the positive asymmetries typically measured in deep-inelastic scattering from protons. When interpreted in a LO QCD model implemented in the PYTHIA Monte Carlo generator, a value of the gluon polarization in the nucleon $\Delta G/G$ of 0.41 ± 0.18 (stat.) ± 0.03 (exp. syst.)$^{+0.42}_{-0.06}$ (model) is extracted at $\langle x_G \rangle = 0.17$ and scale $\langle \hat{p}_T^2 \rangle = 2.1$ (GeV/c)^2. Several possibilities for unpolarized models of the data are considered, and the effects on $\Delta G/G$ are quantified in a model dependence error bar: $\delta(\Delta G/G)_{\mathrm{model}} =^{+0.42}_{-0.06}$. The result compares favorably with QCD fits of the same quantity.

Thesis Supervisor: Professor Richard G. Milner
Title: Professor of Physics

Acknowledgments

Many people contributed to the concept of this thesis and the drafting of the related paper. The most important one to me was my supervisor, Richard Milner. He allowed me the freedom to explore many different analysis topics at the HERMES experiment. One of the topics I looked into resulted quite nicely in this thesis. I should also thank the other people who put some work into this topic. Moskov Amarian came up with the original concept. I credit Arthur Mateos with setting me on Moskov's trail, and getting me interested in the subject. I thank Stephan Brons and Slava Korotkov for pointing out the weaknesses in my analysis. Antje Brüll, Ed Kinney, Naomi Makins, Andreas Schäfer, Bob Redwine, and Klaus Rith provided me with significant guidance in my exploration of the analysis. All these people also helped significantly in drafting the paper. I'd like to acknowledge my thesis committee: Bob Jaffe for useful discussions, and June Matthews for saving me by joining the committee the day before the defense.

I would like to thank all my friends from my first year at MIT, without whom I would not have survived, but mainly: Andrew Barger, Ben Brau, Winthrop Brown, Oliver de Wolfe, David Kokorowski, Kieran Holland, Allen Hunt, Jim McBride, and Dan Ripin. The weekly Stat. Mech. study sessions were a pain, but we're all still alive, eh? Don't forget: I am Nihat!

Life in Hamburg was made so much more livable by all the wonderful, tolerant people on the experiment. I would like to thank in particular everyone who ever attended an offsite meeting. Now I will list my drinking buddies that I met at HERMES: Elke Aschenauer, Balijeet Bains, Marc Beckmann, Johan Blouw, Maurice Bouwhuis, Pam Chumney, Dirk de Schepper, James Ely, Brendan Fox, MAF, Phil Geiger, Holger Ihssen, Ralf Kaiser, Hauke Kolster, Naomi Makins, Mike McAndrew, Felix Menden, Falk Meiβner, Andreas Most, Philip Oelwein, Brynnen Owen, Steve Pate, Greg Rakness, Gunar Schnell, Chiara Simani, Joachim Seibert, Jim Stewart, Hugh Tallini, Michael Tytgat, Jeroen van Hunen, Manuella Vincter, Jan Visser, Erik Volk, and, saving the best for last, Wolfgang Wander. To those who didn't make the usual drinking list: Don't feel bad, it just means that I actually respect you.

Coming back to polish my analysis at MIT, I was triumphantly reunited with all my MIT friends, and crammed into an office with three other HERMES students (Taeksu Shin, Mark Sutter, Bryan Tipton) and one LADS student (Nik Gregory). Mostly, I remember all the wonderful physics discussions we had, ... mostly. Keen insight was often added by Arthur Mateos, Kevin McIlhany, and Antje Brüll. Actually, we all mainly just watched South Park on my computer and went to coffee and to the bar together. Our volleyball team did pretty good this past summer, and I hope that Dipangkar Dutta, Bill Franklin, Doug Hasell, and Vitaliy Ziskin will agree to make peace and speak to each other again, so that they can continue summer volleyball in the LNS. I feel that I must also thank Joanne Gregory. Despite the fact that she constantly reamed me out for not getting my travel vouchers in on time, she saved me on more than one occasion when I really needed a hand.

Throughout my stay at MIT and my travels abroad, my parents have called every week to make sure that I was still alive. They saved me from freaking out over several crises while away from home. I regret that my travels have not taken me through Crystal City, Manitoba a few more times. I thank my brothers and sister, Steve, Eric, and Jill, and my other friends back in Manitoba for staying in touch, even though I have often been hard to reach.

Lastly and most importantly, I would like to acknowledge my girlfriend Melanie Schachter. I gratefully thank her for her love and devotion over these past four years. I cannot wait to start our new life together in California. Hurry up and graduate, Melanie, so that the daily barrage of email can finally stop!

Contents

Chapter 1

Theory

The use of electromagnetic probes to study the structure of the strong interaction has become an important technique in the last century. An example is deep-inelastic scattering (DIS), where high-energy leptons are scattered from targets to study the structure of nucleons (protons and neutrons). Using inclusive DIS, where only the scattered lepton is considered in the final state, it has been experimentally proven that there are pointlike constituents inside the nucleon (quarks), that these constituents are spin-1/2, and that only a fraction (of order 30-50%) of the nucleon momentum and spin are carried by these constituents.

Through precise measurements of the inclusive DIS cross section, it has been inferred from scaling violations that the missing piece of the nucleon momentum is carried by gluons. This has been confirmed by measurements of the production of current jets in DIS and photoproduction experiments. This mechanism gives sensitivity to the leading-order (LO) QCD photon gluon fusion (PGF) diagram, allowing a direct measurement of the gluon structure function $G(x)$.

The reason that only a fraction of the nucleon spin is carried by quarks remains a mystery, although from analogy with the above measurements, it seems reasonable that the gluons could contribute significantly to the proton spin. Arguments based on the axial anomaly support this view. Consequently, recent theoretical work and several experimental proposals have concentrated on ways to measure the polarized gluon distribution in the nucleon, $\Delta G(x)$ [1, 2, 3]. One way to infer $\Delta G(x)$ is by a measurement of the scaling violation of the polarized structure functions. However, this extraction requires a precise knowledge of the inclusive DIS asymmetry over a broad range of x and Q^2. The presently available data on polarized inclusive DIS is insufficient to extract $\Delta G(x)$, though there is some indication for the integral ΔG to be positive [4, 5, 6]. A calculation of ΔG in the MIT bag model has suggested that ΔG could be negative [7].

A way to measure $\Delta G(x)$ directly is via the PGF process, using jets, as for the unpolarized momentum measurements described above. In fixed target experiments, jet separation is only possible at very high energies. At lower energies, single high p_T hadrons must be substituted for jets [8]. A significant reduction in the statistical uncertainties can be obtained by including data not only from DIS, but also from quasi-real photoproduction. However, the inclusion of such physics processes significantly increases the level of difficulty in understanding the interpretation of the result. Several phenomenological studies of the use of high p_T meson photoproduction as a probe of ΔG have been conducted [9, 10].

In this chapter, a review of the techniques of (spin-dependent) DIS and semi-inclusive DIS is presented. Possible ways to measure $\Delta G/G$ by measuring spin asymmetries in high-energy lepton-nucleon collisions are explored. The limit of quasi-real photoproduction ($Q^2 \to 0$) is taken, and spin asymmetries in high-p_T photoproduction are related to the gluon polarization in the nucleon $\Delta G(x)$.

1.1 Deep-Inelastic Scattering

Deep-inelastic scattering of leptons from nucleons can be approached from a phenomenological point of view resulting in four arbitrary structure functions: two for the polarized case and two for the unpolarized case. The assumption of point-like charged constituents in the nucleon leads to the effect of scaling in these structure functions. Use of the quark-parton model allows for a phenomenological interpretation of these structure functions in terms of contributions from the quark species. Semi-inclusive DIS is introduced as a method to separate the contributions of the different quarks using the charge of a produced hadron to tag the quark flavor.

1.1.1 The cross section for the inclusive process

The leading-order Feynman diagram describing DIS is shown in Fig. 1-1. The following kinematic quantities are used to described the scattering:

$$q \equiv k - k' = (\nu; \mathbf{q}) \tag{1.1}$$

$$Q^2 \equiv -q^2 = 2EE'(1 - cos\theta) \tag{1.2}$$

$$x \equiv \frac{-q^2}{2p \cdot q} = \frac{Q^2}{2M\nu} \tag{1.3}$$

$$y \equiv \frac{p \cdot q}{p \cdot k} = \frac{\nu}{E} \tag{1.4}$$

$$W^2 \equiv (p+q)^2 = M^2 + 2M\nu - Q^2 \tag{1.5}$$

where the final equality in each of the above equations holds in the lab frame. Here, the four-momenta k, k', q, and p are those of the incident electron, scattered electron, virtual photon, and target proton, respectively. The Lorentz invariants which are calculated are: Q^2, the negative-square four-momentum of the virtual photon; x, Bjorken's scaling variable; y, the fractional energy carried by the virtual photon; and

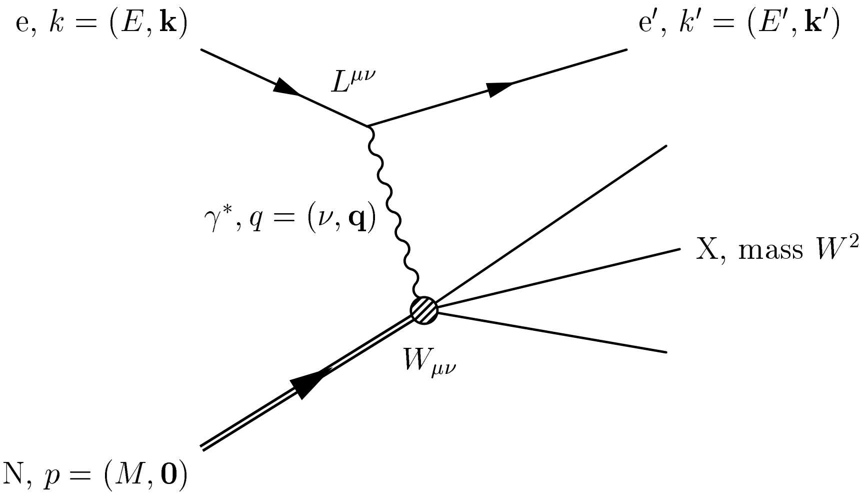

Figure 1-1: lepton e scatters from target nucleon N exchanging virtual photon γ^*

W^2, the total hadronic energy of the final state. The experimentally determined lab frame variables are: E, the energy of the incident electron; E', the energy of the scattered electron; and θ, the scattering angle. M is the proton mass.

Scattering is expected to occur from quarks when the energy of the final state exceeds all strong hadronic resonances ($W^2 > 4$ GeV^2) and the momentum transfer exceeds the hadronic QCD momentum scale, Λ_{QCD}: $Q^2 \gg \Lambda_{QCD}^2 \simeq (300\ \text{MeV})^2$. The DIS regime of the scattering process is usually defined by the following requirements:

$$\begin{cases} Q^2 & > \quad 1\ \text{GeV}^2 \\ W^2 & > \quad 4\ \text{GeV}^2. \end{cases} \tag{1.6}$$

The cross section for DIS is given by [11]:

$$\frac{d^2\sigma}{dE'd\Omega} = \frac{\alpha^2}{Q^4}\frac{E'}{E}L^{\mu\nu}W_{\mu\nu}. \tag{1.7}$$

The leptonic tensor $L_{\mu\nu}$ can be calculated exactly by assuming leptons are point-like fermions. A first principles calculation of the hadronic tensor $W_{\mu\nu}$ requires a thorough understanding of the structure of the nucleon in QCD. However, fundamental symmetries limit the functional form to [12]:

$$\begin{aligned} W_{\mu\nu} &= F_1(x,Q^2)\left[-g_{\mu\nu}+\tfrac{q_\mu q_\nu}{q^2}\right] \\ &+ \tfrac{F_2(x,Q^2)}{(p\cdot q)}\left[p_\mu-\tfrac{(p\cdot q)}{q^2}q_\mu\right]\left[p_\nu-\tfrac{(p\cdot q)}{q^2}q_\nu\right] \\ &+ i\tfrac{g_1(x,Q^2)}{p\cdot q}\epsilon_{\mu\nu\gamma\delta}q^\gamma s_n^\delta \\ &+ i\tfrac{g_2(x,Q^2)}{(p\cdot q)^2}\epsilon_{\mu\nu\gamma\delta}q^\gamma((p\cdot q)s_n^\delta-(s_n\cdot q)p^\delta), \end{aligned} \tag{1.8}$$

where s_n is the four-spin of the nucleon and F_1, F_2, g_1, and g_2 are structure functions of the nucleon. At this point, the structure functions are arbitrary functions of the two independent variables in the problem, x and Q^2.

Averaging over initial nucleon polarization gives the cross section for the unpolarized process [12]:

$$\frac{d^2\sigma}{dxdQ^2}=\frac{4\pi\alpha^2}{Q^4x}\left[\left(1-y-\frac{Mxy}{2E}\right)F_2(x,Q^2)+xy^2F_1(x,Q^2)\right]. \tag{1.9}$$

In the case that beam and target are polarized longitudinally, the spin-dependent part of the cross section is accessed:

$$\frac{d^2\Delta\sigma}{dxdQ^2}=\frac{4\pi\alpha^2}{MExQ^2}\left[\left(2-y-\frac{Mxy}{E}\right)g_1(x,Q^2)-\frac{2Mx}{E}g_2(x,Q^2)\right], \tag{1.10}$$

where $\Delta\sigma=\sigma^{\uparrow\downarrow}-\sigma^{\uparrow\uparrow}$ is the difference between the cross section when the target is polarized anti-parallel to the beam polarization direction and the cross section when the target is polarized parallel to the beam polarization direction.

Experimentally, the spin asymmetry $A_{||}$ is measured:

$$A_{||}=\frac{d\sigma^{\uparrow\downarrow}-d\sigma^{\uparrow\uparrow}}{d\sigma^{\uparrow\downarrow}+d\sigma^{\uparrow\uparrow}}=\frac{\frac{d^2\Delta\sigma}{dxdQ^2}}{2\frac{d^2\sigma}{dxdQ^2}}=D(A_1+\eta A_2) \tag{1.11}$$

where A_1 and A_2 are virtual photon-nucleon asymmetries, related to the usual structure functions as follows [12]:

$$A_1(x, Q^2) = \frac{g_1(x, Q^2) - \gamma^2 g_2(x, Q^2)}{F_1(x, Q^2)} \tag{1.12}$$

$$A_1(x, Q^2) = \gamma \frac{g_1(x, Q^2) + g_2(x, Q^2)}{F_1(x, Q^2)} \tag{1.13}$$

. The quantities γ, D, and η are kinematical factors. In the Bjorken limit of large Q^2, γ and η approach zero. Only D, the so-called virtual photon depolarization factor, remains:

$$D(y) \simeq \frac{y(2-y)}{2(1-y)(1+R) + y^2} \tag{1.14}$$

where R is the ratio of longitudinal to transverse virtual photon-nucleon cross sections, related to F_1 and F_2 by:

$$R(x, Q^2) = \frac{1+\gamma^2}{2xF_1(x, Q^2)} F_2(x, Q^2) - 1. \tag{1.15}$$

In the quark parton model, and experimentally, R is found to be close to zero. Therefore, a simplified expression for $D(y)$ is often used:

$$D(y) \simeq \frac{y(2-y)}{2(1-y) + y^2}. \tag{1.16}$$

In the Bjorken limit, the relationship of $A_{||}$ to g_1 also simplifies:

$$A_{||} \simeq D(y) \frac{g_1(x, Q^2)}{F_1(x, Q^2)}. \tag{1.17}$$

1.1.2 The interpretation of g_1 in the quark parton model

In the quark parton model (QPM), DIS is described as an incoherent superposition of virtual photon absorption on quarks. In the most naive form of the model, the quark momentum distributions are only a function of the Bjorken scaling variable x defined in the previous section. In the QCD-improved QPM, this scaling is broken by the presence of gluons.

In the naive QPM, the hadronic tensor $W_{\mu\nu}$ may be derived based on the (spin-dependent) x distributions of the quarks. Consider a longitudinally polarized photon incident on a quark. Since the photon has spin $S = 1$, $S_z = \pm 1$, and the quark has spin $S = 1/2$, the quark cannot absorb the photon unless its spin is opposite to that of the photon (see Fig. 1-2). Hence, longitudinally polarized photons only scatter from

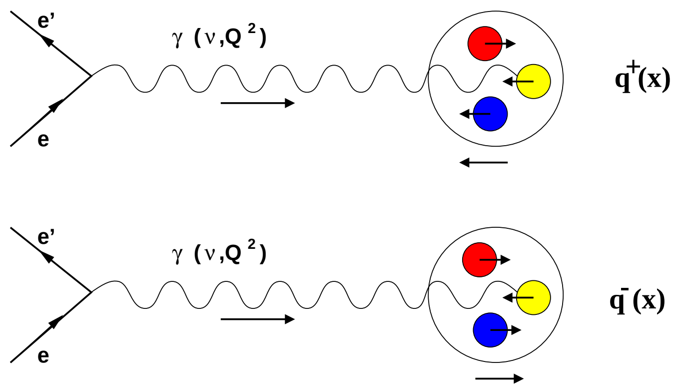

Figure 1-2: A simple QPM explanation of the sensitivity of polarized DIS to the polarized quark distributions

quarks that are polarized opposite to the photon polarization direction, independent of the polarization of the nucleon. Reversing the polarization of the nucleon allows a measurement of the difference in the number of quarks aligned with the spin of the nucleon and those that are anti-aligned.

The nucleon structure function is then obtained by summing over all quark flavors and spins and integrating over all momenta, weighted by the probability of such occurence in the ground state of the nucleon. Explicitly, this means:

$$\begin{aligned} F_1(x) &= \sum_f \frac{e_{q_f}^2}{2}\left(q_f^+(x) + q_f^-(x)\right) \equiv \sum_f \frac{e_{q_f}^2}{2} q_f(x) \\ F_2(x) &= 2xF_1(x) \\ g_1(x) &= \sum_f \frac{e_{q_f}^2}{2}\left(q_f^+(x) - q_f^-(x)\right) \equiv \sum_f \frac{e_{q_f}^2}{2} \Delta q_f(x) \\ g_2(x) &= 0. \end{aligned} \tag{1.18}$$

1.1.3 Decomposition of the nucleon spin

Modern experiments in spin physics strive to determine how the spin of the nucleon is distributed among its constituents. Assuming the principle of conservation of angular momentum, the following angular momentum sum rule applies:

$$\frac{1}{2} = \frac{1}{2}\left[\underbrace{\Delta u + \Delta d + \Delta s}_{\Delta\Sigma}\right] + \Delta G + L_z. \tag{1.19}$$

Here, $\Delta\Sigma$ is the spin carried by the quarks, ΔG the spin carried by the gluons, and L_z the angular momentum carried by the quarks and gluons.

1.1.4 Semi-inclusive measurements

Present experiments study semi-inclusive DIS. Semi-inclusive in this context means that one or more hadrons are detected in the final state in addition to the scattered lepton. The observation of hadrons produced in the DIS reaction gives valuable information about which type of quark was struck in the process. For example, a high momentum π^+ observed in the final state is a strong indication that a u quark was struck in the collision, whereas a high momentum π^- means that a d quark was likely struck. In reality, the hadronization process complicates things considerably, and probabilities for u and d quarks to "fragment" into π^+ and π^- mesons must be measured.

The cross-section for semi-inclusive DIS, normalized to the inclusive cross-section, can be related to parton distributions in the QPM by:

$$\frac{1}{\sigma_{tot}}\frac{d\sigma^h(x,Q^2,z)}{dz} = \frac{\sum_f e_{q_f}^2 q_f(x,Q^2) D_{q_f}^h(z,Q^2)}{\sum_f e_{q_f}^2 q_f(x,Q^2)} \ . \tag{1.20}$$

The "fragmentation function" $D_{q_f}^h(z,Q^2)$ represents the probability that a quark of type q_f fragments into a hadron of type h. The $D_{q_f}^h(z,Q^2)$ are functions of the energy fraction carried by the detected hadron,

$$z = \frac{E_h}{\nu}. \tag{1.21}$$

Factorization in semi-inclusive (polarized) deep-inelastic scattering [13] implies the independence of the fragmentation process from the kinematics of the photon-quark vertex (i.e. $D_{q_f}^h(z,Q^2)$ doesn't depend on x). However, similar to the factorization of the quark structure functions, the factorization scale Q^2 must be included as an argument in the fragmentation function; however, $D_{q_f}^h(z,Q^2)$ has only a logarithmic dependence on this scale.

In polarized DIS, the semi-inclusive asymmetry probes the helicity difference parton distributions, $\Delta q(x)$, in a linearly independent way from the inclusive asymmetry:

$$A_{||}^h = D(y) \times A_1^h(x,z) = \frac{\sum_f e_{q_f}^2 \Delta q_f(x,Q^2) D_{q_f}^h(z,Q^2)}{\sum_{f'} e_{q_{f'}}^2 q_{f'}(x,Q^2) D_{q_{f'}}^h(z,Q^2)} \times D(y) \tag{1.22}$$

where $D(y)$, the virtual photon depolarization factor, should not be confused with the fragmentation functions $D_{q_f}^h(z,Q^2)$. Thus, the $\Delta\Sigma$ piece of equation (1.19) can be separated into contributions from different quark flavors by observing different hadrons in the final state.

1.2 Measuring the Gluon Polarization

Several experimental techniques are envisioned in lepton-nucleon scattering to access information about the gluon contribution to the nucleon spin ΔG. They can be divided into two groups. One method is to use the scaling violation of the polarized inclusive structure functions mentioned in the previous sections. The Q^2 evolution is due to the presence of gluons. The other method is to attempt isolation of the photon-gluon fusion diagram. Again, there exist two ways to do this: charm production and high-p_T jet production.

1.2.1 Q^2 evolution of the polarized structure functions

The evolution of the quark distribution functions is due to the presence of gluons. The evolution between two momentum scales can be calculated via perturbative QCD. The structure functions themselves cannot be calculated perturbatively.

In leading order, there are three ways in which quarks and gluons can interact (see Fig. 1-3).

(a) A quark can radiate a gluon, leaving a quark and a gluon.

(b) A gluon can create a pair of quarks.

(c) A gluon can create a pair of gluons.

The cross section for each possibility is perturbatively calculable for sufficiently large scale $Q^2 \gg \Lambda^2_{\mathrm{QCD}}$ and hence small coupling α_s. The fact that, perturbatively, quarks can create gluons and vice versa implies that the structure functions will be linked via an equation. Therefore, measuring the scale dependence of the quark structure functions will allow for an extraction of the gluon structure function.

The processes are described by the splitting kernels $P_{ab}(z)$. They represent the probability that a parton a is generated from a parton b with a momentum fraction z of

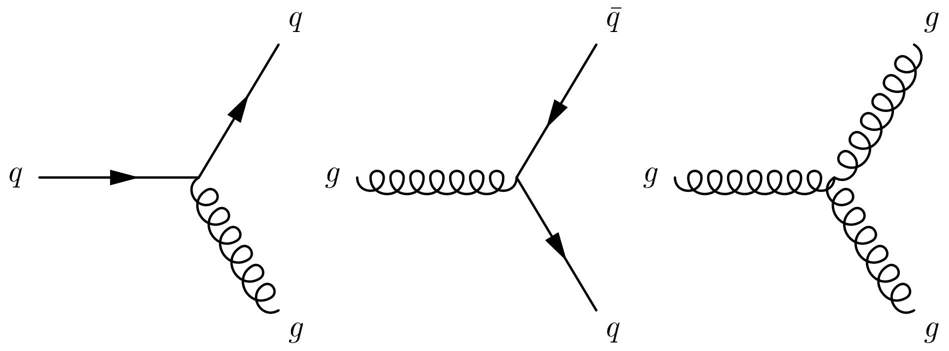

Figure 1-3: Interactions of quarks and gluons relevant to Q^2 evolution: (a) $q \to q+G$, (b) $g \to q+\bar{q}$, (c) $g \to g+g$.

the parent parton. The partons can be gluons or quarks. The DGLAP (Dockshitzer-Gribov-Lipatov-Altarelli-Parisi) evolution equations are given by [11]:

$$\frac{dq_i(x,Q^2)}{d\ln Q^2} = \frac{\alpha_s(Q^2)}{2\pi}\int_x^1 \frac{dy}{y}\left(q_i(y,Q^2)P_{qq}\left(\frac{x}{y}\right) + G(y,Q^2)P_{qG}\left(\frac{x}{y}\right)\right), \tag{1.23}$$

$$\frac{dG(x,Q^2)}{d\ln Q^2} = \frac{\alpha_s(Q^2)}{2\pi}\int_x^1 \frac{dy}{y}\left(\sum_i q_i(y,Q^2)P_{Gq}\left(\frac{x}{y}\right) + G(y,Q^2)P_{GG}\left(\frac{x}{y}\right)\right). \tag{1.24}$$

For the polarized parton distribution functions the splitting functions need merely be replaced by helicity dependent splitting kernels $P_{a\pm b\pm}$, where the $\pm$ denotes the helicity of the interacting particle. The spin-dependent DGLAP evolution equations are:

$$\frac{d\Delta q_i(x,Q^2)}{d\ln Q^2} = \frac{\alpha_s(Q^2)}{2\pi}\int_x^1 \frac{dy}{y}\left(\Delta q_i(y,Q^2)\Delta P_{qq}\left(\frac{x}{y}\right) + \Delta G(y,Q^2)\Delta P_{qG}\left(\frac{x}{y}\right)\right), \tag{1.25}$$

$$\frac{d\Delta G(x,Q^2)}{d\ln Q^2} = \frac{\alpha_s(Q^2)}{2\pi}\int_x^1 \frac{dy}{y}\left(\sum_i \Delta q_i(y,Q^2)\Delta P_{Gq}\left(\frac{x}{y}\right) + \Delta G(y,Q^2)\Delta P_{GG}\left(\frac{x}{y}\right)\right). \tag{1.26}$$

with the definition $\Delta P_{ab}(z) \equiv P_{a+b+}(z) - P_{a+b-}(z)$.

Analogous to the unpolarized case, a measurement of the Q^2 dependence of the polarized quark structure functions can, in principle, lead to a determination of the polarized gluon distribution.

Typically, the way to do this is to parameterize the polarized parton distributions at some low scale Q_0^2 with a QCD-motivated form, e.g.

$$x\Delta f(x,Q_0^2) = A_f x^{a_f}(1-x)^{b_f}(1+\gamma_f x + \rho_f x^{1/2}), \tag{1.27}$$

and then use the polarized DGLAP equations to evolve to arbitrary Q^2. In this way, one fits for the free parameters A_f, a_f, b_f, γ_f, and ρ_f for each constituent f by comparing the results of the evolution to various data on $g_1(x,Q^2)$.

The $O(\alpha_s)$ corrections relating $g_1(x,Q^2)$ to $\Delta q(x,Q^2)$ in the QCD-improved parton model have been calculated, as have the $O(\alpha_s)$ corrections to the polarized splitting functions ΔP_{ab}. This allows the improvement of the above DGLAP equations to next-to-leading order (NLO).

Recent results of various leading- and next-to-leading-order fits of the polarized structure functions will be reviewed in section 1.3.3.

1.2.2 Isolation of photon gluon fusion via charm production

Heavy quarks are produced in leading order via the PGF process shown in Fig. 1-4. The cross section for the leptoproduction of charm is given by:

$$\frac{d^4\sigma^{eN\to c\bar{c}}}{d\nu\, dQ^2\, dx\, d\hat{t}} = \Gamma(Q^2,\nu)G(x,m_c^2)\frac{d\sigma^{\gamma^* G\to c\bar{c}}}{d\hat{t}} \tag{1.28}$$

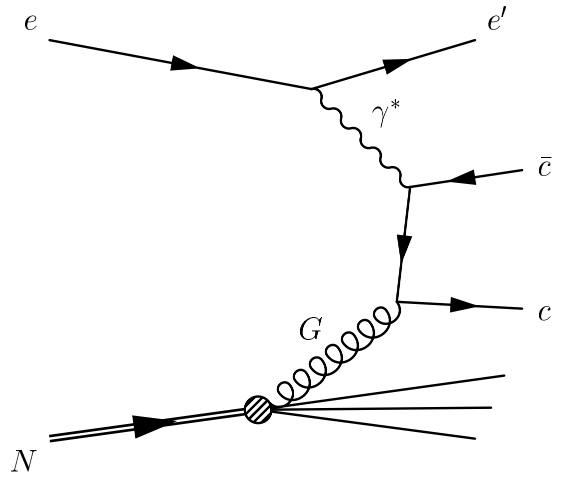

Figure 1-4: The photon gluon fusion diagram for charm leptoproduction

where $\Gamma(Q^2, \nu)$ is the virtual photon flux, $G(x)$ is the unpolarized gluon structure function (flux), and $d\sigma/d\hat{t}$ is the cross section for a virtual photon of energy ν, virtuality Q^2 to produce a heavy quark $c\bar{c}$ pair. The scale at which the gluon structure function is evaluated is set by the hardest scale in the problem, in this case the mass of the charm quark $m_c \simeq 3.5$ GeV/c^2. For this case, the photon-gluon cross section is also infrared safe. The helicity difference cross section is analogously constructed from polarized quantities:

$$\frac{d^4\Delta\sigma^{eN\to c\bar{c}}}{d\nu dQ^2 dx d\hat{t}} = \Delta\Gamma(Q^2, \nu)\Delta G(x, m_c^2)\frac{d\Delta\sigma^{\gamma^* G\to c\bar{c}}}{d\hat{t}} \tag{1.29}$$

The experimental asymmetry $A_{||}$ will be given by the ratio of these quantities, integrated over the appropriate phase space:

$$A_{||} = \frac{\int d\Delta\sigma}{\int d\sigma} \tag{1.30}$$

and is therefore sensitive to ΔG.

In current fixed target experiments, there are two channels in which charmed mesons can be detected in the final state: J/ψ and D meson production. Both mesons have been used to determine the unpolarized gluon distribution in the nucleon [14, 15, 16, 17, 18, 19].

D-meson photoproduction

The photoproduction of D mesons is believed to be the least model-dependent method to determine $\Delta G/G$. The D meson, like the pion, is a pseudoscalar, which means that its production may be described simply through the addition of a fragmentation function to the cross-sections and asymmetries described in the section above. For example, for the production of a D^0 meson, the following relations apply:

$$\frac{d^5\Delta\sigma^{eN\to \mathrm{D}X}}{d\nu dQ^2 dx d\hat{t} dz} = \frac{d^4\Delta\sigma^{eN\to c\bar{c}X}}{d\nu dQ^2 dx d\hat{t}} D_c^{\mathrm{D}^0}(z) + \frac{d^4\Delta\sigma^{eN\to \bar{c}cX}}{d\nu dQ^2 dx d\hat{t}} D_{\bar{c}}^{\mathrm{D}^0}(z). \tag{1.31}$$

One normally detects D^0 and $\bar{\mathrm{D}}^0$ mesons in the $\mathrm{K}^+\pi^-$ and $\mathrm{K}^-\pi^+$ decay channels, respectively. However, these decay channels are in general subject to a significant combinatorial background from non-resonant $\mathrm{K}\pi$ production (see e.g. [20]).

A way to overcome this problem is to use the method of "D^* tagging" to enhance the signal to noise ratio [17, 15, 19]. In this method, one detects an additional soft pion in the final state, related to the decay $\mathrm{D}^* \to \mathrm{D}\pi$. Placing a cut on the energy of this soft pion, or equivalently the mass difference $m(\mathrm{D}^*) - m(\mathrm{D})$ significantly reduces the background from other non-charm processes.

J/ψ photoproduction

Due to the fact the the J/ψ meson is a neutral vector meson, the question of how it is produced becomes more complicated, since it may also be produced elastically and inelastically through diffractive processes. It has been shown that in the elastic case, even if the dominant diffractive production mechanism is perturbative two gluon exchange, the spin asymmetry is expected to be zero [21, 22]. The same result is naively expected from VMD considerations assuming s-channel helicity conservation

(SCHC) [23], which has been found to be obeyed in experiments studying elastic J/ψ photoproduction [24].

Indeed, even if one can remove the elastic background, two competing models exist for the method in which inelastic J/ψ's are produced. These are the Color Singlet Mechanism and the Color Octet Mechanism. Which mechanism dominates determines the sensitivity to $\Delta G/G$ [1].

The inclusive J/ψ asymmetry measured at HERMES (dominated by elastic photoproduction), though of limited statistical precision, has been found to be consistent with zero [25].

1.2.3 A simple phenomenological model of high-p_T hadron leptoproduction in LO QCD

It is useful to consider a simple phenomenological model of high-p_T hadron leptoproduction, in order to get a feeling for how the different processes contribute to the cross section. It is expected that for sufficiently high p_T at fixed target energies that direct photon processes will dominate cross section. The term "direct processes" refers to the two subprocess types pictured schematically in Fig. 1-5: photon gluon fusion (PGF) and the QCD Compton effect (QCDC).

Assuming the production of two high-p_T hadrons h_1 and h_2 to be dominated by direct processes, and that each hadron is a part of each of the two forward jets produced in such processes, the cross section may be written as:

$$\begin{aligned}
\frac{d^6\sigma^{eN\to h_1h_2X}}{d\nu dQ^2dxd\hat{t}dz_1dz_2} &= \frac{d^6\sigma^{eN\to h_1h_2X}_{\text{PGF}}}{d\nu dQ^2dxd\hat{t}dz_1dz_2} + \frac{d^6\sigma^{eN\to h_1h_2X}_{\text{QCDC}}}{d\nu dQ^2dxd\hat{t}dz_1dz_2} \\
&= \Gamma(Q^2,\nu)\left[\sum_q G(x,\hat{p}_T^2)\frac{d\sigma^{\gamma^*G\to q\bar{q}}}{d\hat{t}}\left(D_q^{h_1}(z_1)D_{\bar{q}}^{h_2}(z_2)+D_{\bar{q}}^{h_1}(z_1)D_q^{h_2}(z_2)\right)\right. \\
&\qquad \left. +\sum_q q(x,\hat{p}_T^2)\frac{d\sigma^{\gamma^*q\to Gq}}{d\hat{t}}\left(D_q^{h_1}(z_1)D_G^{h_2}(z_2)+D_G^{h_1}(z_1)D_q^{h_2}(z_2)\right)\right]. \qquad (1.32)
\end{aligned}$$

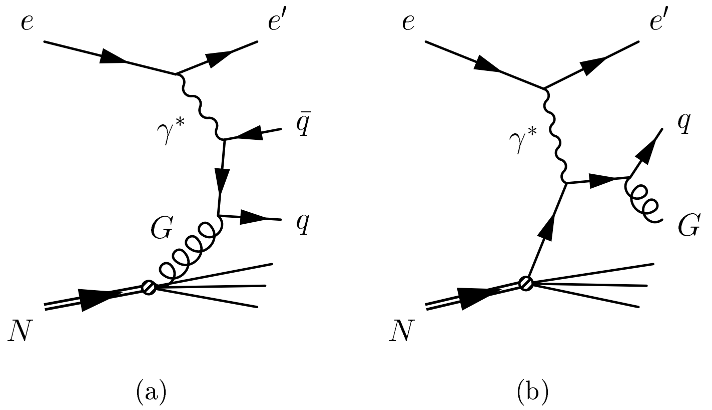

Figure 1-5: The two "direct" processes: (a) photon gluon fusion (PGF) and (b) the QCD Compton effect (QCDC)

The subprocess cross sections $d\sigma/d\hat{t}$ for both photon gluon fusion and the QCD Compton effect are easily calculable to first order in α_s:

$$\frac{d\sigma^{\gamma^* G\to q\bar{q}}}{d\hat{t}} = \frac{\pi e_q^2 \alpha_e \alpha_s}{\hat{s}^2}\left(\frac{\hat{u}}{\hat{t}} + \frac{\hat{t}}{\hat{u}} - \frac{2\hat{s}Q^2}{\hat{t}\hat{u}}\right), \tag{1.33}$$

$$\frac{d\sigma^{\gamma^* q\to Gq}}{d\hat{t}} = \frac{8\pi e_q^2 \alpha_e \alpha_s}{3\hat{s}^2}\left(-\frac{\hat{u}}{\hat{s}} - \frac{\hat{s}}{\hat{u}} + \frac{2\hat{t}Q^2}{\hat{s}\hat{u}}\right). \tag{1.34}$$

Here, the cross section for QCDC is written for $\hat{t}$ being the momentum transfer between the photon and the gluon. The Mandelstam invariants at the subprocess level, $\hat{s}$, $\hat{t}$, and $\hat{u}$, are related to the photon virtuality Q^2 by the relation $\hat{s}+\hat{t}+\hat{u} = -Q^2$. These equations are written for massless quarks and gluons. Note that the matrix elements are collinearly divergent (for $\hat{t} = \hat{u} = 0$), but are safe against $Q^2 \to 0$, the photoproduction limit. Since the virtual photon flux $\Gamma(Q^2, \nu)$ is maximal as $Q^2 \to 0$, it is logical to extend measurements into the photoproduction regime to boost statistics from these processes. Note that the kinematic lower limit on the photon virtuality is $Q^2_{\min} = \frac{m_e^2\nu^2}{E(E-\nu)}$ (set by the scale of the electron mass) while the upper limit is $Q^2_{\rm max} = 2m_{\rm p}\nu$ (set by the elastic scattering limit).

From equation (1.32), it is already obvious that to maximize the contribution of photon gluon fusion to the cross section, one should use h^+h^- pairs. In this way, products of favored fragmentation functions (fragmentation functions where the observed hadron contains the quark which fragmented) will appear in the sum over quark species for the photon gluon fusion piece of the cross section.

The quark and gluon structure functions of equation (1.32) must be evaluated at the scale of the hard subprocess. In the following, the limit $Q^2 \to 0$ is taken, so that the typical choice of setting this scale equal to Q^2 is not possible. In this limit, the scale is chosen so that it is zero in the collinear case, and symmetric under the interchange of $\hat{t}$ and $\hat{u}$. A possible choice is therefore a multiple of $\hat{p}_T^2 = \hat{s}\hat{t}\hat{u}/(\hat{s}+Q^2)^2$, the transverse momentum of the outgoing partons in the center of mass frame. From here on, this scale is chosen to be equal to $\hat{p}_T^2$. This choice is not unique, but is typical for hard photoproduction experiments.

Under the additional assumption of spin-independent fragmentation (as was assumed in the discussion of semi-inclusive deep-inelastic scattering), the polarized cross section may be written as:

$$\begin{aligned}\frac{d^6\Delta\sigma^{eN\to h_1h_2X}}{d\nu dQ^2 dx d\hat{t} dz_1 dz_2} &= \frac{d^6\Delta\sigma^{eN\to h_1h_2X}_{\rm PGF}}{d\nu dQ^2 dx d\hat{t} dz_1 dz_2} + \frac{d^6\Delta\sigma^{eN\to h_1h_2X}_{\rm QCDC}}{d\nu dQ^2 dx d\hat{t} dz_1 dz_2} \\ &= \Delta\Gamma(Q^2,\nu)\left[\sum_q \Delta G(x,\hat{p}_T^2)\frac{d\Delta\sigma^{\gamma^* G\to q\bar{q}}}{d\hat{t}}\left(D_q^{h_1}(z_1)D_{\bar{q}}^{h_2}(z_2) + D_{\bar{q}}^{h_1}(z_1)D_q^{h_2}(z_2)\right)\right. \\ &\left. + \sum_q \Delta q(x,\hat{p}_T^2)\frac{d\Delta\sigma^{\gamma^* q\to Gq}}{d\hat{t}}\left(D_q^{h_1}(z_1)D_G^{h_2}(z_2) + D_G^{h_1}(z_1)D_q^{h_2}(z_2)\right)\right]. \quad (1.35)\end{aligned}$$

In the limit $Q^2 \to 0$, the polarized subprocess cross sections become:

$$\frac{d\Delta\sigma^{\gamma^* G\to q\bar{q}}}{d\hat{t}} = -\frac{\pi e_q^2 \alpha_e \alpha_s}{\hat{s}^2}\left(\frac{\hat{u}}{\hat{t}} + \frac{\hat{t}}{\hat{u}}\right), \quad (1.36)$$

$$\frac{d\Delta\sigma^{\gamma^* q\to Gq}}{d\hat{t}} = \frac{8\pi e_q^2 \alpha_e \alpha_s}{3\hat{s}^2}\left(\frac{\hat{u}}{\hat{s}} - \frac{\hat{s}}{\hat{u}}\right). \tag{1.37}$$

The measured cross section asymmetry $A_{||}$ will be given by the ratio of the integrals of the polarized and unpolarized cross sections (as in equation (1.30). However, if the requirements placed on the observed hadrons select a relatively small region of the six-fold differential phase space, the polarized to unpolarized cross section ratio may be approximated as:

$$\frac{\int d\Delta\sigma}{\int d\sigma} \equiv A_{||}^{eN\to h_1h_2} \simeq \langle D(y)\rangle \left(\langle \hat{a}_{\mathrm{PGF}}\rangle\langle\frac{\Delta G(x)}{G(x)}\rangle f_{\mathrm{PGF}} + \langle \hat{a}_{\mathrm{QCDC}}\rangle\langle\frac{\Delta q(x)}{q(x)}\rangle f_{\mathrm{QCDC}}\right). \tag{1.38}$$

Here, $D(y)$ is the usual virtual photon depolarization factor (see equation (1.16)). The quantities $\hat{a}_{\mathrm{PGF}}$ and $\hat{a}_{\mathrm{QCDC}}$ are subprocess asymmetries, while f_{PGF} and f_{QCDC} are the unpolarized fractions of events originating each of the subprocess types.

The subprocess asymmetries are given simply by the ratio of the polarized subprocess cross section to the polarized subprocess cross section, which, in the photoproduction limit are [9, 10]:

$$\hat{a}_{\mathrm{PGF}} = \frac{d\Delta\sigma^{\gamma^* G\to q\bar{q}}/d\hat{t}}{d\sigma^{\gamma^* G\to q\bar{q}}/d\hat{t}} = -1, \tag{1.39}$$

$$\hat{a}_{\mathrm{QCDC}} = \frac{d\Delta\sigma^{\gamma^* q\to Gq}/d\hat{t}}{d\sigma^{\gamma^* q\to Gq}/d\hat{t}} = \frac{\hat{s}^2 - \hat{u}^2}{\hat{s}^2 + \hat{u}^2}, \tag{1.40}$$

The kinematics selected by high-p_T back-to-back hadrons will be such that the outgoing partons in the will be constrained to scattering angles in the center of mass frame of roughly $\hat{\theta} \simeq \pi/2$, giving $\hat{a}_{\mathrm{QCDC}} \simeq 3/5$.

The subprocess fractions are given by:

$$f_{PGF} = \frac{\int d\sigma_{\mathrm{PGF}}^{eN\to h_1h_2X}}{\int d\sigma^{eN\to h_1h_2X}} \tag{1.41}$$

$$f_{QCDC} = \frac{\int d\sigma^{eN\to h_1 h_2 X}_{\mathrm{QCDC}}}{\int d\sigma^{eN\to h_1 h_2 X}} \tag{1.42}$$

where the integrals are over the kinematics contrained by the measured kinematical quantities. Monte Carlo integration will be used to calculate these factors in this case.

Inverting equation (1.38), and having a knowledge of all the other quantities allows an extraction of the polarization of the gluons in the nucleon from the measured asymmetry $A_{||}$:

$$\frac{\Delta G}{G}(\langle x\rangle) \simeq \langle\frac{\Delta G(x)}{G(x)}\rangle = \frac{A_{||} - \langle D(y)\rangle\langle\hat{a}_{\mathrm{QCDC}}\rangle\langle\frac{\Delta q(x)}{q(x)}\rangle f_{\mathrm{QCDC}}}{\langle D(y)\rangle\langle\hat{a}_{\mathrm{PGF}}\rangle f_{\mathrm{PGF}}} \tag{1.43}$$

evaluated at the average kinematics of the measurement.

1.2.4 Photoproduction of high-p_T hadron pairs

For finite p_T and non-zero Q^2, there will be other processes that can, in principle, contribute to the cross section to produce two hadrons. In leading order, two types of processes can contribute: direct photon processes, where the photon interacts with the nucleon as a bare photon, and hadronic photon processes, where the photon interacts with the proton via hadronic interactions, for example, diffractive processes.

For $Q^2 = 0$ the only direct processes possible are photon gluon fusion and the QCD Compton effect. For non-zero Q^2, virtual photoabsorption (described in the naive quark parton model of deep-inelastic scattering) is also possible, though its contribution is suppressed by the requirement of high p_T. Since the HERMES experiment makes use of an untagged photon beam, originating from the HERA positron beam, the background due to virtual photoabsorption must be estimated. For now, this background will be assumed to be small, since it should in principle be dominated by the comparatively large photoproduction cross sections.

Hadronic photon processes are suppressed for non-zero Q^2, but become important for $Q^2 \to 0$, a limit that will be taken in the analysis of the data. The hadronic photon processes can be separated into contributions from vector-meson dominance (VMD), and from non-resonant $q\bar{q}$, or "anomalous" contributions.

A general description of high-energy photoproduction is found in Ref. [26], and the discussion that follows is closely connected to this reference.

Schematically, and following the notation of Ref. [27], the wave function of the physical photon may be written as:

$$|\gamma\rangle = \sqrt{Z_3}|\gamma_B\rangle + c\sqrt{\alpha_e}|h\rangle. \tag{1.44}$$

This equation expresses the fact that the physical photon is a superposition of the bare photon γ_B and the hadronic photon h. The coefficients must satisfy $Z_3 = 1 - c^2\alpha_e$. Although the hadronic component is of order $\sqrt{\alpha_e}$, this component turns out to be dominant in γN interactions, due to the largeness of the hN cross-section. In the vector-meson dominance model, the state $|h\rangle$ must have the same quantum numbers as the photon: $J^{PC} = 1^{--}$ and $Q = B = S = 0$. In its simplest form, the model includes the three lowest lying vector mesons:

$$c\sqrt{\alpha_e}|h\rangle = \sum_{V=\rho,\omega,\phi} \frac{e}{f_V}|V\rangle. \tag{1.45}$$

This description is successful for photoproduction at low energies. For higher mass states (above the ϕ), one typically adds another continuum term:

$$c\sqrt{\alpha_e}|h\rangle = \sum_{V=\rho,\omega,\phi} \frac{e}{f_V}|V\rangle + \frac{e}{f_{q\bar{q}}}|q\bar{q}\rangle. \tag{1.46}$$

The factors $(e/f_V)^2$ give the probability for the transition $\gamma \to V$, and can be obtained from fits to low energy photoproduction and e^+e^- annihilation data. Normally, these couplings are assumed to be independent of energy. The anomalous coupling depends on the typical scale μ of the interaction:

$$\left(\frac{e}{f_{q\bar{q}}}\right)^2 \simeq \frac{\alpha}{2\pi}\frac{N_C}{3}\left(2\sum_q e_q^2\right)\ln\left(\frac{\mu^2}{p_0^2}\right) \tag{1.47}$$

where $N_C = 3$ and q runs over the quarks that are massless at scale μ. The scale p_0 is typically chosen to be larger than the scale of the highest mass VMD interactions $p_0 > \frac{1}{2}m_\phi$.

Another term $|l^+l^-\rangle$ can, in principle, be added to the photon wavefunction. However, in γp interactions, this term will give rise to a contribution of order α_e^2, since the leptons would not undergo strong interactions to leading order. Radiative corrections of this sort will therefore be neglected. The γp cross section can therefore be decomposed as follows:

$$\sigma^{\gamma\mathrm{p}} = \sigma^{\gamma\mathrm{p}}_{\mathrm{direct}} + \sigma^{\gamma\mathrm{p}}_{\mathrm{VMD}} + \sigma^{\gamma\mathrm{p}}_{\mathrm{anomalous}}. \tag{1.48}$$

The three event classes are pictured schematically in Fig. 1-6.

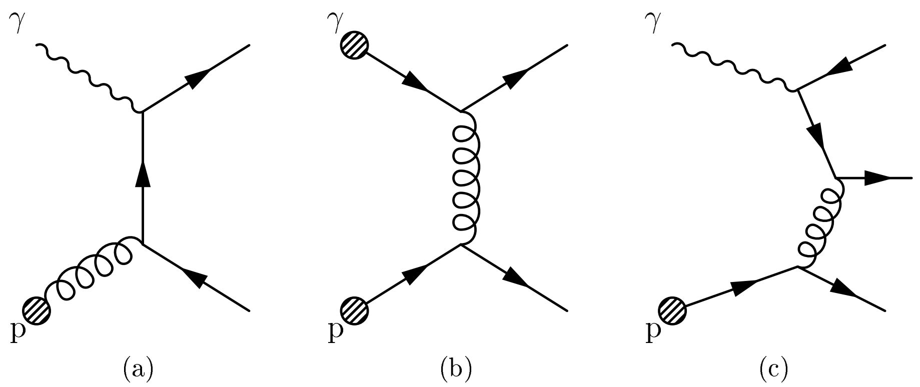

Figure 1-6: The different processes contributing to γp scattering: (a) direct processes, (b) VMD processes, and (c) anomalous processes.

The VMD processes can be further subdivided into elastic, diffractive and non-diffractive components. The VMD elastic process is:

$$\gamma + \mathrm{p} \to V + \mathrm{p}. \tag{1.49}$$

The singly and doubly diffractive processes are of the type where either the proton breaks up, the vector meson breaks up, or both break up:

$$\begin{aligned} \gamma + \mathrm{p} &\to V + X, \\ \gamma + \mathrm{p} &\to X + \mathrm{p}, \\ \gamma + \mathrm{p} &\to X_1 + X_2. \end{aligned} \tag{1.50}$$

The non-diffractive processes are those where no significant rapidity gap between the beam and target fragments can be seen:

$$\gamma + \mathrm{p} \to X. \tag{1.51}$$

The non-diffractive piece of the cross-section can be further subdivided into hard and soft pieces. The term "hard" refers to events where high-p_T jets are produced. To first order, these are phenomenologically treated as events where beam and target partons interact with one another via a first-order QCD Feynman graph. The cross section per jet p_T in this mode is given by (analogous to the direct processes considered earlier):

$$\frac{d\sigma}{dp_T^2} = \sum_{i,j} \int dx_1 \int dx_2 \int d\hat{t} f_i(x_1, \mu^2) f_j(x_2, \mu^2) \frac{d\sigma_{ij}}{d\hat{t}} \delta\left(p_T^2 - \frac{\hat{t}\hat{u}}{\hat{s}}\right) \tag{1.52}$$

where i and j are summed over the possible interacting partons in each hadron. The term "soft" refers to events where no such high-p_T jets are produced. These kinds of events are typically described using minimum-bias phenomenology. The separation between the soft and hard non-diffractive events is given by a cut-off $p_T^{\min}$.

A model of the total γp cross section as a function of energy is shown in Fig. 1-7. This is the model that will be used to determine $\Delta G/G$ from the asymmetry data. The broad features of the model at HERMES energies ($\sqrt{s} \simeq 7$ GeV) are that roughly 80% of the cross section is made up of VMD processes and that 20% is direct processes. Anomalous photon processes are expected to contribute very little to the cross section, becoming significant only at considerably higher $\sqrt{s}$.

1.2.5 Measurements of $G(x)$ using high-p_T hadron production

High-p_T leptoproduction has been used to extract the unpolarized gluon distribution $G(x)$ in both the photoproduction and DIS regimes.

The EMC experiment found that a hadron produced in DIS could acquire transverse momentum in four different ways [28]:

- intrinsic k_T of the struck quark,
- multiple soft gluon radiation from the struck quark,
- hard QCD processes (to first order, PGF and QCDC),
- p_T accumulated in hadronization.

These effects were discovered by considering p_T versus x_F correlations (the so-called "seagull plot") in the current ($x_F > 0$) and target ($x_F < 0$) regions, and comparing with the Lund model. The "hard QCD" processes were found to be required in order for the current hadrons to have sufficient p_T. The level of compensation was found to be in agreement with measurements of the unpolarized quark and gluon distributions from this experiment. All the above effects are included in current models of ep and μp interactions. Energy flows in forward hadron production in DIS were also found to show the emergence of jets with increasing p_T [29, 30]. Energy correlations between jets at fixed target energies have been used to extract the unpolarized gluon distribution [31].

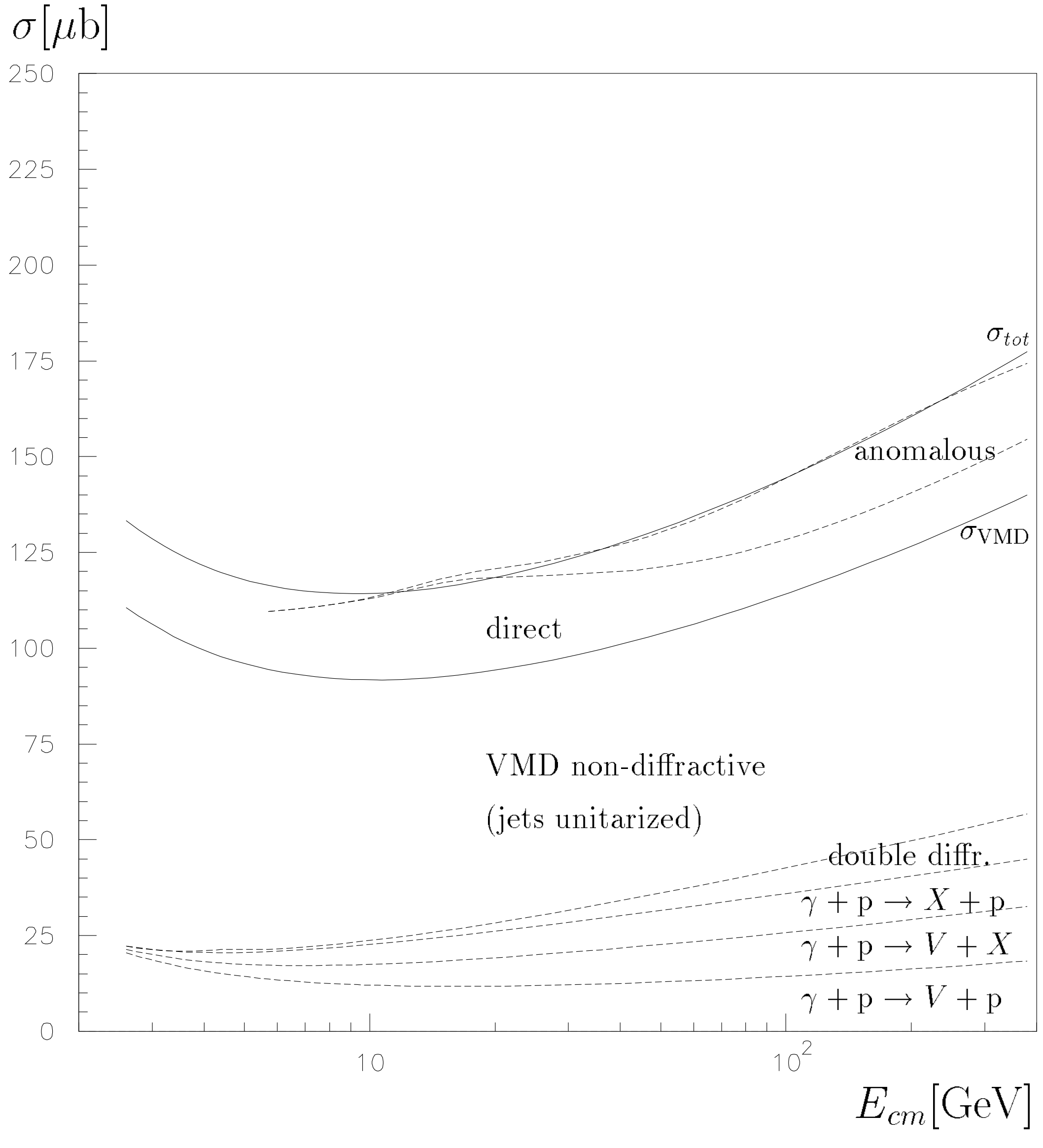

Figure 1-7: Relative contributions of different processes to the total γp cross section

Recent collider experiments have used jet production to extract the unpolarized gluon distribution [32]. The result of such an extraction, compared with other measurements of the same quantity, is shown in Fig. 1-8, and is found to agree well with the other measurements. Included on the plot are measurements of $G(x)$ from QCD fits of $F_2(x, Q^2)$, from charm production, and from global fits. NLO calculations of dijet rates in DIS have become available for comparison [33]. Of note is the steep rise of $xG(x)$ with decreasing x. It will be seen in section 1.3.3 that the polarized analogue $x\Delta G(x)$ is expected to be large only for larger $x \gtrsim 0.1$, meaning that the gluons at low x are unpolarized.

Recently, there has been much interest in high-p_T photoproduction at the HERA collider experiments. Measurements of cross sections as a function of x_γ have shown the separation of the resolved and direct parts of the photon [34, 35, 36]. Here, x_γ (defined in a similar way to x) has the physical interpretation of being the fraction of the photon momentum carried by a partonic constituent of the photon. Using knowledge of the quark and gluon distributions in the proton, the cross section measurement for resolved photons ($x_\gamma < 1$) has allowed the extraction of the gluon distribution in the photon [37]. Meanwhile, the cross section for direct processes ($x_\gamma \equiv 1$) has been shown to be in agreement with expectations from perturbative QCD.

Such hard, resolved-photon processes are not expected to play a role at lower center of mass energies, as was displayed in Fig. 1-7.

1.3 Motivation to Study the Gluon Polarization

The angular momentum sum rule was introduced in section 1.1.3. It has been mentioned that the naive expectation of $\Delta\Sigma = 1$ is apparently violated. A brief review of how this was discovered will be presented. Some of the possible resolutions of this problem will be discussed. One such solution is a significant anomalous contribution to $\Delta\Sigma$. This would result in a significant gluon polarization ΔG. The current sta-

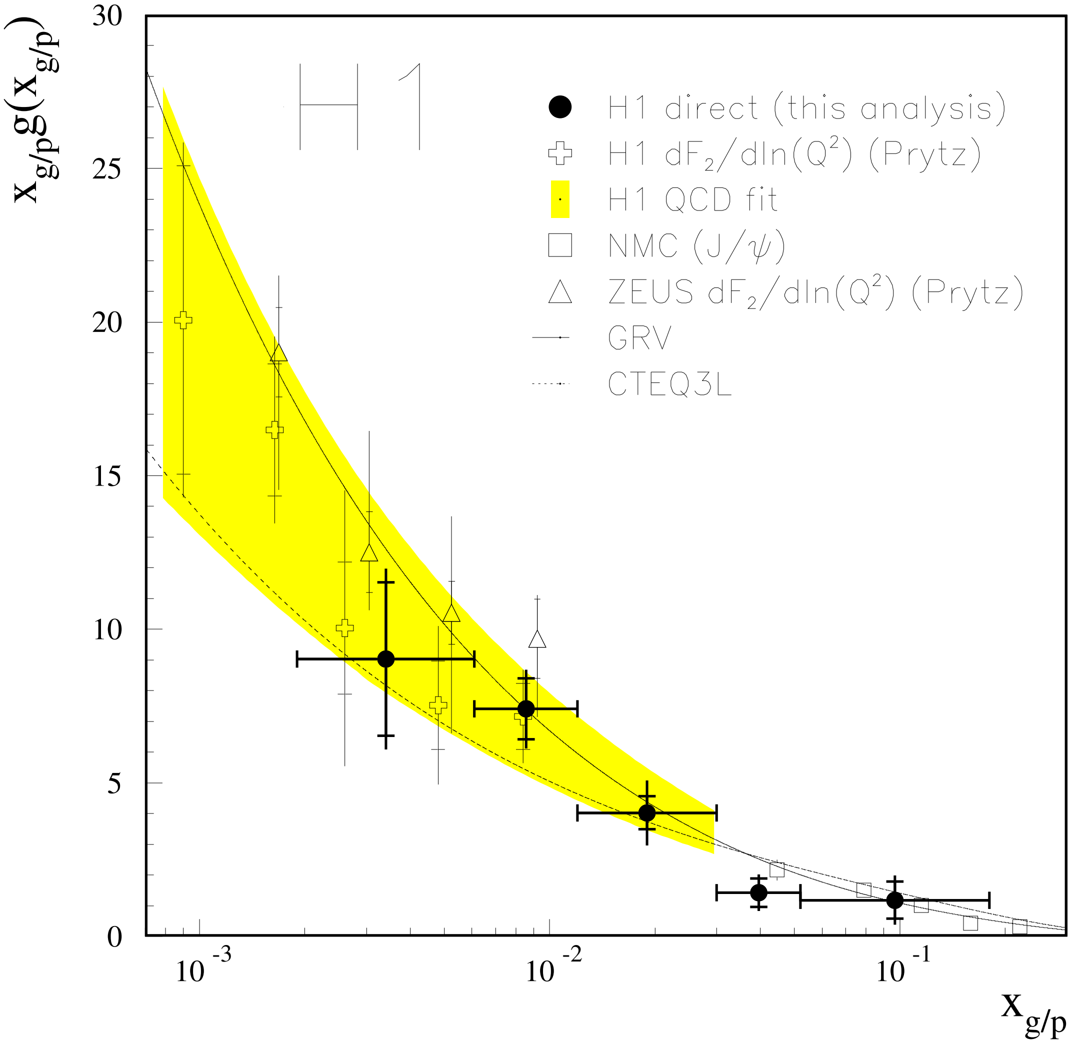

Figure 1-8: Fig. 5 of Ref. [32]. $xG(x)$ at $Q^2 = 30$ (GeV/c)^2 extracted using different methods. The solid points show the results of the dijet analysis.

tus of phenomenological fits of $\Delta G(x, Q^2)$ (discussed briefly in section 1.2.1) will be reviewed.

1.3.1 The Origin of the Nucleon Spin in the Quark Parton Model

Theoretical discussions of the nucleon spin are presented in Refs. [38, 39]. The discussion is somewhat simplified, here, beginning with the definition of the axial vector quark currents of the nucleon, the relationship of these currents to hyperon decays and deep-inelastic scattering, and the apparent contradiction that arises in the angular momentum sum rule of the nucleon.

The axial vector quark currents are defined as:

$$J^j_{5\mu} = \bar{\psi}\gamma_\mu\gamma_5 \left(\frac{\lambda_j}{2}\right)\psi \qquad (j = 1, ..., 8) \tag{1.53}$$

where ψ is written in the flavor basis:

$$\psi = (\psi_u, \psi_d, \psi_s) \tag{1.54}$$

and the λ_j are the Gell-Mann matrices. The singlet axial vector current may be defined as:

$$J^0_{5\mu} = \bar{\psi}\gamma_\mu\gamma_5\psi. \tag{1.55}$$

For a proton with four-momentum P^μ and four-spin $S^\mu(\lambda)$ corresponding to helicity λ, the matrix elements a_j and a_0 are defined as:

$$\langle P, S|J^j_{5\mu}|P, S\rangle = M a_j S_\mu, \tag{1.56}$$

$$\langle P,S|J^0_{5\mu}|P,S\rangle = 2Ma_0S_\mu. \tag{1.57}$$

Assuming that the eight spin-1/2 hyperons form an octet under $SU(3)_F$, and that the vector and axial vector currents transform as an octet, and that these currents are conserved, then all hyperon β decays may be described in terms of two constants F and D, arising in the matrix elements of the axial currents:

$$\langle B_i;P,S|J^j_{5\mu}|B_k;P,S\rangle = 2M_BS_\mu\{-if_{ijk}F + d_{ijk}D\}, \tag{1.58}$$

where the indices i, j, and k run from 1 to 8 and f_{ijk} and d_{ijk} are $SU(3)_F$ group constants.

The values of F and D are arbitrary in this model, and may be determined from hyperon decay data:

$$F = 0.477 \pm 0.012, \quad D = 0.756 \pm 0.011. \tag{1.59}$$

The independent constants F and D can be expressed in terms of the octet matrix elements a_3 and a_8, as:

$$a_3 = F + D, \quad a_8 = 3F - D. \tag{1.60}$$

Note that weak hyperon decays have no sensitivity to $J^0_{5\mu}$ or to a_0.

To relate these constants to deep-inelastic scattering requires the operator product expansion. If one assumes the naive quark parton model, the relationships simplify immensely. In the framework of this model, the matrix elements of the axial vector currents are directly related to the polarized quark distributions measured in deep-inelastic scattering:

$$\langle P,S|J^f_{5\mu}|P,S\rangle = 2MS_\mu\int_0^1 dx[\Delta q_f(x) + \Delta\bar{q}_f(x)], \tag{1.61}$$

which is written in the quark flavor basis. In terms of the matrix elements a_j, the following equations apply:

$$a_3 = \Delta u + \Delta\bar{u} - \Delta d - \Delta\bar{d}, \tag{1.62}$$

$$a_8 = \Delta u + \Delta\bar{u} + \Delta d + \Delta\bar{d} - 2\Delta s - 2\Delta\bar{s}, \tag{1.63}$$

and

$$a_0 = \Delta u + \Delta\bar{u} + \Delta d + \Delta\bar{d} + \Delta s + \Delta\bar{s} \equiv \Delta\Sigma \tag{1.64}$$

thereby defining $\Delta\Sigma$, the contribution of the quark spins to the nucleon spin. Note that the notation $\Delta q_f = \int_0^1 dx \Delta q_f(x)$ has been implicitly defined. It is worth mentioning that QCD corrections to equations (1.62), (1.63), and (1.64) acquire a Q^2 dependence to higher orders in QCD which disappears only for infinite Q^2. This results in the left hand side being multiplied by QCD corrections $C(Q^2)$ and each term of the right hand side acquiring a Q^2 dependence $q_f \to q_f(Q^2) = \int_0^1 dx \Delta q_f(x, Q^2)$. The Q^2 dependence will be suppressed for much of the following discussion.

The integral Γ_1^p can therefore also be related to a_3, a_8, and a_0 as follows:

$$\Gamma_1^p \equiv \int_0^1 dx g_1^p(x) = \frac{1}{12}\left\{a_3 + \frac{1}{3}a_8 + \frac{4}{3}a_0\right\}, \tag{1.65}$$

and can therefore be used to extract $a_0 = \Delta\Sigma$.

Ellis and Jaffe used equation (1.65) to make an estimate of the size of Γ_1^p, by assuming that the strange quark polarizations are small $\Delta s \simeq \Delta\bar{s} \simeq 0$ [40]. In this way a_0 is related to a_8: $a_0 \simeq a_8$. This gives the Ellis-Jaffe sum rule prediction for Γ_1^p:

$$(\Gamma_1^p)_{EJ} = \frac{1}{12}\left\{a_3 + \frac{5}{3}a_8\right\} \simeq 0.188 \pm 0.004. \tag{1.66}$$

Under these assumptions, the singlet matrix element has a value $\Delta\Sigma = a_8 \simeq 0.6$.

This is apparently at odds with the expectation from the naive quark parton model. In this model, all the quarks move parallel to the parent hadron, and therefore carry no angular momentum. Effects from gluons are ignored. Therefore, the spins of the quarks must add up to the total spin of the proton, implying that $\Delta\Sigma = 1$ [38]. However, QCD-inspired bag models of the nucleon are able to account for the reduction by including intrinsic k_T and therefore angular momentum, giving $\Delta\Sigma \simeq 0.65 - 0.75$ [41]. A similar result, $\Delta\Sigma = 0.75$ was calculated in a relativistic three-quark model of the nucleon using light-cone quantization [42].

An extraction of a_0 is possible by measuring $g_1(x, Q^2)$ and extrapolating outside the measured x-range to get the total integral $\Gamma_1^p(Q^2)$. A recent HERMES result [43, 44], which makes use of additional information from semi-inclusive hadron production from both proton neutron targets, puts a_0 extracted from deep-inelastic scattering at the level $a_0 = 0.30 \pm 0.04 \pm 0.09$ at $Q^2 = 2.5$ (GeV/c)^2. This value is in good agreement with other deep-inelastic scattering experiments. However, it is in contrast to the value $a_0 \simeq 0.6$ expected based on relativistic quarks models and hyperon decay measurements, assuming Δs to be zero. That a_0 is so small was first discovered by the EMC experiment [45].

The result for a_0 can be easily incorporated into $SU(3)_F$ by allowing the strange quarks to carry a significant polarization. A recent analysis [46] gives the world-averaged result $\Delta s + \Delta\bar{s} = -0.10 \pm 0.03$ at $Q^2 = 2.5$ (GeV/c)^2. Recent HERMES measurements of the same quantity, however, do not assume $SU(3)_F$ because of the extra degrees of freedom afforded by semi-inclusive measurements. Instead, an assumption about the symmetry of the sea quarks is made, i.e. that their polarization $\Delta\bar{q}(x)/\bar{q}(x)$ is the same, independent of flavour. Under this assumption, the HERMES extraction gives $-0.01 \pm 0.03 \pm 0.04$ [43], which appears somewhat smaller than the $SU(3)_F$ models which rely on inclusive data. Such semi-inclusive measurments promise to scrutinize $SU(3)_F$ in the future.

Other extractions (e.g. Ref. [47]) suggest that the hyperon β-decay results apply only to the so-called valence quark distributions $\Delta u_V = \Delta u - \Delta \bar{u}$ where sea quark effects are subtracted. This is often referred to as the "valence" scenario, where the usual interpretation is referred to as the "standard" scenario [48]. Averaging the sea polarizations, thereby defining $\Delta \bar{q} = \Delta u = \Delta \bar{u} = \Delta d = \Delta \bar{d} = \Delta s = \Delta \bar{s}$, gives a somewhat smaller sea-averaged polarization $\Delta \bar{q} = -0.05$ (at similar scale $Q^2 = 4$ (GeV/c)^2).

The puzzle arises when one considers why the extracted $a_0 = \Delta\Sigma$ makes up such a small piece of the total nucleon spin. The angular momentum sum rule (equation (1.19)), then implies that the gluon spin and quark and gluon orbital angular momentum contributions must be large.

1.3.2 The Anomalous Contribution to $\Delta\Sigma$ and the Gluon Spin

Another solution to the smallness of $\Delta\Sigma$ comes from the axial anomaly [38, 49]. This contribution arises due to the fact that the axial current for quark flavor f

$$J^f_{5\mu} = \bar{\psi}_f(x)\gamma_\mu\gamma_5\psi_f(x) \tag{1.67}$$

is not conserved, as expected from the Dirac equation, but has an anomalous contribution due to the triangle diagram shown in Fig. 1-9:

$$\partial^\mu J^f_{5\mu} = \frac{\alpha_s}{2\pi}\mathrm{Tr}[G_{\mu\nu}\tilde{G}^{\mu\nu}] \tag{1.68}$$

for massless quarks and non-zero gluon virtuality. If the quarks are more massive than the gluon virtuality, the anomalous contribution is found to vanish. Generally, one takes m_u, m_d, and m_s to be $<< k^2$, the gluon virtuality, and m_c, m_b, and $m_t >> k^2$.

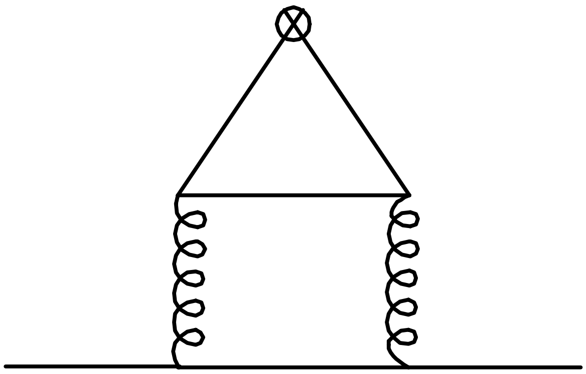

Figure 1-9: Triangle diagram contributing to non-conservation of the axial currents (from Ref. [39]).

The matrix element $a_0 = \langle P,S|J^0_{5\mu}|P,S\rangle$ then picks up an extra contribution:

$$a_0^{\text{gluons}}(Q^2) = -3\frac{\alpha_s}{2\pi}\int_0^1 dx \Delta G(x,Q^2) = -3\frac{\alpha_s}{2\pi}\Delta G(Q^2), \tag{1.69}$$

so that

$$a_0 = \Delta\Sigma - 3\frac{\alpha_s}{2\pi}\Delta G. \tag{1.70}$$

The anomaly has been shown to be stable to higher orders in perturbation theory, and it has been argued that equation (1.68) is true even beyond perturbative QCD [38].

The correction due to the anomaly allows for another way to account for a_0 being so small, via ΔG. Setting $\Delta s + \Delta\bar{s}$ to zero, and leaving $\Delta\Sigma$ at the level 0.6 gives a value for $\Delta G(Q^2)$ of about 1.9 at scale $Q^2 = 4.0$ (GeV/c)^2 [47].

The problem with this explanation for the deficit of quark spin as measured by DIS is that, to higher orders, it depends on the regularization scheme [39]. For example, in the modified minimal subtraction ($\overline{\text{MS}}$) scheme, the contribution due to the anomaly disappears and a relationship similar to the naive QPM result holds, namely $a_0 = \Delta\Sigma$.

However, it has been argued that the schemes including the anomalous contribution are more physical for the specific case of deep-inelastic scattering [4, 50]. There are several reasons for this, which include:

- Practically massless "current" quarks preserve chirality.
- The anomalous term in a_0 is Q^2 independent in leading order.
- In QCD-improved parton models, the anomalous term can be physically interpreted as the contribution of the photon-gluon fusion graph to the first moment $\Gamma_1^p(Q^2)$.

It has therefore been argued that soft contributions are not properly factored out of the coefficient functions in schemes such as $\overline{\mathrm{MS}}$. Many phenomenological fits therefore use schemes which include the anomalous contribution, such as the Adler-Bardeen (AB) scheme (defined in Ref. [4]).

Revisiting the angular momentum sum rule (equation (1.19)), there is a contribution $\Delta\Sigma \simeq 0.6$ and, taking the anomaly at face value, a contribution $\Delta G \simeq 1.9$ (at $Q^2 = 4$ (GeV/c)^2) which rises with increasing Q^2. To compensate for the large value of ΔG, there must a significant contribution of the opposite sign from the orbital angular momentum of the quarks and gluons. This can be easily understood in terms of evolution of parton angular momentum in QCD [38]. A quark which radiates a gluon preserves its helicity, via high-energy helicity conservation. If ΔG is non-zero, the gluon is radiated with some preferred helicity. The orbital angular momentum of the quark-gluon final state must compensate for the component of the spin carried by the radiated gluon. Therefore, as ΔG increases, L_z must also increase with opposite sign, in agreement with the expectation from the angular momentum sum rule.

1.3.3 Results of Phenomenological Fits to Inclusive Polarized DIS: The Current Status of ΔG

Since this thesis will use a leading-order QCD model, the results of LO phenomenological fits are of primary interest. However, NLO corrections are important for more more accurate determinations of ΔG, and the results of such fits will also be discussed.

Two sets of recent LO fits are available in Refs. [47, 48]. Both references also provide NLO fits.

Ref. [47] makes use of the anomalous contribution to a_0 to set the normalization of ΔG via violation of the Ellis-Jaffe sum rule. At their starting scale, $Q^2 = 4$ (GeV/c)^2, they find $\Delta G = 1.9$. This reference also uses the "valence" scenario, including a small, negative sea quark polarization.

In contrast, Ref. [48] omits the anomaly, and varies the relation of the hyperon beta matrix elements to the first moments of the polarized quark distributions between the "standard" and "valence" scenarios (described at the end of section 1.3.1).

The effects on $\Delta G(x, Q^2)$ are shown in Fig. 1-10 at scale $Q^2 = 2$ (GeV/c)^2. From the fits of Ref. [48], it is seen that even if the anomaly is not included in the fits, the result for the best fit of $\Delta G(x, Q^2)$ still tends to be positive.

Several groups have recently presented next-to-leading-order analyses of the polarized structure functions [47, 48, 6, 4, 50]. These references vary in their treatment of the anomaly and the standard vs. valence treatment of the relationship of the hyperon decay constants to the non-singlet sector of polarized deep-inelastic scattering.

Ref. [48] is the only one to consider the valence vs. standard scenarios, and, as in leading order, the effect was found to be small. This reference also uses the $\overline{\mathrm{MS}}$ scheme in order to be consistent with its leading-order analysis and unpolarized fits of the time. Ref. [47] also uses $\overline{\mathrm{MS}}$, also for consistency with unpolarized fits of the time.

Refs. [4, 50] define and use the AB scheme, citing the afore-mentioned features of this scheme when used in the context of deep-inelastic scattering.

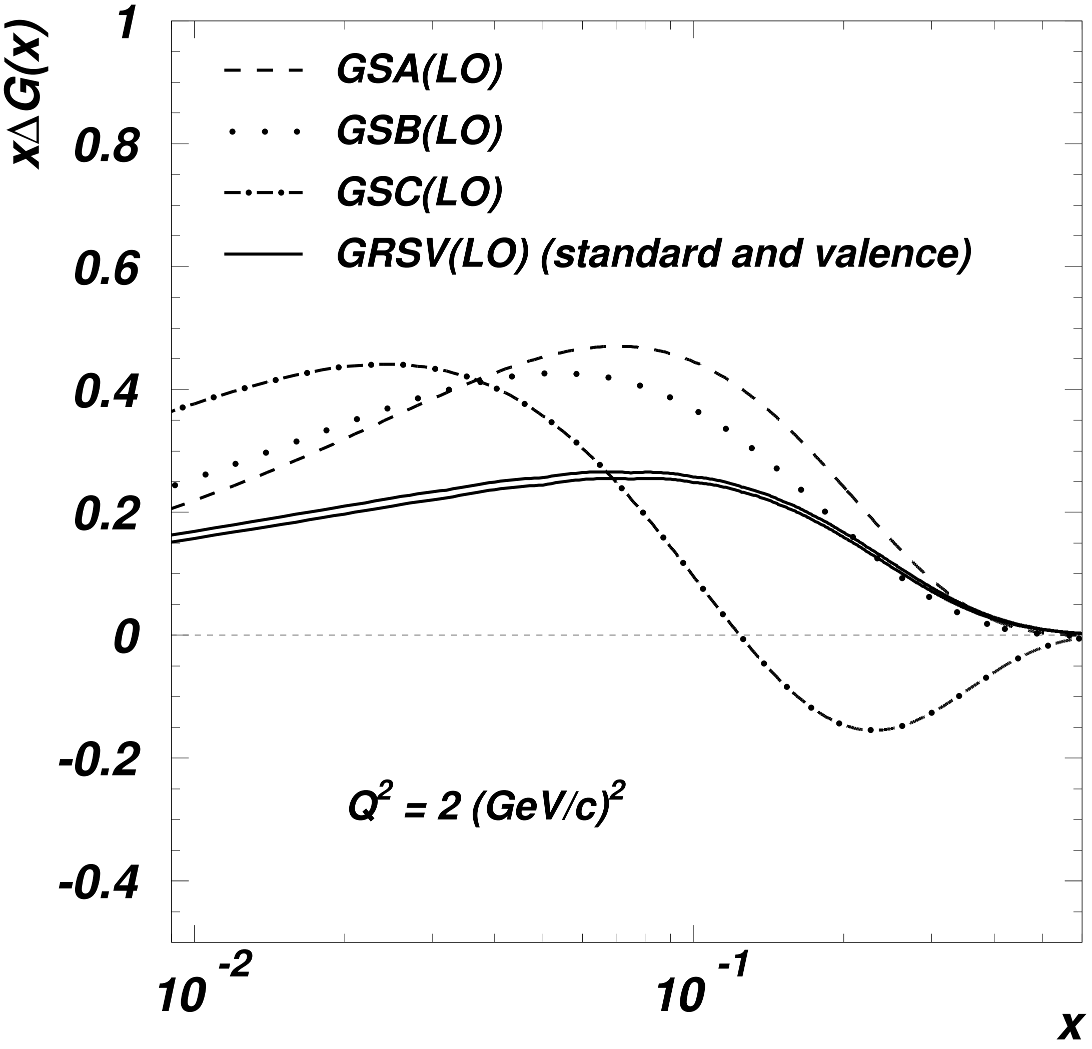

Figure 1-10: Recent leading-order polarized gluon distribution functions from Ref. [47] (GSA, B, and C) and Ref [48] (GRSV standard and valence fits) for $Q^2 = 2$ (GeV/c)^2. For the GRSV curves, the upper curve is the valence scenario and the lower curve is the standard scenario.

Of the above sets of fits, Ref. [6] is the only reference which adequately addresses the difference between the renormalization schemes, and the statistical errors of the measurements. The differences in the $\overline{\mathrm{MS}}$ and AB renormalization schemes from this analysis are shown in Fig. 1-11. From this figure, it can be seen that the main differences between the $\overline{\mathrm{MS}}$ and AB schemes arise in the singlet sector ($\Delta\Sigma$ and ΔG). In the $\overline{\mathrm{MS}}$ scheme, the $\Delta\Sigma$ is negative at low x due to negatively polarized sea quarks, whereas in the AB scheme, this contribution is shuffled into a positive polarized gluon distribution. However, the fit for the polarized gluon distribution tends to be positive in both cases.

For consistency with previous analyses, the authors of this reference then chose to work in the AB scheme. In Fig. 1-12, the AB fits of Ref. [6] are displayed with error bars. From this figure, it can be seen that the statistical and theoretical uncertainties are large for the measurement of ΔG. The theoretical uncertainties are dominated by uncertainties in the factorization and renormalization scales (which were varied within the range $0.5Q^2 <$ scale $< 2.0Q^2$) and uncertainty in the assumed functional form of the initial parton distributions. However, note that, for this plot, no uncertainty was assigned due to variation of the renormalization scheme.

The current indirect experimental information on the polarized gluon structure function suggests positive values of $\Delta G(x)$. However, the size of the polarized gluon distribution is currently tied to the issue of the role of the anomaly in the axial vector quark current. Even a negative or zero ΔG is not entirely excluded. Direct measurements of $\Delta G(x, Q^2)$ are necessary and will play an important part in the resolution of the question of the origin of the nucleon spin.

1.4 Future Experiments

Several experiments [1, 2, 3] have been proposed to study the polarized gluon distribution $\Delta G(x)$. The experiments also plan to study other spin effects in the nucleon;

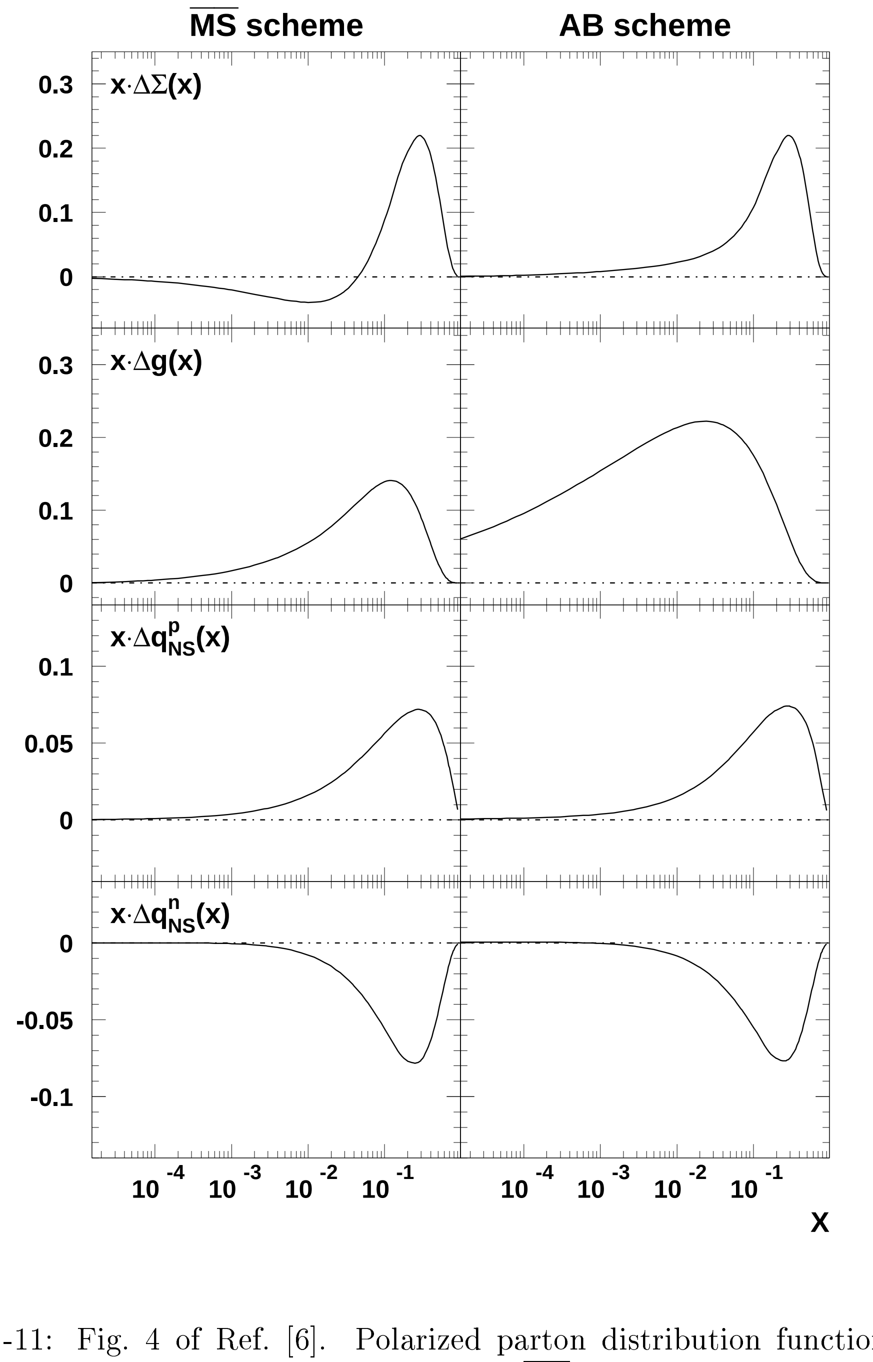

Figure 1-11: Fig. 4 of Ref. [6]. Polarized parton distribution functions at $Q^2 = 5\ (\mathrm{GeV/c})^2$ obtained in two different schemes, $\overline{\mathrm{MS}}$ and AB.

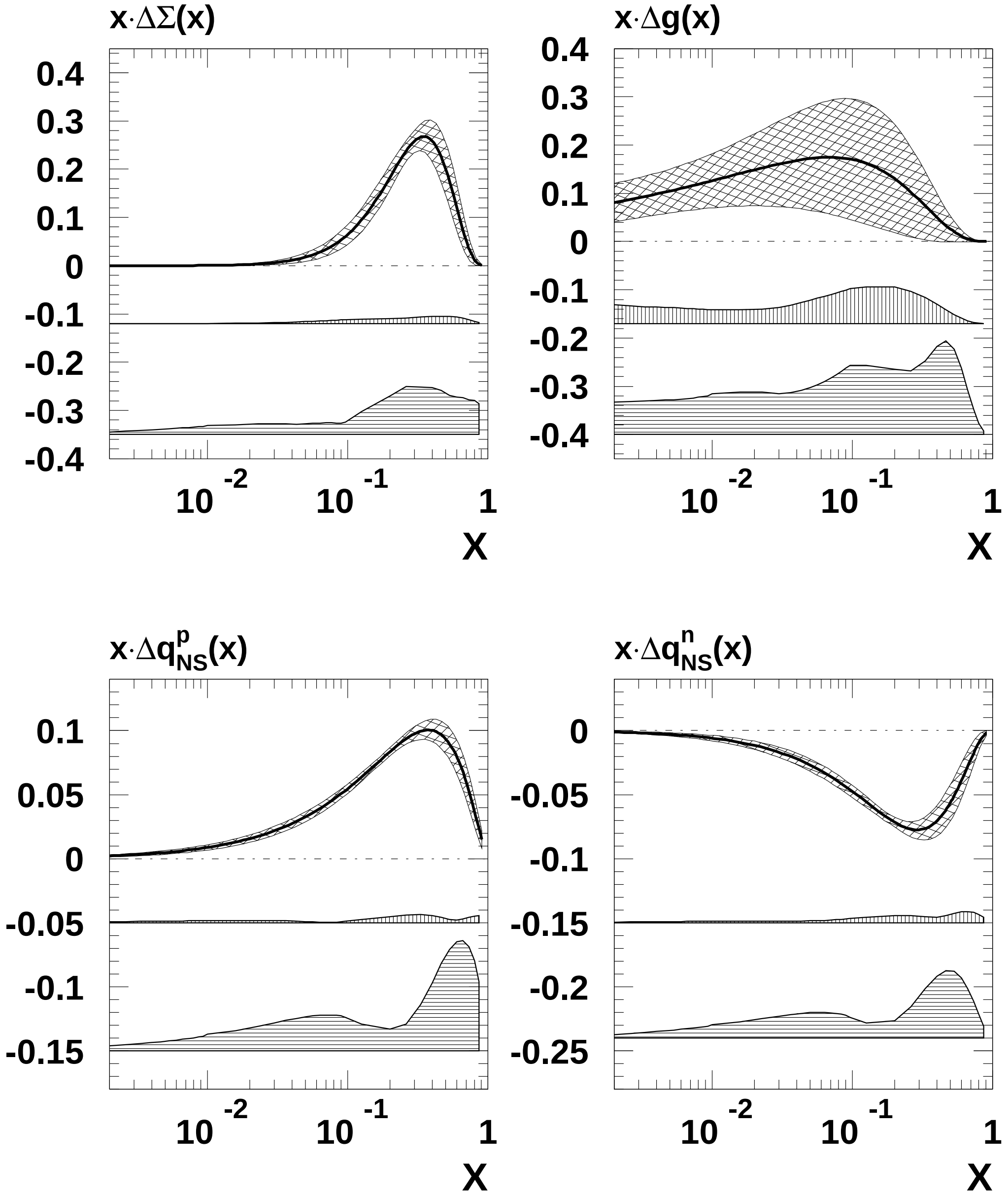

Figure 1-12: Fig. 5 of Ref. [6]. Polarized parton distributions at scale $Q^2 = 5\ (\mathrm{GeV/c})^2$ in the AB scheme. The cross-hatched band is the statistical uncertainty. The vertically hatched band is the experimental systematic uncertainty. The horizontally hatched band is the theoretical uncertainty.

however, only the aspects related to the determination of $\Delta G(x)$ will be described, here.

1.4.1 The HERMES Charm Upgrade

A proposed upgrade to the HERMES spectrometer [1] has been partially completed and aims to improves the charm detection capabilities of the spectrometer. The changes include introducing a muon wall, enlarging the angular acceptance of the spectrometer to broaden the acceptance for J/ψ and D meson decays, and the upgrade of the threshold Čerenkov counter to a Ring-Imaging Čerenkov counter (for complete π/K/p separation over the full momentum range). For 80 pb^{-1} integrated luminosity (corresponding roughly to running through 1999 for 8.5 months with a polarized deuterium ABS target, or 4.5 million DIS events), the expected precision from D meson production in a variety of channels is $\delta(\Delta G/G)_{\text{stat.}} = 0.45$, limited mainly by the inability to detect D mesons cleanly due to large combinatorial backgrounds, and the small cross section for charm production near threshold.

Though the detection efficiency for J/ψ production is also improved, the relationship of its spin asymmetry to $\Delta G/G$ is not clear (as described in section 1.2.2).

Another aspect of the upgrade is improved small angle acceptance using small chambers embedded in the quadrupole magnets in the beamline downstream of the HERMES experiment. The Forward Quadrupole Spectrometer (FQS) will allow for the detection of positrons scattered at small angles and therefore better determination of photoproduction kinematics. This upgrade, despite its small angular acceptance, will therefore in the future have an impact on the high-p_T photoproduction analysis which is the subject of this thesis.

1.4.2 COMPASS

The COMPASS experiment also aims to study $\Delta G/G$ using charm production [2] and high-p_T hadron production [8].

The experiment plans to use incident muons of energy 100 GeV and polarization 80%, and to take data for one and a half years with a ^{6}LiD target with 50% polarization and one year with a NH_3 target with 85% polarization. Eighty percent of the time will be spent running with longitudinally polarized targets (the remaining 20% with transversely polarized targets).

Using several detection schemes for D mesons, the experiment plans to measure $\Delta G/G$ with a statistical precision $\delta(\Delta G/G)_{\text{stat.}} \simeq 0.11$. Other decay channels are under investigation. For 100 GeV muons, the x_G range probed is $0.07 < x_G < 0.4$ [51].

Including data from high-p_T hadron pair production is hoped to improve the statistical accuracy attained for $\Delta G/G$. Using the following selection criteria [8]:

- two hadrons with $p_T > 1.0 - 1.5$ GeV/c and mass of an assumed two pion system $M(2\pi) > 2.5 - 3.0$ GeV/c^2,
- $x_F > 0$ to ensure the hadrons are current fragments,
- $\Delta\phi \simeq 180°$ to ensure they are produced back to back,
- oppositely charged hadrons, to increase fraction of events from photon gluon fusion,

was found to give good sensitivity of the longitudinal spin asymmetry to $\Delta G/G$. Using K^+K^- pairs was also found to improve the sensitivity to $\Delta G/G$; however, such a cut also reduced statistics. The expected precision with which $\Delta G/G$ will be measured is $\delta(\Delta G/G)_{\text{stat.}} \simeq 0.05$ for each year of running. The x_G range that is probed is roughly $0.05 < x_G < 0.3$.

The COMPASS experiment also plans to add data to the determination of $g_1(x, Q^2)$ at higher Q^2. This will allow for a more precise determination of $\Delta G(x, Q^2)$ from scaling violations. The x range over which $g_1(x, Q^2)$ will be measured is roughly 0.003 to 0.7, the same as the SMC experiment [52]. Improved large angle muon acceptance for the COMPASS experiment is hoped to also improve DIS rates at large x.

1.4.3 RHIC Spin

Using the inverse of the QCD Compton effect:

$$q + G \rightarrow q + \gamma \tag{1.71}$$

allows measurements of prompt photon or photon+jet production in pp or p$\bar{\text{p}}$ collisions to gain sensitivity to gluon structure functions of the proton. In the polarized case, the double spin asymmetry in prompt photon production is expected to be directly related to the product of the quark and gluon polarizations:

$$A_{LL}(x) = [\Delta u(x)/u(x)][\Delta G(x)/G(x)]\hat{a}_{LL}(x). \tag{1.72}$$

The RHIC Spin program [3] plans to exploit this fact to measure $\Delta G/G$ using both the STAR and PHENIX detectors. The experiments plan to collide polarized protons at two center of mass energies: 200 and 500 GeV. The integrated luminosities expected to be attained at each beam energy in the polarized running are 320 and 800 pb^{-1} at $\sqrt{s} = 200$ and 500 GeV, respectively. The proton beam polarization is expected to be roughly 70%.

A recent prediction [53] for the PHENIX collaboration is shown in Fig. 1-13. The precision with which $\Delta G/G$ is determined is roughly 0.05 to 0.30 in each x bin for each beam energy setting.

A drawback of the PHENIX detector is its small kinematic coverage for photons. The STAR detector has a larger kinematical coverage for photons, and consequently is expected to attain higher precision for $\Delta G/G$. The expected precision for $\Delta G/G$ is 0.04 at $\sqrt{s} = 200$ GeV, covering an x range of 0.05-0.3, and 0.03 at $\sqrt{s} = 500$ GeV, covering an x range of 0.02-0.3 [54].

Though direct γ production is likely the cleanest way to measure $\Delta G/G$ using a polarized pp collider, other jet-jet channels can be opened up using quark-gluon scat-

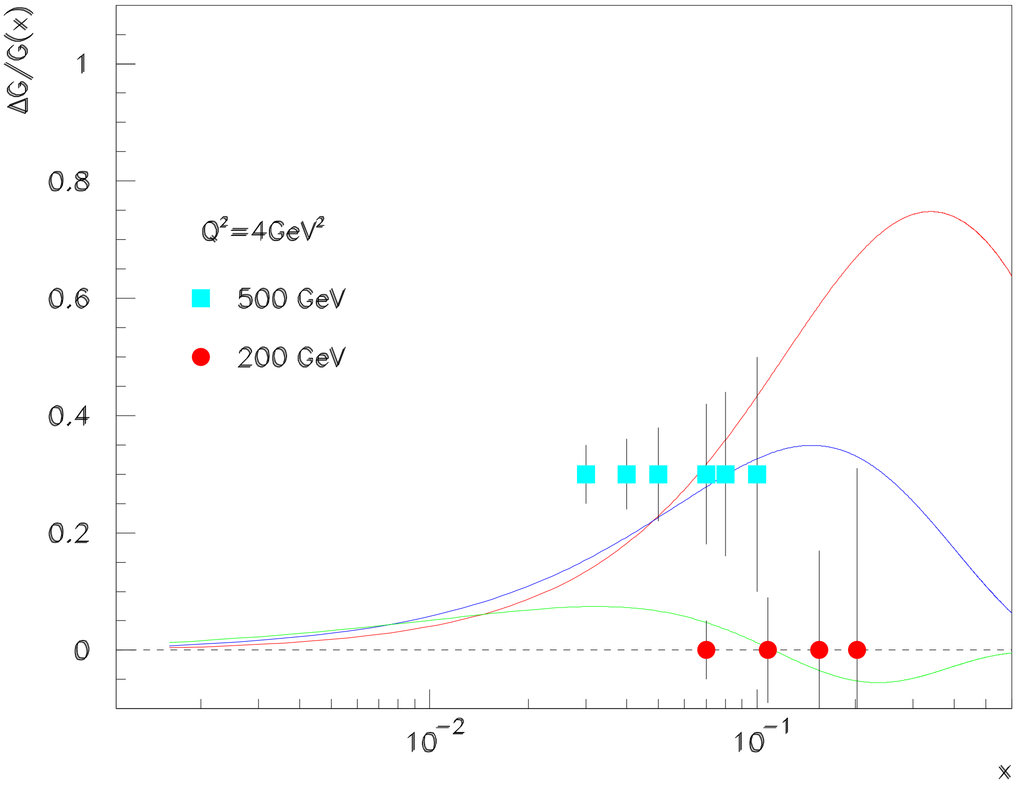

Figure 1-13: Fig. 1 of Ref. [53]. Expected precision for gluon polarization measurement using direct-γ production at PHENIX. Curves are from Ref. [47]

tering and gluon-gluon scattering. Gluon-gluon scattering in particular is expected to dominate in lower-p_T regions, and may dominate for production of single particles [3].

1.4.4 Polarized HERA

Using the same technology as the RHIC collider, HERA could be converted to a polarized ep collider. Using both jet production and scaling violations of g_1, such a collider would yield an accurate determination of $\Delta G(x, Q^2)$ [55, 56]. Colliding the polarized proton beam with a polarized fixed target, such as that used at the HERMES experiment, would yield physics opportunities similar to those at RHIC, with similar projected error bars for the determination of $\Delta G/G$ [57]. The range of x probed would be essentially the same as that for the current HERA experiments, i.e. roughly the range $1 \times 10^{-3} < x < 0.1$. This would nicely complement the fixed target and RHIC collider kinematic domains.

The required upgrade to the existing HERA ring is costly and time-consuming, and whether or not this option will be pursued is uncertain.

Chapter 2

Experiment

The data in this thesis were collected in 1996 and 1997 at the HERMES experiment at the HERA storage ring of the DESY laboratory. In this chapter, the experiment will be described. The key features of the experiment are catalogued in this introduction.

At the HERMES experiment, longitudinally polarized positrons of energy 27.6 GeV are scattered from polarized internal gas targets. The beam polarization was continuously measured by Compton back-scattering and reached typical values of 55% with a systematic fractional uncertainty in the measurement of 3.4%. The HERMES polarized proton target is formed by injecting a nuclear-polarized beam of atomic hydrogen into a tubular open-ended storage cell. The target polarization was 0.79 ± 0.06 in 1996 and 0.88 ± 0.04 in 1997, where the quoted errors are systematic.

The HERMES detector is a forward spectrometer with a dipole magnet providing an integrated field of 1.3 Tm. The magnet is divided into two identical sections by a horizontal iron plate that shields the positron and proton beams from the magnetic field. Consequently, the spectrometer consists of two identical detector systems, upper and lower, with a minimum polar angle for the acceptance of particles produced from the target region of 40 mrad. The maximum angular acceptances are ± 140 mrad vertically and ± 170 mrad horizontally. For charged particles with momenta from 4.5 to 27 GeV/c, the average momentum resolution $\Delta p/p$ is about 1%.

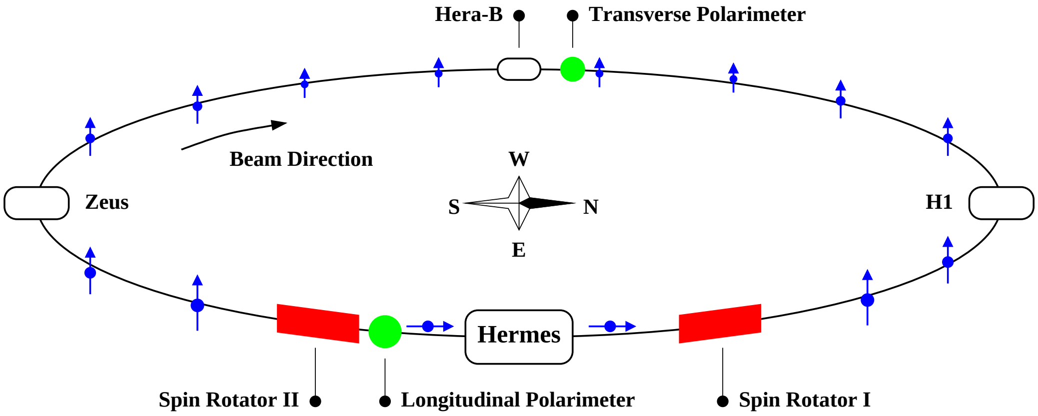

Figure 2-1: Schematic layout of the HERA accelerator. The positions of the four experiments making use of the ring (H1, HERMES, Zeus, and HERA-B) are shown, along with the positions of the two beam polarimeters and the spin rotators on either side of the HERMES experimental site.

Particle identification (PID) is accomplished using a lead-glass electromagnetic calorimeter, a scintillator hodoscope preceded by two radiation lengths of lead, a six-module transition radiation detector, and a C_4F_{10}/N_2(70:30) gas threshold Čerenkov counter. The Čerenkov counter may also be used to identify pions with momenta between 4.5 and 13.5 GeV/c.

Each component of the experiment will now be described in greater detail.

2.1 The Polarized Positron Beam

The Hadron-Electron Ring Accelerator facility (HERA) is located at the Deutsches Elektronen-Synchrotron (DESY), in Hamburg, Germany. It collides electrons and protons at high energies. The electron and proton storage rings share the same tunnel, which is 6.335 km in circumference. A schematic layout of the HERA electron ring is presented in Fig. 2-1. Two other experiments (ZEUS and H1) take data using the collider mode of the accelerator to study ep interactions at high energies. The HERA-B experiment is in the commissioning stage and will collide the HERA proton beam with wire targets to search for CP violation in the B meson system. The HERMES experiment uses only the HERA electron ring, colliding it with a fixed internal gaseous target. The electrons circulating in the ring are arranged in 210 bunches, 96 ns apart. Each bunch contains 3.8×10^{10} electrons. The bunch length is 27 ps. The current in the ring reached typically 30 mA.

In 1996 and 1997, HERA was operated using positrons as opposed to electrons. Positrons were used because the stored beam lifetime was substantially longer. The positrons repel positively charged ions created in collisions with residual gas in the imperfect vacuum of the ring, keeping them away from the beam axis. The ring uses a series of RF cavities to bring the positrons to energies of 27.6 GeV from the injected energy of 14 GeV. Polarization in the ring is built up over time via the Sokolov-Ternov effect [58, 59]. Sokolov and Ternov discovered that the synchrotron radiation of a circulating lepton beam will have an asymmetry. The asymmetric emission of synchrotron radiation gives rise to transverse polarization of the electrons in the ring. For electrons (positrons) the polarization is antiparallel (parallel) to the magnetic field used to bend the leptons in the synchrotron. The polarization increases with time according to the relation:

$$P(t) = P_{\mathrm{max}}(1 - e^{-t/\tau}) \tag{2.1}$$

where τ is the time to accumulate polarization and P_{max} is the asymptotic limit. For an ideal flat machine the maximum asymptotic limit is $P^{\mathrm{ST}}_{\mathrm{max}} = 0.92$. Depolarizing effects in a real machine result in a lower limit. At HERA a typical polarization maximum is $P^{\mathrm{HERA}}_{\mathrm{max}} = 0.55$. For an ideal HERA machine running at 27.6 GeV, the time constant $\tau^{\mathrm{ST}} = 37$ min. Adding depolarizing effects with a typical depolarizing time τ^{D} will decrease this time according to:

$$\frac{1}{\tau} = \frac{1}{\tau^{\mathrm{ST}}} + \frac{1}{\tau^{\mathrm{D}}} \tag{2.2}$$

and will also decrease the maximum attainable polarization:

$$P_{\max} = P_{\max}^{\mathrm{ST}} \frac{\tau}{\tau^{\mathrm{ST}}}. \tag{2.3}$$

The transverse polarization is converted into linear polarization at the HERMES experimental site using spin rotators. Spin rotator I rotates the spin of the incident positrons into a longitudinal state before they reach the HERMES experiment. Spin rotator II rotates this longitudinal polarization back to the transverse direction of the rest of the ring after the positrons have passed through the HERMES experiment. For a non-flat machine (i.e. a machine with spin rotators), the above equation for $P_{\max}$ is modified with a multiplicative factor $(1+\delta)$ due to depolarizing effects from the spin rotators. The rise with time of the polarization of positrons in the HERA ring with spin rotators is shown in Fig. 2-2.

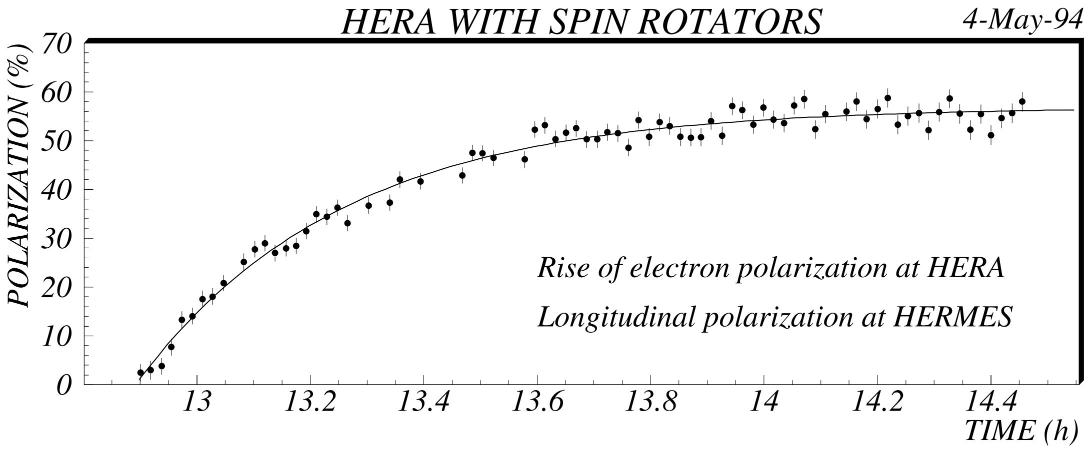

Figure 2-2: The rise of polarization in the HERA ring with spin rotators.

Two beam polarimeters continuously measure the polarization in the ring [59]. Both use high power lasers to backscatter circularly polarized Compton photons from the electrons in the ring. The transverse polarimeter measures the vertical polarization of the electrons in the ring and the longitudinal polarimeter measures the longitudinal polarization of the electrons in the ring near the HERMES interaction point.

The cross-section for the scattering of the polarized photons is dependent on the polarization of the electrons. Since only vertical (P_y) and longitudinal (P_z) components of the electron polarization $\mathbf{P}$ are measured, integrating over the horizontal component leads to:

$$\frac{d\sigma_c}{d\Omega}(\mathbf{S},\mathbf{P}) = \frac{1}{2}r_0^2\left(\frac{k_f}{k_i}\right)^2[\Sigma_0 + S_1\Sigma_1 + S_3(P_y\Sigma_{2y}) + P_z\Sigma_{2z}] \tag{2.4}$$

where S_1 and S_3 are the linear and circular components of the initial photon polarization $\mathbf{S}$, r_0 is the classical electron radius, and k_i and k_f are the initial and final photon momenta in the electron rest frame. $\Sigma_{0,1,2y,2z}$ are unpolarized, single and double polarized cross sections. Σ_{2y} is used for the transverse measurement and Σ_{2z} for the longitudinal measurement.

The two polarimeters will now be described.

2.1.1 The Transverse Polarimeter

The HERA transverse polarimeter and the associated systematic error for its measurement of the beam polarization are described in detail in Ref. [44]. The transverse polarimeter is located across the HERA ring from the HERMES experiment in the West Hall. A schematic layout of the transverse polarimeter is displayed in Fig. 2-3. This polarimeter was commissioned in 1991.

An argon-ion laser provides a continuous 10 W beam of circularly polarized 2.41 eV photons which collides with the HERA electron beam. Lenses and mirrors transport the laser beam roughly 200 m to the interaction point with the electron beam. A Pockels cell is used to switch the photon polarization with a frequency of 90 Hz. The energy and the vertical position of the backscattered Compton photons are measured in a tungsten-scintillator calorimeter located 65 m from the interaction point. The

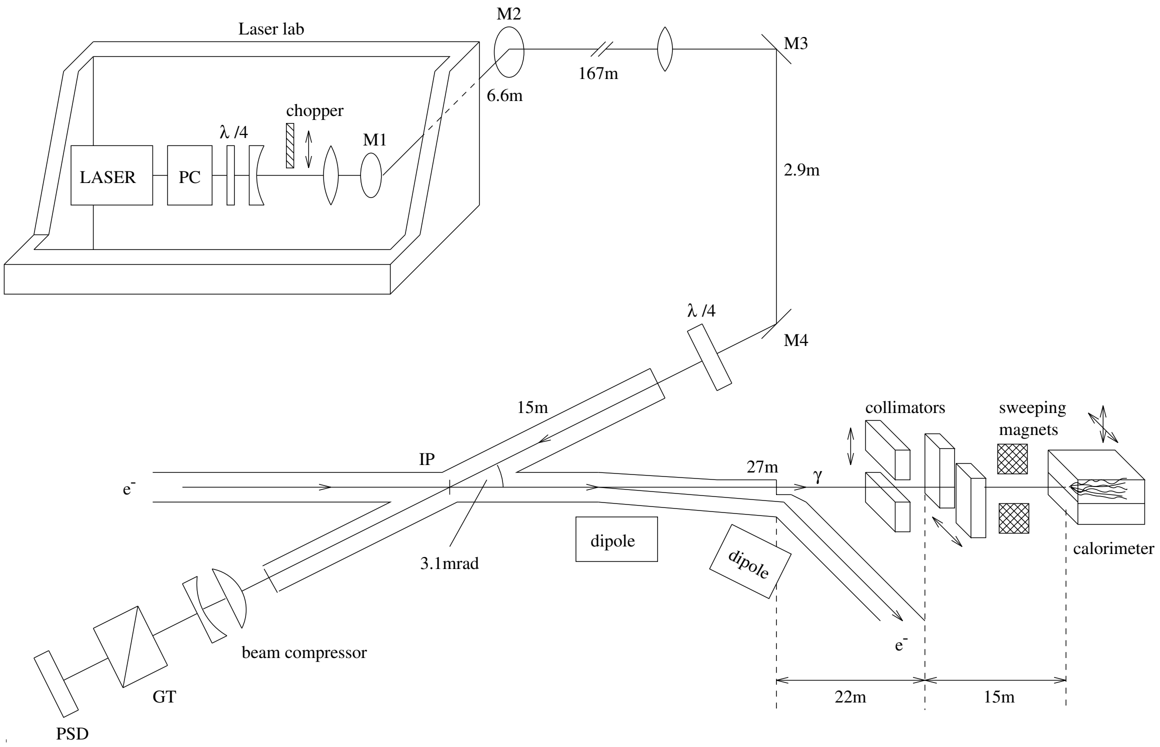

Figure 2-3: The HERA Transverse Polarimeter

calorimeter is split into essentially identical upper and lower halves to give position sensitivity in the vertical direction.

The laser intensity is chosen so that the probability for multiple Compton photons per bunch crossing is about 1%. In this way, the energy and position of each detected photon is used for the analysis. This is commonly known as the "single photon method". By measuring the asymmetry of the energies of the photons detected in the upper and lower calorimeter $\eta(\langle y \rangle) = (E_{\text{upper}} - E_{\text{lower}})/(E_{\text{upper}} + E_{\text{lower}})$, one can determine the mean vertical position $\langle y \rangle$.

The standard method of determining the polarization P_y is from the shift of the mean vertical positions $\langle y \rangle$ measured with left and right circularly polarized light:

$$\Delta\langle y \rangle(E_\gamma) = \frac{1}{2}(\langle y \rangle_L - \langle y \rangle_R) = P_y \Delta S_3 \Pi(E_\gamma) \qquad (2.5)$$

where the analyzing power $\Pi(E_\gamma) \simeq 170\ \mu$m is determined using the η to $\langle y \rangle$ transformation with the polarized cross section Σ_{2y}. The analyzing power is a function of the photon energy, measured using $E_\gamma = E_{\text{upper}} + E_{\text{lower}}$. The statistical precision in the transverse polarization δP_y is roughly 0.01 to 0.02 per minute.

2.1.2 The Longitudinal Polarimeter

In 1996 a second Compton polarimeter (the Longitudinal Polarimeter) was commissioned. The longitudinal polarimeter is located in the HERA tunnel roughly 50 m downstream of the HERMES experiment, before spin rotator II rotates the polarization back into its transverse state in the ring. Unlike the transverse polarimeter, the longitudinal polarimeter uses the energy distibution asymmetry of Compton photons to determine the longitudinal beam polarization $A(E_\gamma) = \Delta S_3 P_z \Sigma_{2z}$. It also uses a "multi-photon method", measuring the total energy deposited in the detector by roughly 1000 Compton photons per bunch crossing. This method is used to overcome large backgrounds from Bremsstrahlung photons which would swamp the single photon method used by the transverse polarimeter.

The layout of the longitudinal polarimeter optical path is shown in Fig. 2-4. A frequency doubled, pulsed YAG laser produces 2.3 eV photons at typically 100 Hz with pulse energies from 1-250 mJ. The laser beam is guided with remotely controlled mirrors and lenses through a 72 m long vacuum pipe to the interaction point with the electron beam. A Pockels cell switches the photon polarization with a frequency of 89 Hz. The backscattered photons are detected in a calorimeter located 54 m downstream of the interaction point. It consists of four NaBi(WO_4) Cerenkov crystals, arranged in a 2×2 array. The energy of the photons is the sum of the energy detected in the four segments. The segmentation allows a determination of the x-y position of the photons. The calorimeter table is periodically recentered using this information, if the scattered Compton photons drift too far towards the edge of the calorimeter. The recentering is necessary typically a few times per fill, due to shifts in the HERA beam

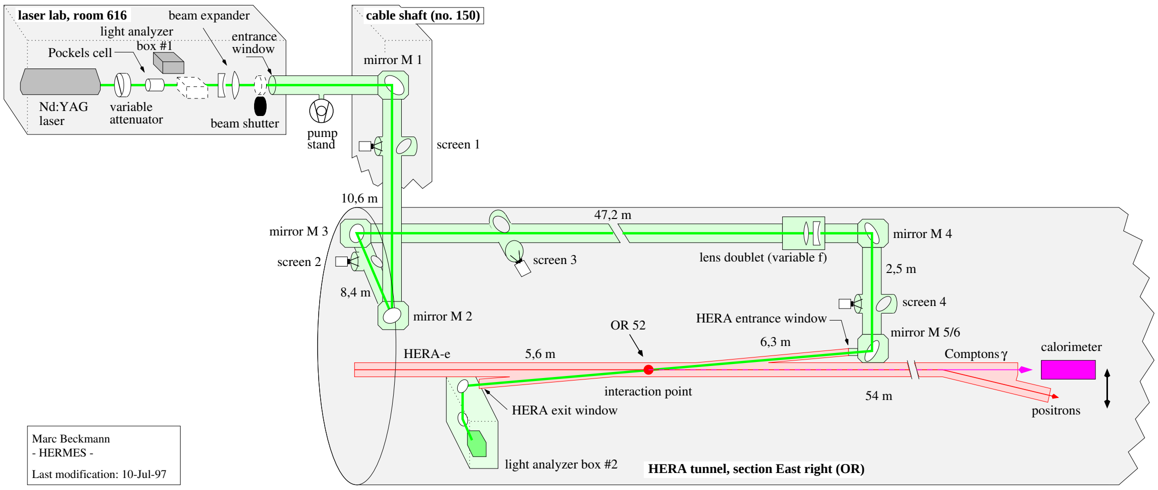

Figure 2-4: The longitudinal polarimeter

position.

The longitudinal polarimeter can achieve a statistical error δP_z of 0.01 in about 40 s. The laser power is typically adjusted to keep the luminosity seen in the calorimeter constant. The bremsstrahlung background can be measured between laser pulses, but is found to be small in multi-photon mode.

2.2 The Internal Gas Target

A variety of polarized and unpolarized internal gaseous target options are available to the experiment.

The HERMES polarized target is formed by injecting a nuclear-polarized beam of ^{1}H, ^{2}H or ^{3}He into a tubular open-ended storage cell. Two different target technologies have provided polarized nuclei for study. In 1995, a source of polarized ^{3}He was used. The ^{3}He target becomes polarized through metastability-exchange optical pumping [60]. Typical polarizations were near 50% with an areal density of 1.0×10^{15} nucleons/cm^2. In 1996 and 1997, a polarized ^{1}H source was used. An atomic beam source uses permanent sextupole magnets and radio-frequency transitions to select the desired hyperfine states [61]. The target polarization was typically 80%, with an areal density of 7×10^{13} nucleons/cm^2. From 1998 to 2000, a polarized atomic deuterium source will be used, also based on atomic beam source technology. The polarized targets are used mainly to study polarized semi-inclusive deep-inelastic scattering and polarized photoproduction.

In addition to polarized targets, HERMES can also use unpolarized targets. These targets are supplied using the HERMES Unpolarized Gas Feed System. The unpolarized gaseous targets used to date are H_2, D_2, ^{3}He, and N_2. Although unnecessary for the photoproduction spin asymmetries that are the subject of this thesis, these targets have been used to extract many fascinating physics results, including:

- unpolarized structure function ratios such as $F_2^{\rm n}(x)/F_2^{\rm p}(x)$, $d_v(x)/u_v(x)$, $F_2^{^3{\rm He}}(x)/F_2^{\rm D_2}(x)$, and $F_2^{\rm N_2}(x)/F_2^{\rm D_2}(x)$ [62],
- nuclear transparency of diffractive incoherent ρ^0 meson production [63],
- nuclear attenuation of charged pion production,
- ρ and ϕ angular decay distributions [64],
- spin transfer of the polarized electron beam to polarized Λ baryons in the final state [65].

The gas feed system was the responsibility of the MIT group and will be discussed in addition to the polarized ^{1}H target, though only the polarized ^{1}H target provided the data presented in this thesis.

The apparatus common to both targets systems will first be discussed. A schematic of the target region is shown in Fig. 2-5. A flow of target gas is directed into a windowless tube that confines the gas atoms in a region close to the positron beam. This storage cell is an elliptical tube mounted coaxially with the HERA positron beam. It confines the target gas near the high energy positron beam, increasing the target thickness by roughly two orders of magnitude compared to an atomic beam. The cell

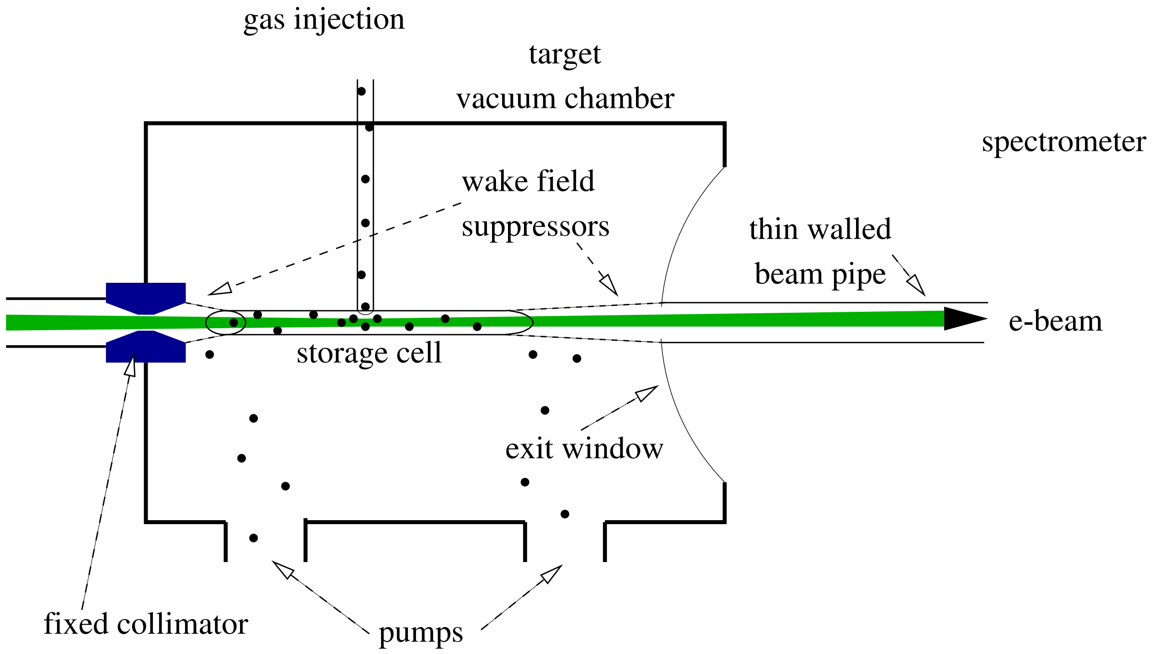

Figure 2-5: Schematic diagram of the target region.

is a 29×9.8 mm^2 elliptical tube that is 400 mm long. It is made from 75 μm thick aluminum. To increase the target thickness even further, the storage cell is cooled by flowing cold helium gas through the support structure. Platinum resistance thermometers mounted on the cell support structure monitor the cell temperature. The typical operating temperature is 100 K.

The ends of the cell are windowless so that the positron beam can pass freely though the cell. To prevent contamination of the positron beam vacuum, a powerful differential pumping system with a total pumping speed of about 9000 L/s is used in the region surrounding the cell to remove the target gas. The pressure in the target region when the ABS is in operation is typically $1.5{\times}10^{-7}$ mbar and this is reduced to about $5{\times}10^{-9}$ mbar outside the target region.

The transition from the cell to the beam pipe was made smooth to avoid the generation of wake fields that could cause heating and increase the emittance of the beam. This was accomplished using thin perforated tubes called "wake-field suppressors".

To protect from synchrotron radiation created upstream of the HERMES area, a system of two collimators, C1 and C2, were installed upstream of the target. C2 is shown in the schematic diagram in Fig. 2-5. C1 is located 2 m upstream of the target and protects C2 from direct radiation. C1 consists of two moveable collimators in the horizontal and vertical directions, separated by a half a meter. These collimators are opened during injection and are returned to a narrower setting before applying high voltage to the elements of the spectrometer. C2 has a fixed aperture and is located directly in front of the storage cell. It also protects the cell from direct radiation during injection.

Particles that scatter from the target gas and into the spectrometer exit the target chamber through a 0.3 mm stainless steel foil. The beam pipe downstream of the target chamber is also made of thin stainless steel. These thin foils present a small probability for radiation to the particles as they enter the spectrometer, thus minimizing electromagnetic showering.

2.2.1 The HERMES Polarized ^{1}H Target

The polarized atomic hydrogen target is described in detail in Refs. [66, 67]. This section is based largely on Ref. [67]. A schematic diagram of the target is shown in Fig. 2-6. A beam of polarized hydrogen atoms is formed using the atomic beam source (ABS). The injected target gas is analyzed using a target gas analyzer (TGA) and a Breit-Rabi Polarimeter (BRP). The TGA measures the fraction of the hydrogen that is in atomic form and the BRP measures the polarization of the atomic hydrogen. Significant Monte Carlo and background corrections are possible to the atomic fraction measured by the TGA, as it is hard to distinguish where the recombination occurred and thus find the true atomic fraction in the target cell.

Each part of the ^{1}H target system will now be described in greater detail, pro-

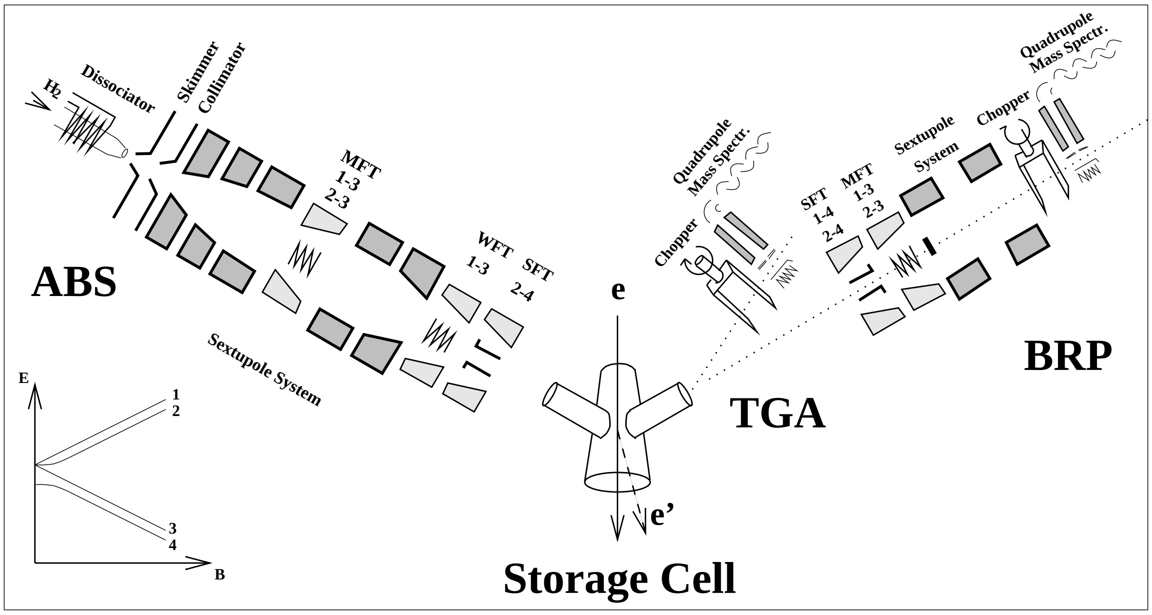

Figure 2-6: Schematic diagram of the HERMES polarized ^{1}H target. Inset: energy level diagram for atomic hydrogen.

ceeding from left to right in Fig. 2-6.

The beam originates in the RF dissociator of the ABS, where injected molecular hydrogen from a gas bottle is converted to atomic form. The RF dissociator simply provides a strong RF field which completely dissociates the hydrogen molecules. The atoms have their electrons polarized by Stern-Gerlach separation in a system of five sextupole magnets. The electron polarization of the atomic beam after the magnet system is transferred to the protons by means of two adiabatic RF transitions. The weak field transition (WFT 1-3) after the magnet system provides negative proton polarization. The strong field transition (SFT 2-4) provides a positive proton polarization. By switching off the transitions, the electron polarized state created by the sextupoles is injected. Using the medium field transition (MFT 1-3/2-3), located after the third sextupole, either hyperfine state $|1\rangle$ or $|2\rangle$ can be transferred into state $|3\rangle$ which can then be deflected away by the remaining two sextupoles. Using this transition in combination with the WFT 1-3 and SFT 2-4 transitions allows the injection of each of the four possible states separately. The seven different combinations possible are catalogued in Table 2.2.1. A small diagram showing the energy level splitting of the four atomic hydrogen states may be found in the inset of Fig. 2-6. To minimize

ABS transitions on	injected states	S_z^e	S_z^p
none	$\lvert 1\rangle$ or $\lvert 2\rangle$	+1	0
WFT 1-3	$\lvert 2\rangle$ or $\lvert 3\rangle$	0	−1
SFT 2-4	$\lvert 1\rangle$ or $\lvert 4\rangle$	0	+1
MFT 2-3, SFT 2-4	$\lvert 1\rangle$	+1	+1
MFT 1-3, WFT 1-3	$\lvert 2\rangle$	+1	−1
MFT 2-3, WFT 1-4	$\lvert 3\rangle$	−1	−1
MFT 1-3, SFT 2-4	$\lvert 4\rangle$	−1	+1

Table 2.1: Injection modes of the ABS [68].

false asymmetries from systematic drifts in the detector, the target polarization is reversed frequently (every 30 seconds).

The polarized atomic hydrogen is injected into the cell through a 100 mm long, 10 mm diameter entry tube and then diffuses out of the ends of the storage cell. The cell is located in a vacuum chamber surrounded by a super conducting magnet which provides a quantization axis for the proton and electron spins. The field is produced by four coils resulting a non-uniformity of $\frac{\Delta B}{B} = \pm 1.5\%$ along the cell axis at the working point of $B = 355$ mT. To economize on cold helium usage, the superconducting target magnet uses the same helium supply as the target cell. The target gas is sampled in the middle of the cell through a 100 mm long 5mm diameter sample tube. A 10 mm diameter 120 mm long extension tube is connected to the sample tube to direct gas into the TGA and BRP.

The TGA measures the relative fluxes of atomic and molecular hydrogen coming through the sample tube. The TGA is mounted off axis by 7° so that is doesn't interfere with the gas entering the BRP. Two baffles collimate the beam entering the TGA. A quadrupole mass spectrometer is used to analyze the resulting beam. A chopper allows the subtraction of background due to residual gas.

The BRP uses a similar RF and sextupole magnet system as the ABS to analyze the atomic polarization of the atoms from the sample tube. The BRP also has elements similar to the TGA to collimate and analyze the beam using a chopper and a quadrupole mass spectrometer. Switching between the four possible states of the two RF transitions and measuring the ^{1}H rate using the mass spectrometer gives a determination of the occupation probabilities for the four hyperfine states. From the occupation probabilities and a knowledge of the guide field, the polarization of the atomic hydrogen can be calculated. To calibrate the BRP, the transition efficiencies of the RF transitions and transmission probabilities of the sextupole system must be measured. The extraction of these factors can be done by switching the ABS and BRP transitions through all possible combinations.

The target polarization is determined using the formula [68]:

$$P_T = \alpha_0[\alpha_r + (1 - \alpha_r)\beta]P_T^{\mathrm{atom}} \tag{2.6}$$

where α_0 is the initial atomic fraction, α_r is the fraction of atoms surviving recombination and β is the polarization of the recombined molecules relative to the polarization of the atomic hydrogen P_T^{atom}. The quantity β is essentially unknown and the lack of knowledge is assigned to a portion of the systematic error on the target polarization. To determine the true α_r and P_T^{atom} in the target cell from the measurements of these quantities from in the TGA and BRP, α_r^{TGA} and $P_{\mathrm{T}}^{\mathrm{BRP}}$, respectively, sampling corrections c_α and c_P must be introduced:

$$\alpha_r = c_\alpha \alpha_r^{\mathrm{TGA}}, \tag{2.7}$$

$$P_T^{\mathrm{atom}} = c_P P_T^{\mathrm{BRP}}. \tag{2.8}$$

The sampling corrections account for effects which might change the measured values due to the fact that the atoms must travel some distance before reaching the TGA and BRP. Possible resulting effects on the measurement of α_r by the TGA are recombination within the gas and on the cell and sample tube walls. Possible effects on the measurement of the atomic polarization are spin exchange in collisions within the gas and spin changes in wall collisions. A Monte Carlo was developed to estimate these corrections and was used to assign a systematic error.

Using these corrections, the injected proton polarization was determined to be typically 95.5%. The average polarization loss was determined to within 2.5% from spin exchange collisions and 1% from wall collisions. The final result was $P_T^{\mathrm{atom}} = 0.92 \pm 0.03$ (syst.). The value for c_α is easier to constrain when α_r^{TGA} is close to unity, as was the case in 1997, resulting in $\alpha_r = 0.93 \pm 0.04$. The range for β was taken to be $0.2 \leq \beta \leq 1.0$, constrained by HERMES estimates when operating the target at low α_r [66, 69]. The result for the target polarization was 0.88 ± 0.04 (syst.) in 1997. For the 1996 data taking, the value for α_r^{TGA} was not as close to 1, resulting in larger Monte Carlo uncertainties. The value for the target polarization in 1996 was roughly 0.85 ± 0.12 (syst.). The error in the 1996 target polarization can be reduced by renormalizing the result to the 1997 results using the deep-inelastic asymmetry. The effect of the systematic uncertainties on the measurement for the asymmetry will be described in chapter 3.

2.2.2 The Unpolarized Gas Feed System

The Unpolarized Gas Feed System (UGFS) is used to supply a variety of pure unpolarized gasesous targets for the HERMES experiment. Several unpolarized measurements carried out by the experiment were described briefly in section 2.2. The UGFS is also used for the calibration of the polarized target. This includes determinations of the unpolarized flows needed to fully determine α_0 for the calculation of the target polarization, such as background pressure in the target chamber due to finite pumping capacity of the HERMES pumpstands in the target region. The UGFS is also used to check the relative calibrations of the ion gauges in the pumpstands in the target region, upon which many of the BRP and TGA calibration parameters depend.

A schematic of the UGFS is shown in Fig. 2-7. The various valves are used to control the direction of flow of the gas, while the pressure gauges and transducers monitor the pressure of the particular gas as it is flowing through the system. The turbo and fore pumps are used to clear gas out of the system quickly, e.g. when changing gas types.

In normal operation, valves 5 and 9 and the bottle valve for the desired gas are left open so that gas flows from the bottle through the thermovalve and diaphragm into the target cell. Valve 6 is used to flow into the target chamber, simulating the background conditions when the polarized ^{1}H target is in operation. This provides a calibration of part of α_0 for the polarized ^{1}H target [66].

The important feature of the system is the ability of the diaphragm and thermovalve to regulate the pressures in the system in order to supply a constant density of the order 10^{15} nucleons/cm^2 to the target cell. Calibrating the diaphragm conductance as a function of the pressures measured by B2 and B4 then allows for an absolute determination of the flow rate. The flow rate has a known dependence on the type of gas that is flowing, so the calibration was performed for only one gas. Calculating the conductance of the target cell then allows for a determination of the target density. The target density calculated using this method has been calibrated to within 20% [70] due largely to a poor calibration of the diaphragm conductance and the need for the use of a calculation to determine the cell conductance.

2.3 Spectrometer

The HERMES spectrometer is described in detail in Ref. [71]. Several of the spectrometer subsystems are described in their own references [72, 73, 74]. A schematic diagram of the spectrometer is shown in Fig. 2-8. The tracking chambers used in

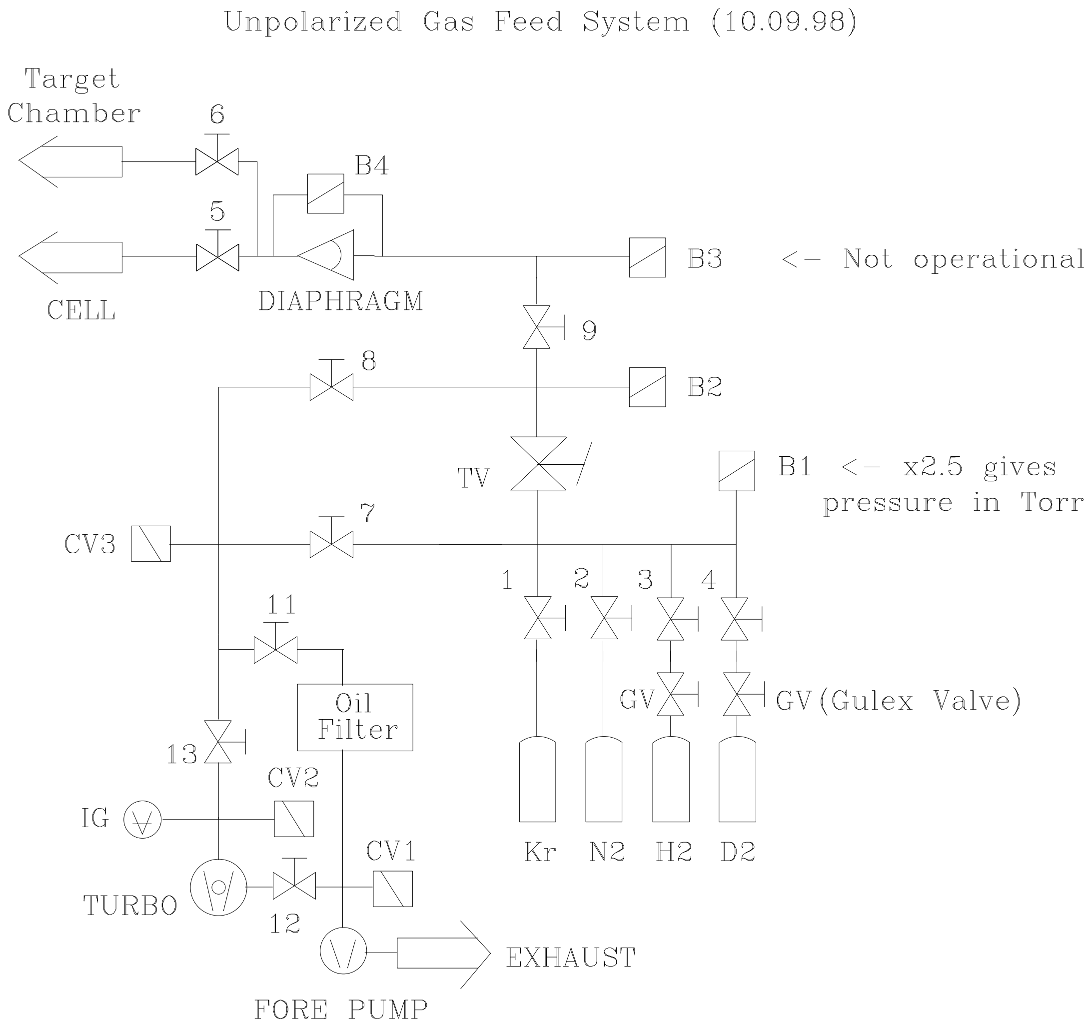

Figure 2-7: Schematic diagram of the HERMES UGFS on Sept 10, 1998. Displayed in the figure are the locations of solenoid valves (numbered 1 through 13), Gulex valves (labeled GV), a thermovalve (TV), a diaphragm, Convectron pressure gauges (labeled CV1 through CV3), Baratron pressure transducers (labeled B1 through B4), an ion gauge (IG), and bottles filled with different gases (in this case, krypton, nitrogen, hydrogen, and deuterium). Also displayed are possible ways for gases to leave the system (through the target chamber, target cell, or exhaust), and the turbo and fore pumps for the system.

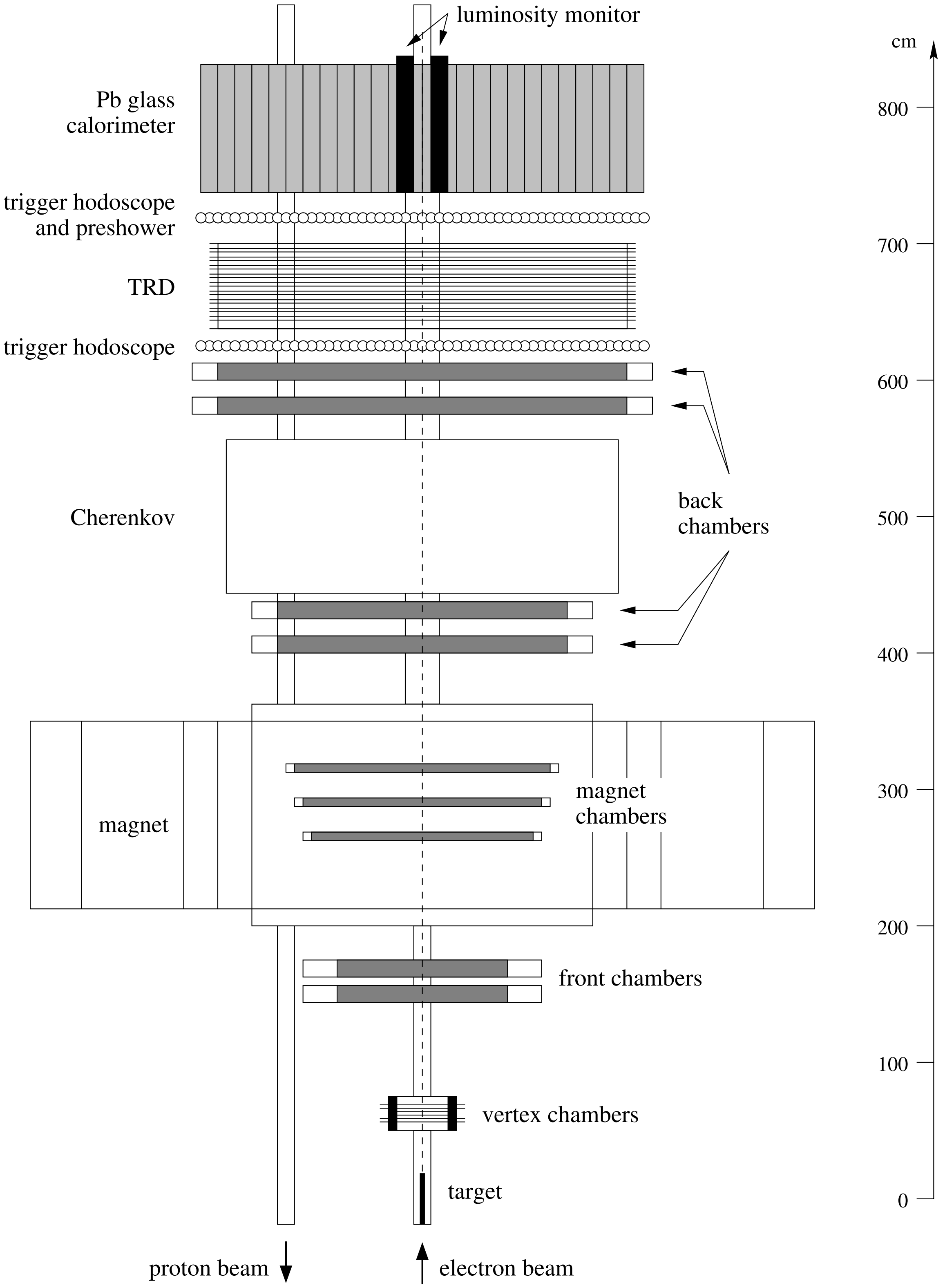

Figure 2-8: The HERMES spectrometer (top view).

the experiment, starting from the target and proceeding downstream are: the vertex chambers (VC), the drift vertex chambers (DVC) (not shown in Fig. 2-8), the front chambers (FC), magnet chambers (MC), and the back chambers (BC). In addition to the tracking chambers, HERMES has several detectors designed specifically for particle identification (PID). The PID detectors are the transition radiation detector (TRD), the gas threshold Čerenkov, the preshower detector, and the electromagnetic calorimeter.

2.3.1 Tracking Chambers

The characteristics of the tracking chambers are described in detail in Ref. [71]. Only the main features are covered here. A summary of the characteristics of each tracking chamber may be found in Table 2.2.

The tracking system is used to determine event vertices, to measure scattering angles for kinematical reconstruction, to measure the particle momentum from track deflection in the spectrometer dipole magnet and to match up tracks with hits in the PID detectors.

The vertex chambers (VC1/2) are microstrip gas counters (MSGC) and are used to provide measurements of scattering angles and vertex positions. In a microstrip gas counter, cathodes and anodes are etched on a substrate of high resistivity. This allows for a smaller cell size than conventional counters. In the front region, it is also necessary to use low-Z materials to minimize showering into the downstream elements of the spectrometer. The MSGC design removes the need for wire chamber frames so that the chambers can be placed close to the beam pipe. The upper and lower VC's each consist of six planes separated into two modules VC1 and VC2.

The drift chambers (DVC, FC, and BC) are of conventional design. Each layer of cells consists of a plane of alternating anode and cathode wires between two cathode foils. The cathodes are at negative high voltage while the anode sense wires are at ground. Each of the upper and lower DVC, FC1, FC2, and BC1-4 contains six planes.

CHAMBER	Vertex		Drift Vertex	Front		Magnet			Back	
Detector name	VC1	VC2	DVC	FC1	FC2	MC1	MC2	MC3	BC1/2	BC3/4
mm from target	731	965	1100	1530	1650	2725	3047	3369	4055	5800
Active Area:										
Horizontal (mm)	323	393	474	660	660	996	1210	1424	1880	2890
Vertical (mm)	137	137	290	180	180	263	306	347	520	710
Cell design	microstrip gas		horizontal-drift	horizontal-drift		MWPC			horizontal-drift	
Cell width (mm)	0.193		6	7		2			15	
A-C plane gap (mm)	3		3	4		4			8	
Anode (A) material	200 μm glass(Al)		W(Au)	W(Au)		W(Au)			W(Au)	
Anode wire diameter	7 μm		30 μm	20 μm		25 μm			25 μm	
Potential wire mat'l	Al strip		Be-Cu(Au)	Al(Au)					Be-Cu(Au)	
Potential wire dia.	85 μm		50 μm	50 μm					127 μm	
Cathode (C) material	Al on glass		Al on Mylar	Al on Mylar		Be-Cu wires			C on Kapton	
Cathode thickness	200 μm		34 μm	6.4 μm		90 μm 0.5 mm pitch			25.4 μm	
Gas composition:	DME/Ne		$Ar/CO_2/CF_4$	$Ar/CO_2/CF_4$		$Ar/CO_2/CF_4$			$Ar/CO_2/CF_4$	
(%)	50/50		90/5/5	90/5/5		65/30/5			90/5/5	
U,V stereo angle	$+5°, -90°$		$\pm 30°$	$\pm 30°$		$\pm 30°$			$\pm 30°$	
Resolution/plane (σ)	65 μm		220 μm	225 μm		700 μm			275 μm	300 μm
Wires in X plane	1674	2046	80	96	96	496	608	720	128	192
Wires in U,V plane	2170	2170	96	96	96	512	608	720	128	192
Module config.	VUX	XVU	XX'UU'VV'	UU'XX'VV'		UXV			UU'XX'VV'	
Rad. length/module	0.8%		0.25%	0.075%		0.29%			0.26%	
Number of modules	1	1	1	1	1	1	1	1	2	2
(upper or lower)										
Channels/module	6014	6386	544	576	576	1520	1824	2160	768	1152
Total channels	24800		1088	2304		11008			7680	

Table 2.2: Tracking Chamber properties (from Ref. [71]).

The drift vertex chambers (DVC) were installed in 1997 to provide additional redundancy in the front region and to enlarge the acceptance of the front region for the HERMES charm upgrade program [1].

The front drift chambers (FC1/2) provide spatial resolution in front of the magnet necessary for good angular resolution. They are also necessary for accurate momentum reconstruction, as they constrain the track before the bend in the dipole magnet.

The back drift chambers (grouped into two sets BC1/2 and BC3/4) provide spatial resolution after the spectrometer magnet. This is necessary for precise momentum determination. The back chambers also match the track in the back region with hits in the PID detectors for accurate identification of the particle.

The magnet chambers (MC1/2/3) are proportional wire chambers located in the gap of the magnet. They were intended to resolve ambiguities in cases of high track multiplicities. However, they were found to be unnecessary for this purpose, due to low backgrounds. They are now primarily used for momentum determination of low energy particles that are bent out of the spectrometer acceptance by the magnet. An example is in the decay of the Λ to a pion and a proton, where the proton is not seen in the back region.

A laser alignment system [73] is used to continuously monitor the relative alignment of the tracking system, to monitor detector shifts during operation and after possible replacement or maintenance.

The HERMES reconstruction code (HRC) [75] is used to reconstruct tracks from detector hits and assign angle, momentum, vertex, and particle identification quantities to each track. HRC uses a tree-search algorithm for fast track finding and a look-up table for fast momentum determination, and will be discussed in greater detail in chapter 3.

The HERMES Monte Carlo (HMC) program is based on the GEANT [76] software package and was used to estimate the tracking resolution of the detector. This was done by fitting Gaussians to the difference of reconstructed vs. generated quantities.

The average momentum resolution for the average kinematics of the experiment was determined to be roughly 1% and the angular resolution was determined to be less than 0.6 mrad. The Monte Carlo simulation of the deep-inelastic scattering process shows excellent agreement with the data.

2.3.2 Particle Identification Detectors

The electromagnetic calorimeter is used to detect electromagnetic showers of electrons and photons. This is useful for discriminating between electrons and hadrons, and for detecting photons and measuring their energies. The calorimeter is constructed of two sections of 420 lead-glass blocks stacked in a 42×10 array above and below the beam. The blocks present an area of 9×9 cm^2 and are 50 cm (about 18 radiation lengths) long. The blocks are optically isolated from one another using aluminized mylar foil and tedlar foil. Behind each block is a photomultiplier tube which collects the light from the block. To minimize radiation damage, the calorimeter arrays are moved away from the beam pipe during injection into the HERA ring. The response of the calorimeter to electrons was found to be linear within 1% over the energy range 1-30 GeV. The central value of the ratio of electron energy deposited in the calorimeter to electron momentum determined from the bend in the spectrometer magnet E/p is found to be 1.00 ± 0.01 and is stable against time. The calibration is checked by reconstructing the π^0 mass and width, which is found to be in agreement with the particle data group value. The calorimeter is described in detail in Ref. [72].

Three scintillator hodoscopes are used in the experiment: H0, H1, and H2. H0 is a single sheet of plastic scintillator, located upstream of the FC's, that is used to reduce backward-going showers produced by the proton beam. This is done using time of flight with the rear scintillators H1/2. H1 and H2 are located in the back region and are used with H0 to provide trigger signals. H2 is preceded by 11 mm (two radiation lengths) of lead between two 1.3 mm stainless steel sheets. This allows some discrimination between positrons and pions, because pions will typically deposit

2 MeV while positrons will deposit 20-40 MeV.

The transition radiation detector (TRD) uses X-rays produced by transition radiation of positrons passing through the detector. Transition radiation is emitted whenever a charged particle passes suddenly from one medium to another [77]. At HERMES energies, only positrons will produce transition radiation in the X-ray range, thus allowing separation from hadrons. The TRD uses six planes above and below the beam of loosely packed propylene fibers with 17-20 μm diameters as radiators. Each plane is 6.5 cm thick and 325×75 cm^2 in cross section. Behind each radiator is a proportional wire chamber which detects the X-ray(s) emitted in passing through the radiator. Each chamber is 2.54 cm thick, has 256 vertical wires separated by 1.27 cm, and is filled with Xe/CH_4(90:10) (an efficient mixture for X-ray absorption). The cathode foils are 50 μm thick aluminized mylar. Both positrons and hadrons will deposit some energy in the TRD, due to ionization of the chamber gas. Pions deposit typically 11 keV while positrons deposit about twice this amount. Good separation of positrons and hadrons requires combining the signals of the six modules.

A charged particle will emit Čerenkov radiation if its velocity exceeds the speed of light in the medium through which it is traveling. The gas threshold Čerenkov counter is located between the two sets of BC planes. It is used primarily for pion identification above a threshold energy. The Čerenkov uses a gas mixture of N_2/C_4F_{10}(70:30), giving thresholds for pions, kaons, and protons of 3.8, 13.6, and 25.8 GeV, respectively. The depth of the gas volume is 1.17 m. Each detector half has an array of 20 spherical mirrors which focus the Čerenkov light onto an array of phototubes. In 1998, the Čerenkov was upgraded to a dual-radiator ring-imaging Čerenkov for π/K/p separation over the full momentum range [78].

For each track, the four detector responses are combined using a likelihood method to determine whether the particle was a positron or a hadron. The likelihood variable

PID3 combines the responses of the calorimeter, preshower, and Čerenkov detector:

$$\mathrm{PID3} = \log_{10}\left[\frac{P^e_{\mathrm{Cal}}P^e_{\mathrm{Pre}}P^e_{\mathrm{Cer}}}{P^h_{\mathrm{Cal}}P^h_{\mathrm{Pre}}P^h_{\mathrm{Cer}}}\right]. \tag{2.9}$$

Here, P^i_j is the probability that the signal observed in detector j originated from a particle of type i. The TRD is included in its own PID variable:

$$\mathrm{PID5} = \log_{10}\left[\frac{P^e_{\mathrm{TRD}}}{P^h_{\mathrm{TRD}}}\right]. \tag{2.10}$$

The probability functions P^i_j are determined by simply comparing the signal from detector j to typical detector responses for each detector called parent distributions. The parent distributions for the positron and hadron responses are determined either from the data (by using the other three detectors to determine the identity of the particle, then looking at the distribution for the detector in question) or from Monte Carlo simulation of the detector. The parent distributions are taken to be momentum dependent due to e.g. the momentum dependence of the positron transition radiation peak. Normally, a cut on the sum PID3+PID5 of the particle is placed. Positive PID3+PID5 indicates that the track is likely an electron (or positron) while negative PID3+PID5 indicates that the track is likely a hadron. Efficiencies and contaminations must be estimated with parent distributions and relative fluxes of particles for the PID cut used.

Time of flight information from H1/2 may also be used to separate pions, kaons, protons, and deuterons for momenta up to about 2 GeV in energy [79, 80].

2.4 The Luminosity Monitor

An absolute measurement of the luminosity accumulated by the experiment is possible using the luminosity monitor. The luminosity monitor detects e^+e^- coincidences from Bhabha scattering of the incident positrons off target gas electrons. The cross section and radiative corrections for this process are known very precisely. The e^+e^- pairs are detected in two calorimeters mounted left and right of the beam axis, just outside the beam pipe, 7.2 m downstream of the target. The calorimeters are constructed from several $NaBi(WO_4)_2$ Čerenkov crystals each of size $22 \times 22 \times 200$ mm^3 stacked in a 3×4 array. Despite the large radiation hardness of these detectors (7×10^5 Gy), the calorimeters are moved away from the beam pipe during injection to protect against radiation damage. Each crystal is optically isolated from the next with aluminized mylar and optically coupled to a photomultiplier. For 27.5 GeV positrons, the symmetric scattering angle is 6.1 mrad. The calorimeters have horizontal acceptances of 4.6 to 8.9 mrad. Bhabha coincidences are identified by requiring at least 5 GeV to be detected in each calorimeter. This allows the separation from the dominant background, where a significant amount of energy is measured in only one detector. The luminosity monitor provides a measurement of the luminosity with a statistical precision of roughly 1% in 100 s. The systematic error in an absolute measurement of the luminosity is about 6% [81].

The luminosity monitor can also be used to measure the Bhabha asymmetry. In 1996 and 1997, several positron fills were dedicated to measuring this asymmetry as a check of the calibration of the BRP and TGA target subsystems. Electron polarized states were injected into the target cell and analyzed with the TGA and BRP. The Bhabha asymmetry measured using the luminosity monitor is proportional to $\alpha_r P_e$. The measurements were found to agree [81].

2.5 Triggers

Two types of triggers were used for physics analysis in 1996 and 1997. These will be referred to as the "DIS" trigger and the "photoproduction" trigger.

The DIS trigger requires a coincidence of signals in all three scintillator hodoscopes with a minimum energy in two adjacent columns of the calorimeter, in time with a signal from the accelerator indicating that a beam bunch was present (the HERA clock). The goal of the DIS trigger is to attempt to identify scattered positrons in the detector using the calorimeters; however this trigger has a significant contamination from events where hadrons deposit sufficient energy to trigger the calorimeter. In 1996, the calorimeter threshold was reduced from 3.5 GeV to 1.4 GeV, increasing this contamination. The goal of the reduction was to increase the energy range of scattered positron detection. Due to the contamination by hadrons, and the requirement of the high-p_T hadron analysis for the hadrons to occur in pairs, this trigger is found to have a large efficiency for the detection of the hadron pairs.

The photoproduction trigger requires a coincidence of signals in the three scintillator hodoscopes with a signal from the BC1 chamber and the HERA clock. The photoproduction trigger also requires a coincidence in the top and bottom of the detectors, so that at least two tracks must be seen in the spectrometer acceptance: one in the top spectrometer half and one in the bottom. In 1997, this trigger was improved by including more BC1 planes into the trigger logic. This increased the efficiency for detecting a track in each of the top and bottom halves. The goal of this trigger was to enchance the observation of decaying particles such as ρ, J/Ψ, D$^{*\pm}$, and D^0 which decay into two or more charged particles at large enough opening angle for each to be detected in one spectrometer half. In this case, the scattered positron need not be observed in the acceptance, and it is assumed that the positron was scattered at too small an angle to be detected. As will be seen, this trigger is also useful for the detection of high-p_T hadron pairs.

Chapter 3

Analysis

This chapter begins with a description of the analysis chain for the data, leading up to the extraction of an asymmetry and cross section. The measurement of the asymmetry and cross section in high-p_T hadron photoproduction will be of special interest.

3.1 Data Reduction

3.1.1 Step 1: Writing the data to tape

The HERMES data acquisition system (DAQ) is described in detail in Ref. [82]. Events are written to tape in the form of signals from each of the various detectors for each triggered event. These consist essentially of pulse height and timing information read from ADC and TDC modules, respectively.

Several other useful sources of data are recorded at a rate much slower than the event rate. For example, "scaler events" are read out every 10 seconds. Examples of scaler information are counts of the number of triggers generated and accepted, and the number of counts recorded by the luminosity monitor. This 10 second period is referred to as a "burst". Most slow control information is synchronized to this rate.

Additional information is written to tape in the form of "user events". User events are asynchronous data sent by a particular detector or subsystem monitoring program. Examples of data that are written as user events are target and high voltage information.

All this information is stored in a single EPIO (Experimental Physics Input Output) format file on a run-by-run basis. One run is typically six minutes of real-time data taking.

The other type of data available online is slow control information. Using Fortran or C codes to communicate with Camac or RS232 modules in the electronics trailer allows for slow control and monitoring of HERMES subsystems. The slow control tasks get their information to tape either by sending it via a user event to the DAQ, or by sending it to a Distributed ADAMO Database (DAD) [83] server. ADAMO (Aleph Data Model) [84] is an entity-relationship based database library which is used to manage most data structures at HERMES. The DAD server is then read by a "taping client". The taping client stores the data with time stamps in DAD format for easy retrieval and synchronization with the events from the EPIO files created by the DAQ. The result is a file for each positron fill (a "fill file") that contains the taped slow control information for the entire fill. The taping client also records information from certain tables even when there is no positron beam in the ring. This is useful for systems that do not necessarily require the beam in order to function (e.g. the target systems, which typically use time without beam for calibration measurements).

3.1.2 Step 2: Removing the data from tape and translating it into useable form

The flow of data after it is written to tape is sketched diagramatically in Fig. 3-1. The elements of the data production scheme will now be described in greater detail.

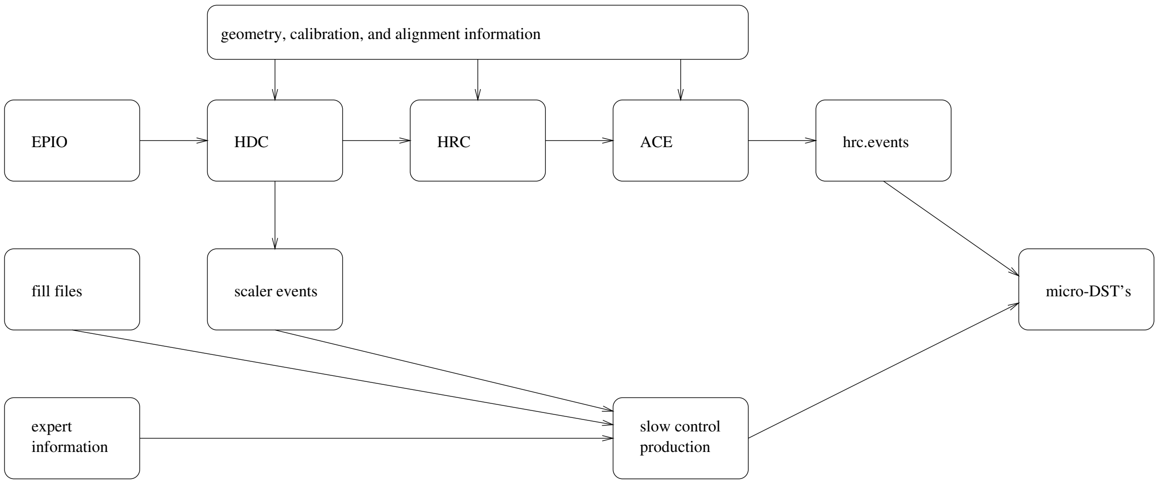

Figure 3-1: The HERMES production scheme. Note that some steps are recursive. For example, some "expert information" and "calibration and alignment information" comes only after a full production.

HDC

The EPIO format files are read using the HERMES decoder program (HDC). This program takes the pulse height and timing information for each detector and converts it into position and energy values using mapping, calibration, and geometry from HERMES analysis servers. These values can be stored in a DAD or ADAMO format file, or can be piped directly to the HERMES reconstruction program (HRC). HDC can also be used online to send data to online monitors. In addition to decoding each triggered event, HDC decodes the scaler and user events and places them in separate files which are combined later into the slow-control production.

HRC

HRC is the next step and is described in detail in Ref. [75]. HRC takes the output of HDC and uses calibration and geometry information to identify tracks. The program has two important time-saving features: a pattern recognition algorithm used to identify tracks, and a fast momentum look up code used to determine the momentum of the tracks.

The pattern recognition algorithm is called Treesearch. The digitized pattern of hits in the detectors is compared with a pattern of reduced resolution. In the first step, this is a simple left or right half of the detector comparison. The resolution of each detector is then doubled and the pattern of hits in the detectors is compared to "child" patterns of the first accepted "parent" pattern. The resolution is recursively doubled until the resolution reaches the typical resolution of the detector. The algorithm is made stable against chamber inefficiencies by reducing the level of agreement required with the pattern (e.g. 3 out of 4 hits). The algorithm is made stable against uncertainties in chamber or wire positions by automatically broadening patterns based on the input resolutions of the detectors.

HRC determines the momentum of the tracks by means of a look up table. Five hundred thousand electron and positron trajectories with unique vertex, angle, and momenta are tracked through the magnet using an input magnetic field map. This is used to create a matrix mapping $\Delta x'_{ijkl}$ where the four indices are the z-vertex, θ_x, θ_y, and momentum of the generated track. Here, $\Delta x'$ is the horizontal slope change of the track as it passes through the magnet, and is therefore the most sensitive to the momentum of the four matrices constructed by the trajectory generation: $\Delta x'$, $\Delta y'$, Δx, and Δy. The x and y offsets and the change in the y slope are all relatively small, as expected. As long as the magnetic field mapping doesn't change, the matrix need not be regenerated.

HRC also performs a few other functions. It extrapolates the distance of closest approach of the front track to determine a vertex position and a transverse vertex. It combines signals from calorimeter clusters that are near to one another to determine the total energy deposited for each track.

ACE

The output of HRC is fed to ACE (Alignment, Calibration, and Efficiency Program). ACE is described in detail in Ref. [64]. ACE calculates the efficiency of each plane in the tracking chambers by using tracks found by HRC. Care is taken that the algorithms used by HRC do not bias the efficiencies calculated by ACE. Plane efficiencies were found to be typically 90% to 95% for polarized data taking. The efficiencies determined by ACE were not used for this analysis.

The HDC/HRC/ACE chain is in principle iterated, to account for better knowledge of relative detector alignment and improved calibration of the various detectors. This results in different versions or "productions" of the data set.

slow control and μDST production

The output of HRC, ACE, and the slow control fill files is now in an analyzeable state, for experts. The output of these three programs is used by experts from each subsystem to perform analysis of their particular detector. For example, the target group uses information from data taken between fills to extract contributions to α_0. Additional information can come from external sources such as log books.

The resultant information is synchronized in time at the burst level with information from the slow control fill files and scaler information decoded by HDC, and placed into a modified fill file that contains all the slow (non-event-level) information for the experiment.

The final step before physics analysis is to combine this slow information with the tracks found by HRC. The result is a micro data set tape (μDST). All information that is not directly related to physics analysis is discarded from the data set at this level. Depending on the physics analysis desired and the level of systematic studies to be done, the data can be further filtered into smaller data sets based on kinematical cuts. The resulting nano-DST's are useful for analyses highly specialized and already well-understood.

The μDST's were used for the analysis in this thesis, as the dataset required is not the usual deep-inelastic scattering dataset found in typical nano-DST's. The DST production versions used were the 96c1 and 97b2 productions.

The μDST's contain several important new sources of information from various groups, useful for extracting asymmetries. The most important consideration in the measurement of an asymmetry is that there are no fluctuations on time scales shorter than the time between reversals of the target polarization. For this reason, statistical fluctuations in the measured values for the quantities necessary to normalize the asymmetry, the beam polarization, the target polarization, and the luminosity monitor rate, can create systematic errors in the measurement of the asymmetry (if their statistical errors are not taken into account properly). To remove this possible error, fitted values of the beam polarization and luminosity monitor rate are used, which remove the statistical error in point by point measurements of these quantities. The target polarization need not be fitted since target polarizations are determined to good precision for relatively long (roughly five minutes) times as the ABS and BRP switch through the different possible states.

3.1.3 Step 3: Physics analysis of the data

For the physics analysis presented in this thesis, the analysis code darKnight [85] (dk) was used. dk is a combination of C and Fortran routines that reads μDST's. The code features the ability to read most currently known formats of files including μDST files, HRC files, HMC files, and arbitrary ASCII files. The code can also currently understand all possible versions of μDST's. Another important feature of dk is its interface to the Histogram and Test Package (HAT) [86], which is used for output of physics quantities calculated inside the code. HAT was also used for the Monte Carlo predictions of Chapter 4, lending continuity to the MC and dk analyses.

3.2 Data Quality

Only data found to be of good quality were analyzed. "Good" data quality implies that, to the best of the experimenters knowledge, all equipment in the experiment is functioning correctly.

Fills and runs were selected for analysis based on the data quality determined in the analysis of g_1^p in 1996 and 1997 [87]. This first level data quality is based largely on the online logbook kept by the shift crew, and on known problems recorded in the paper logbook and checked by hand. One analyzeable period in 1997 was excluded from the analysis presented in this thesis for ease of analysis. This period was a short time (roughly two weeks) of data taking where the beam polarization was reversed (by changing the spin rotators up- and down-stream from the HERMES experimental site) compared to the orientation for most of the 1997 data taking. The effect of including or not including this data set was negligible.

The data quality (DQ) cuts that were applied were the standard cuts for the experiment and are based on problems encountered during running and found in the data during analysis. The requirement made at the μDST level is simply that the data quality bitsets `bg1DQTop` and `bg1DQBot` have no bits set. The data quality requirements implied by this are as follows [88]:

- Simple burst level DQ:
  - target is in a well-defined polarization state
  - beam polarization is within the range 0.30 to 0.80
  - DAQ deadtime is in a reasonable range (0.5 to 1.0)
  - burst length is in a reasonable range (0.0 to 11.0 s)
  - beam current is in a reasonable range (5.0 to 50.0 mA)
  - luminosity monitor rate is in a reasonable range (5.0 to 60.0 Hz)
- Synchronization checks on the DAQ

  - last burst in a run is cut if there was a burst number jump or if this was at the end of a fill.
  - event and slow data are synchronized (checked when target spin reversal occurs, and at start and end of burst)
  - target spin reversal event (signalled by a 1203 user event) is not missing
  - DAQ clock is not zero
  - no burst number jumps
  - no backward jumps in the event number

- Logbook DQ, as determined from the `logrun.new` file maintained by the shift crew during data taking. This file contains brief information on target status and data taking for each run.
  - run is "analyzeable", i.e. no unrecoverable problems were plaguing the experiment, and run was not a test run of some sort
  - polarized ^{1}H target was in operation

- Target DQ
  - UGFS gate valve is closed, i.e. no unpolarized target was being injected into the cell
  - ABS, BRP, and TGA are on and functioning correctly
  - target magnetic holding field is switched on
  - calibrated α_r, and P_{target} values are available

- Detector DQ
  - calorimeter, preshower, luminosity monitor have no dead blocks due to trips (from HERMES Gain Monitoring System, GMS)
  - TRD is working properly

– no high voltage trips detected in the VC's, DVC's, FC's, or BC's

The above DQ requirements are for the 97b2 μDST's. The 96c1 μDST's have a few slightly different requirements. They additionally contain data quality checks on the transverse polarimeter and the Čerenkov as supplied by the groups responsible for these apparati. In 1996, the high voltage trip checking is of course only done for the FC's and BC's, as the VC's were not functioning most of the time in 1996 and were therefore not used in track reconstruction, and the DVC's were not yet installed.

3.3 Extraction of an Asymmetry

The cross section asymmetry to be measured is defined as:

$$A_{||} = \frac{d\sigma^{\uparrow\downarrow} - d\sigma^{\uparrow\uparrow}}{d\sigma^{\uparrow\downarrow} + d\sigma^{\uparrow\uparrow}} \tag{3.1}$$

where the first arrow indicates the beam polarization and the second arrow indicates the target polarization. The cross section asymmetry is extracted from experimental quantities as follows:

$$A_{||} = \frac{N^- L^+ - N^+ L^-}{N^- L_P^+ + N^+ L_P^-}. \tag{3.2}$$

Here $N^+(N^-)$ is the number events selected by the particular analysis for spin parallel (anti-parallel) to the beam spin orientation. The deadtime corrected luminosity for each target spin state is

$$L^{\pm} = \sum_{\pm\text{ spin state bursts}} (dL/dt) \cdot \epsilon \cdot \Delta t \tag{3.3}$$

where dL/dt is the luminosity monitor rate, ϵ is the DAQ livetime, and Δt is the length of time for the burst. The quantity $L_P^{\pm}$ is additionally weighted by the product of the beam and target polarization values for each spin state:

$$L_P^{\pm} = \sum_{\pm \text{ spin state bursts}} (dL/dt) \cdot \epsilon \cdot \Delta t \cdot (P_B P_T). \tag{3.4}$$

The DAQ livetime is calculated from the sum over all triggers of the number of triggers accepted divided by the number of triggers generated, for the burst in question. The luminosity and beam polarization quantities used for the integration are the fitted values mentioned before.

In analyzing the data, it was found that the luminosity monitor rate dL/dt had a small asymmetry. The luminosities were corrected for a small Bhabha cross section asymmetry caused by a roughly 3% residual polarization of the electrons in the target.

The luminosity monitor rate asymmetry is determined using the formula [89]:

$$A_L = \frac{N_L^+ - N_L^-}{N_L^+ + N_L^-}, \tag{3.5}$$

where

$$N_L^{\pm} = \frac{\sum_{\pm \text{ spin state bursts}} (dL/dt) \cdot \epsilon \cdot \Delta t}{\sum_{\pm \text{ spin state bursts}} I \cdot \epsilon \cdot \Delta t}, \tag{3.6}$$

where I is a normalization quantity which cannot have an asymmetry, the positron beam current. The value for this asymmetry in 1996 was typically A_L=0.003 [89]. In 1997, the target cell quality, to which the electron polarization is most sensitive, improved and the luminosity monitor rate asymmetry increased to roughly A_L=0.006. This value can be compared to the raw asymmetries for the DIS data of the order 0.06 to 0.07. The effect on $A_{||}$ can be quantified by correcting the raw luminosity monitor rate measured for each spin state:

$$A_{||} = \frac{(1 - A_L)N^- L^+ - (1 + A_L)N^+ L^-}{(1 - A_L)N^- L_P^+ + (1 - A_L)N^+ L_P^-}. \tag{3.7}$$

Another way to correct for the luminosity monitor rate asymmetry is to simply use equation (3.2) with the modification that the fitted luminosity monitor values should be used for the determination of $L^{\pm}$, as opposed to the raw values. In this procedure, the drop in luminosity monitor rate within a fill is fitted to a decaying exponential, independent of the target polarization. Thus, the fitted rate has no asymmetry. For the results of this thesis, this method of correcting $A_{||}$ was used.

The difference between the two methods of correcting $A_{||}$ for the luminosity monitor rate asymmetry was determined to be less than 0.2%. This is negligible compared to the beam and target polarization systematic uncertainties.

3.4 Systematic Uncertainty for $A_{||}$

The dominant contributions to the systematic uncertainty for $A_{||}$ come from systematic uncertainties associated with the measurement of the beam and target polarizations. Effects due to kinematical smearing were found to be small for the specific case of high-p_T hadron pairs, and will be discussed in section 3.5.4.

3.4.1 Beam Polarization Systematic Uncertainty

The beam polarization systematic uncertainty was determined in Ref. [44]. The absolute calibration of the beam polarization must be determined from "flat machine running" where the spin rotators are removed in an attempt to minimize horizontal magnetic fields in the HERA ring. This calibration was performed in 1994. The rise of the polarization with time was monitored in several fills with the machine in this state. The uncertainty in the scale of the polarization was determined to be $\delta P_{\text{scale}}/P = 3.26\%$. From non-statistical variation of the beam polarization in each year (so-called "point-to-point" instability), another error has been assigned: $\delta P_{\text{point}}/P = 0.9$ %. Adding these errors in quadrature gives a beam polarization uncertainty of $\Delta P_{\text{beam}}/P_{\text{beam}} = 3.4\%$.

3.4.2 Target Polarization Systematic Uncertainty

The target polarization uncertainty is dominated by uncertainties in the sampling corrections, and the lack of knowledge of the polarization of the molecules in the target. The relevant quantities to which uncertainties must be assigned are (from section 2.2.1) c_α, c_P, and β.

From equation (2.6), it can be seen that the error due to variation of β will depend highly on the value of α_r. Similarly, the uncertainties due to the sampling corrections c_α and c_P get considerably smaller when α_r^{TGA} and $P_{\mathrm{atom}}^{\mathrm{BRP}}$ are large, since only recombination and depolarizing effects can occur.

In 1996, when the ^{1}H target had just been commissioned, the molecular recombination in the target cell was large and uncertainties due to c_α and β were consequently large, giving a target polarization uncertainty of about 12%. In 1997, several improvements in the operation of the target were made in order to maximize α_r, thereby maximizing the target polarization while minimizing the error in its determination. The target polarization uncertainty for 1997 was 4.5%.

To reduce the error in the 1996 target polarization, the inclusive DIS asymmetry was compared between the data taking years 1996 and 1997. The renormalization factor required to make the x-dependent DIS asymmetry in 1996 agree with the 1997 asymmetry was determined. The renormalization factor was determined to the level of 4%, this uncertainty being dominated by the statistical precision of the comparison. Adding this in quadrature with the 4.5% determined for 1997 gives a 1996 target polarization systematic of 6% [44].

3.4.3 The Total Systematic Uncertainty on $A_{||}$

Combining the beam and target polarization systematic uncertainties in quadrature gives the total systematic error on $A_{||}$. It is 7% for 1996 and 6% for 1997. Frequently, the 1996 and 1997 results for $A_{||}$ will be averaged statistically. Since the

1997 data contains more statistics than the 1996 data set, the systematic error for the combination will be close to 6%.

3.5 High-p_T Hadron Pairs

The analysis specific to the study of high-p_T hadron pairs will now be discussed.

3.5.1 Data Selection

Hadrons were identified by the PID cut pid3+pid5 < -2. Positrons were identified by the cut pid3+pid5 > 0. The baseline event level cuts used to select the high-p_T hadrons are:

- At least two hadrons of opposite charge must be observed in the event.
- There must be no positron observed in the event.
- Each of the leading hadrons for each charge type must satisfy the following additional cuts. (In this case leading means that the hadron in question has a higher momentum than all the other hadrons of the same charge.)
  - vertex cuts: It was required that -18 cm $<$ z-vertex $<$ 18 cm and $|$t-vertex$| < 0.75$ cm. Here z-vertex refers to the point at which the distance of closest approach of the front track to the beam axis, and t-vertex refers to the transverse distance at that point of closest approach. These cuts therefore restrict the hadrons to originate from inside the target cell. Additionally, it was required that the z-vertex difference between the two hadrons be less than 5.0 cm, i.e., that they originate from the same vertex.
  - kinematical cuts: It was required that the momentum p of each hadron be greater than 4.5 GeV/c and that the transverse momentum p_T of each hadron be greater than 0.5 GeV/c. These cuts ensure that the hadrons

are forward $x_F > 0$ and of relatively high p_T. The mass of the assumed two-pion system $M(2\pi)$ was required to be greater than 1.0 GeV/c^2 to cut out vector-meson decays from the sample. This cut effectively reduces contributions from $\rho(770)$ and $\phi(1020)$ mesons from the sample. The ϕ meson contributions are reduced despite its higher mass because, for its dominant decay into two charged kaons, the opening angle between the kaons is small resulting in a smaller mass if the kaons are to be pions. As a result the ϕ meson shows up at even smaller $M(2\pi)$ than the ρ meson. Contributions from vector mesons were attempted to be minimized because they have a large cross-section in the photoproduction regime which cannot be perturbatively calculated in QCD.

The goal of these kinematical cuts is to begin to attempt to isolate hadron pairs originating from the outgoing $q\bar{q}$ produced in PGF.

3.5.2 Measured Asymmetries

The analysis of the asymmetries is described in several HERMES internal documents [90, 91, 92, 93]. The studies conducted are summarized here.

The p_T cuts and $M(2\pi)$ cuts were varied throughout the allowed phase space of the two hadron system to study the effect on the asymmetry and cross-section. The result for the asymmetry $A_{||}$ when varying the p_T of the leading hadrons of each charge type h^+ and h^- is shown in Fig. 3-2. This figure shows $A_{||}(p_T^{h^+}, p_T^{h^-})$ as a function of $p_T^{h^+}$ for a certain bin in $p_T^{h^-}$. The four panels correspond to four bins used for $p_T^{h^-}$: 0.8 GeV/c$< p_T^{h^-} <$1.0 GeV/c, 1.0 GeV/c$< p_T^{h^-} <$1.2 GeV/c, 1.2 GeV/c$< p_T^{h^-} <$1.5 GeV/c, and $p_T^{h^-} >$1.5 GeV/c. The five points in each panel correspond to bins in $p_T^{h^+}$: 0.5 GeV/c$< p_T^{h^+} <$0.8 GeV/c, 0.8 GeV/c$< p_T^{h^+} <$1.0 GeV/c, 1.0 GeV/c$< p_T^{h^+} <$1.2 GeV/c, 1.2 GeV/c$< p_T^{h^+} <$1.5 GeV/c, and $p_T^{h^+} >$1.5 GeV/c. The true upper limit on the p_T of a particle is limited by the statistics accumulated by the experiment at

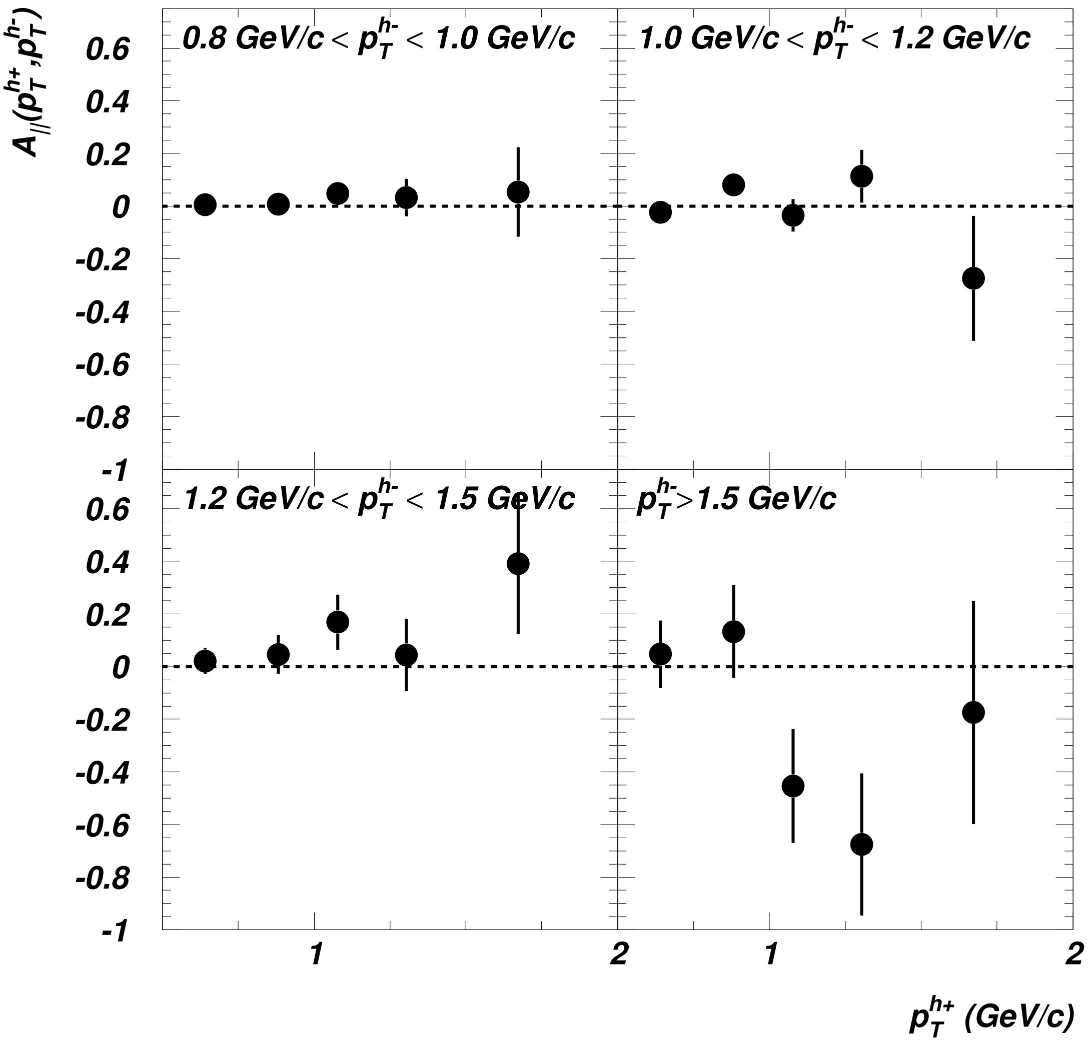

Figure 3-2: $A_{||}(p_T^{h^+}, p_T^{h^-})$ for HERMES 1996 and 1997 data combined.

this time. An upper limit of 2.5 GeV/c was enforced, even though this upper limit doesn't appear on the graph. Relaxing the upper limit had a negligible effect on the uppermost data points. Each data point is plotted at the average $p_T^{h^+}$ for the particular bin. The asymmetry data is presented in tabular form in Table 3.1.

$p_T^{h^-}$ range (GeV/c)	$p_T^{h^+}$ range (GeV/c)	$A_{\|\|}(p_T^{h^+}, p_T^{h^-})$
$0.5-0.8$	$0.5-0.8$	0.017 ± 0.007
$0.5-0.8$	$0.8-1.0$	0.004 ± 0.013
$0.5-0.8$	$1.0-1.2$	0.006 ± 0.025
$0.5-0.8$	$1.2-1.5$	0.018 ± 0.045
$0.5-0.8$	> 1.5	-0.039 ± 0.120
$0.8-1.0$	$0.5-0.8$	0.005 ± 0.013
$0.8-1.0$	$0.8-1.0$	0.007 ± 0.023
$0.8-1.0$	$1.0-1.2$	0.048 ± 0.041
$0.8-1.0$	$1.2-1.5$	0.032 ± 0.071
$0.8-1.0$	> 1.5	0.053 ± 0.170
$1.0-1.2$	$0.5-0.8$	-0.025 ± 0.026
$1.0-1.2$	$0.8-1.0$	0.081 ± 0.041
$1.0-1.2$	$1.0-1.2$	-0.036 ± 0.061
$1.0-1.2$	$1.2-1.5$	0.113 ± 0.100
$1.0-1.2$	> 1.5	-0.275 ± 0.237
$1.2-1.5$	$0.5-0.8$	0.021 ± 0.049
$1.2-1.5$	$0.8-1.0$	0.047 ± 0.073
$1.2-1.5$	$1.0-1.2$	0.169 ± 0.105
$1.2-1.5$	$1.2-1.5$	0.044 ± 0.137
$1.2-1.5$	> 1.5	0.392 ± 0.269
> 1.5	$0.5-0.8$	0.047 ± 0.128
> 1.5	$0.8-1.0$	0.134 ± 0.177
> 1.5	$1.0-1.2$	-0.454 ± 0.217
> 1.5	$1.2-1.5$	-0.675 ± 0.270
> 1.5	> 1.5	-0.174 ± 0.424

Table 3.1: Tabular form of Fig. 3-2.

For a particular region of the $p_T^{h^+} - p_T^{h^-}$ phase space, there is a negative asymmetry (i.e. for $p_T^{h^-}$ >1.5 GeV/c and for $p_T^{h^+}$ >1.0 GeV/c). If it can be proven that in this region PGF is the dominant contribution to the cross section, then this immediately leads to the conclusion that $\Delta G/G$ is positive for these kinematics. It will be the subject of chapter 4 to discuss this in further detail. For now, a few systematic studies of the stability of the asymmetry are presented.

A study to search for a possible time dependence in the asymmetry was conducted by breaking the data set into four time periods containing roughly equal levels of statistics. These time periods were defined to be:

- the 1996 polarized data set,
- 1997 period 1: fills numbered 21 to 67,
- 1997 period 2: fills numbered 102 to 145,
- 1997 period 3: fills numbered 206 to 272,

where the numbering of the fills corresponds to the numbering used in the μDST production. The result for $A_{||}(p_T^{h^+}, p_T^{h^-})$ for each time period is displayed in each of the four panels in Fig. 3-3. All the plots use the same vertical and horizontal scales. Comparing each point with the next one in time shows that there is no time dependence to the asymmetry within the level of statistics. It is also evident that the negativity of the asymmetry for large $p_T^{h^-} > 1.5$ GeV/c persists for all four periods. The number of events in each bin for each year is displayed in Table 3.2.

Another consistency check is to test the influence of pion identification using the Čerenkov counter. This can in principle alter the sensitivity to $\Delta G/G$, but, within the level of statistics, is expected to lead to a consistent asymmetry. The asymmetry for $\pi^+\pi^-$ pairs is presented in Fig. 3-4. From this plot, it appears that the asymmetry for pions in the region of interest is even larger than that for all hadrons. This might be understood in terms of less contamination from protons from the target region at $x_F < 0$. Pions would therefore have higher sensitivity to the polarization of the gluons. Monte Carlo studies with PYTHIA have shown agreement with this expectation.

The normalized yield of events selected via the criteria described above was measured fill by fill and compared with the fluctuations in the DIS normalized yield. This

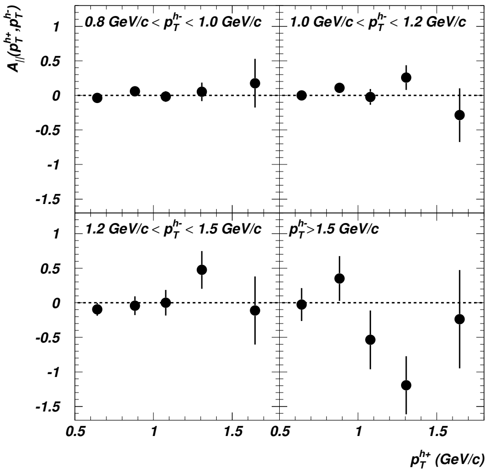

(a) 1996

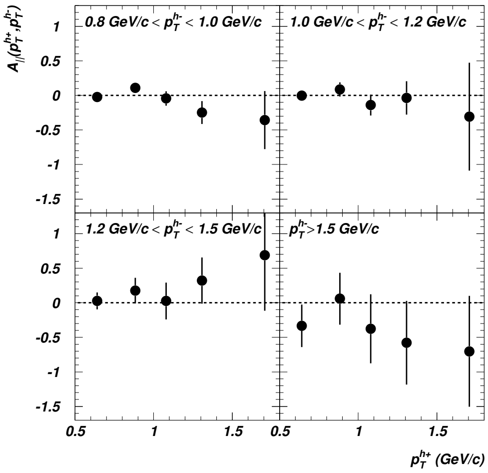

(b) 1997 period 1

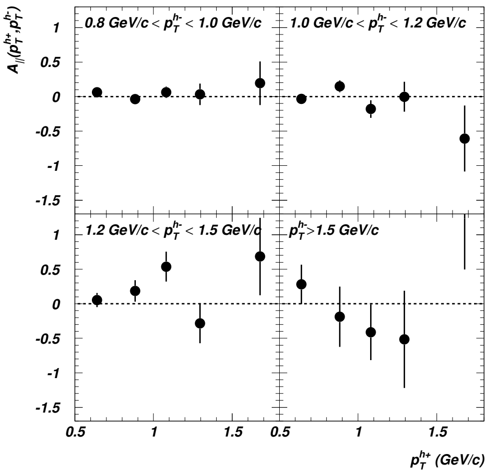

(c) 1997 period 2

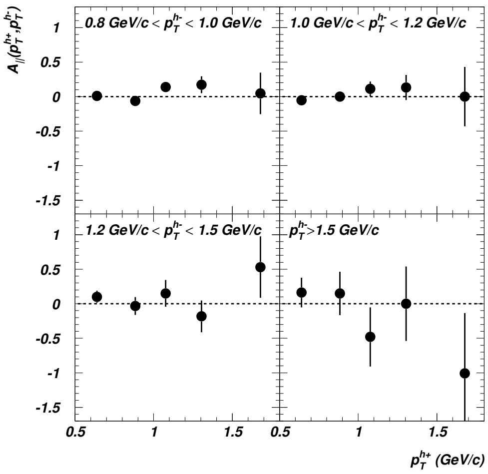

(d) 1997 period 3

Figure 3-3: $A_{||}(p_T^{h^+}, p_T^{h^-})$ for 1996, and periods 1, 2, and 3 from 1997.

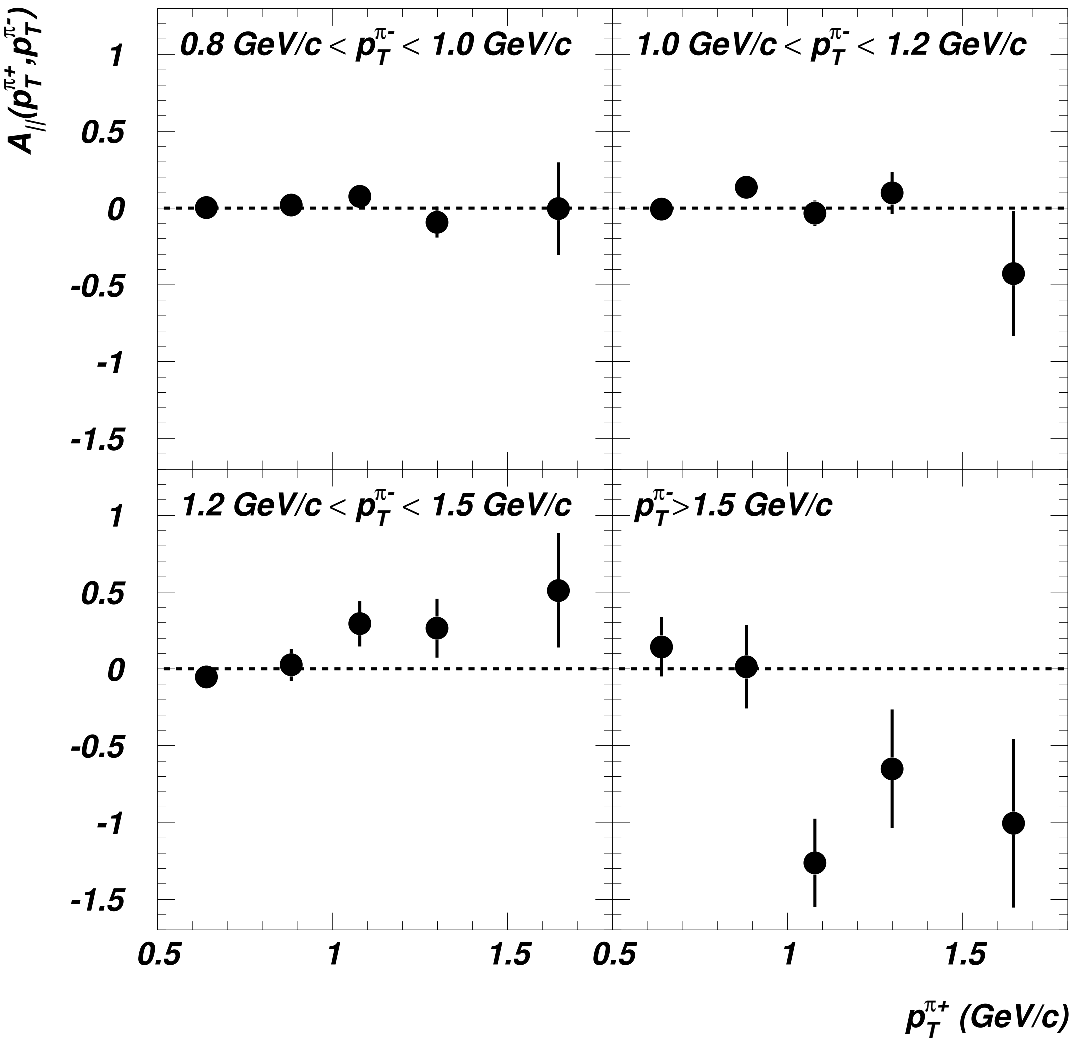

Figure 3-4: $A_{||}(p_T^{\pi^+}, p_T^{\pi^-})$ for HERMES 1996 and 1997 data combined.

$p_T^{h^+}$ range (GeV/c)	$p_T^{h^-}$ range (GeV/c)	1996 + target	1996 - target	1997 + target	1997 - target
> 1.5	$0.8 - 1.0$	17	20	56	55
> 1.5	$1.0 - 1.2$	17	13	20	26
> 1.5	$1.2 - 1.5$	10	9	24	13
> 1.5	> 1.5	5	4	7	8
$0.8 - 1.0$	> 1.5	18	25	48	46
$1.0 - 1.2$	> 1.5	15	9	25	38
$1.2 - 1.5$	> 1.5	14	4	14	19
subtotals		96	84	194	205
yearly totals		180		399	
total		579			

Table 3.2: Number of events in each bin for each year. Note that the beam polarization direction reverses between the two years, while the target polarization doesn't change definition. Only bins used for the extraction of $\Delta G/G$ in Chapter 4 are listed.

was done to see if the high-p_T yield was as well behaved (i.e. stable) as the DIS yield. Here, the "yield" was defined as the event rate normalized to the luminosity monitor rate:

$$Y = \frac{N^+ + N^-}{L^+ + L^-}. \tag{3.8}$$

The DIS positrons used for comparison were identified using the following cuts: pid3+pid5 > 2, $p > 3.5$ GeV/c, $0.02 < x < 0.85$, $y < 0.85$, $W^2 > 4$ GeV^2, $Q^2 > 1$ GeV^2, vertex cuts as for the high-p_T case, and $\theta > 40$ mrad. The result of the comparisons for 1996 and 1997 data is shown in Figure 3-5. The rate of high p_T photoproduction events is roughly a factor of 10 less than the DIS rate. Note that fluctuations in the high-p_T hadron yield are strongly correlated to fluctuations in the DIS yield. The jump in the middle of the 1996 year can be understood as the changing of the calorimeter row-sum threshhold in the DIS trigger, which was lowered from 3.5 to 1.4 GeV to attempt to cover a larger range of DIS kinematics (specifically enlarging the acceptance in the variable y). That the yield of high p_T events is higher in 1997 than 1996 is due to the fact that the efficiency of trigger 28 was improved substantially (by about 30%) in the 1997 data taking year. The trigger efficiencies will be discussed in greater detail in the next section.

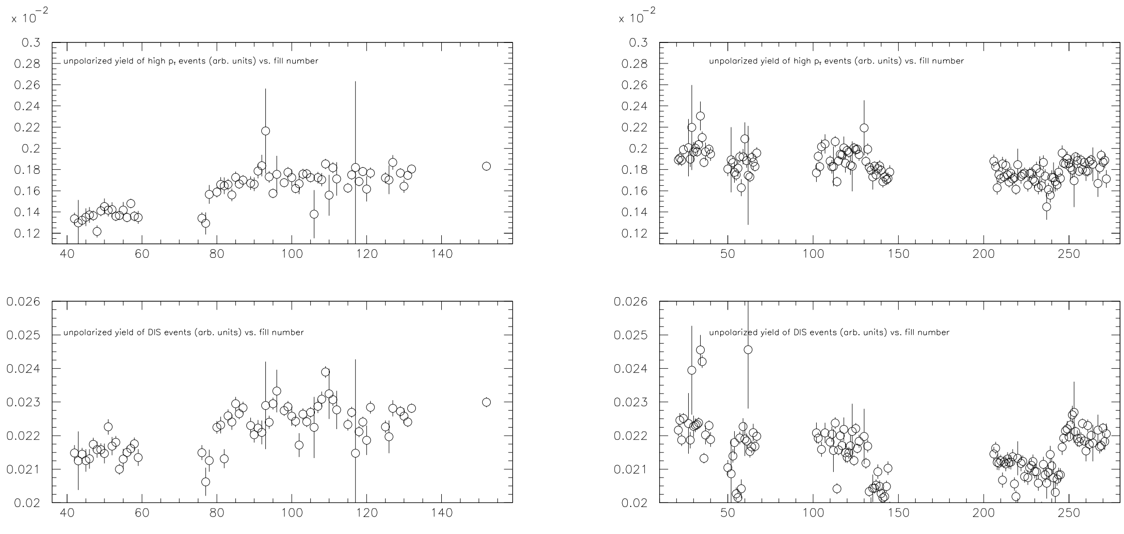

Figure 3-5: Normalized yields vs. fill number in 1996 (left) and 1997 (right). The top plot in each is the yield of high p_T events. The bottom plot is the yield of DIS events.

3.5.3 A Misidentification Background Study

A possible background to high-p_T hadron detection arises from coincident detection of a negative hadron and the scattered positron, the latter being misidentified as a positive hadron. The reason that this background is of special interest is due to the fact that it can produce a negative asymmetry. This negative asymmetry arises from polarized DIS from d quarks, tagged by the high-z negative hadron.

From studies comparing detector responses and from studies using the HERMES Monte Carlo and detector-specific Monte Carlos, the probability for positron/hadron misidentification has been determined to be less than but of the order 0.2%. Comparing e^+h^- pairs to h^+h^- pairs allows one to determine the relative flux. The number of events seen in the 1997 data for e^+h^- pairs and h^+h^- pairs is shown in Fig. 3-6. If the cross sections $\sigma(e^+h^-)$ are suppressed by the expected contamination factor of roughly 0.002, the e^+h^- contamination will be of the order 0.1%. Were this a mistaken underestimate of the actual contamination, the asymmetry of the background should be measured and corrected for. However, the asymmetry, binned in the usual p_T^+-p_T^- space was found to always lie within 5% of zero, as displayed in Fig. 3-7. The more negative asymmetry which has been observed in the h^+h^- case cannot be caused by e^+h^- contamination.

Another estimate of this contamination can be made by examining the distribution of events in the pid3+pid5 logarithmic likelihood variable. The distribution of events in pid3+pid5 for the positively charged particle for the selection $p_T^{h_1} > 1.5$ GeV/c and $p_T^{h_2} > 0.8$ GeV/c (in addition to the cuts defined in section 3.5.1) is displayed in Fig. 3-8. Positively charged hadrons appear in the peak on the left side of the plot while positrons appear in the peak to the right. In Fig. 3-8, two exponentials are fit for the region $-5 <$ pid3+pid5 < 5. One can also use Gaussian tails. This allows one to estimate the number of positrons in the tail underneath the hadron peak. Using these fits, one compares the integral

$$\int_{-\infty}^{-2} d(\mathrm{pid}) \frac{dN^+}{d\mathrm{pid}}(\mathrm{observed}) \tag{3.9}$$

to

$$\int_{-\infty}^{-2} d(\mathrm{pid}) \frac{dN^+}{d\mathrm{pid}}(e^+ \text{ valley fit}). \tag{3.10}$$

The result is 0.014% contamination for the Gaussian fit and 0.14% for the exponential fit. These compare favorably with the previously estimated value of 0.1%. The contamination of the negative hadron due to electrons is known to be comparatively very small, due to the lack of a significant source of electrons in deep-inelastic scattering

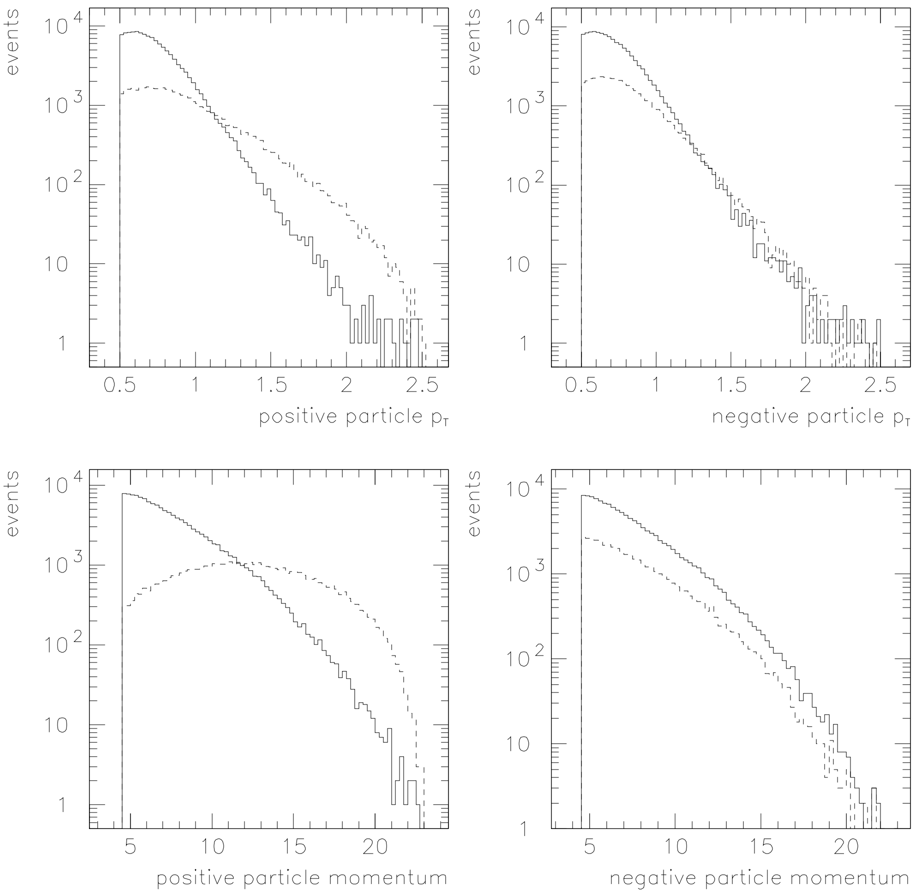

Figure 3-6: $N(p_T^{h^+}, p_T^{h^-})$ for h^+h- (solid) vs. e^+h^- (dashed). Suppressing $\sigma(e^+h^-)$ by factor of 0.002 (averaged PID flux independent contamination) brings e^+h^- contamination to the level 0.1%.

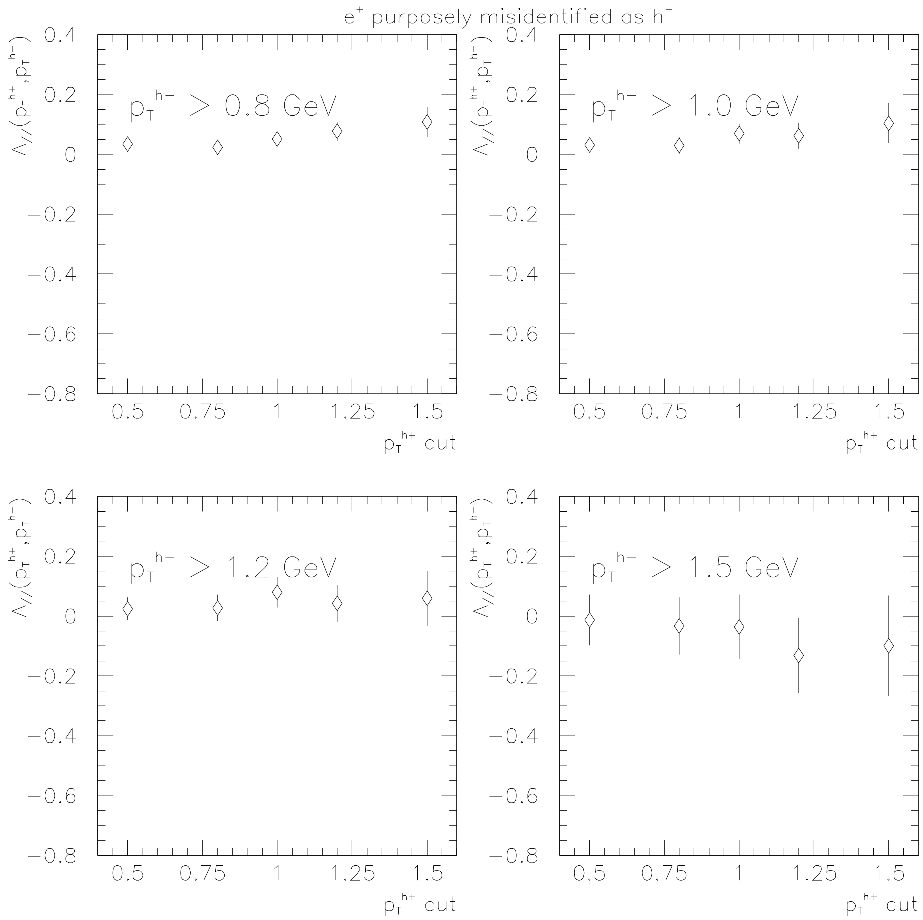

Figure 3-7: $A_{||}(p_T^{e^+}, p_T^{h^-})$ for e^+h- pairs. Even were this contamination significant, the asymmetry is close to zero.

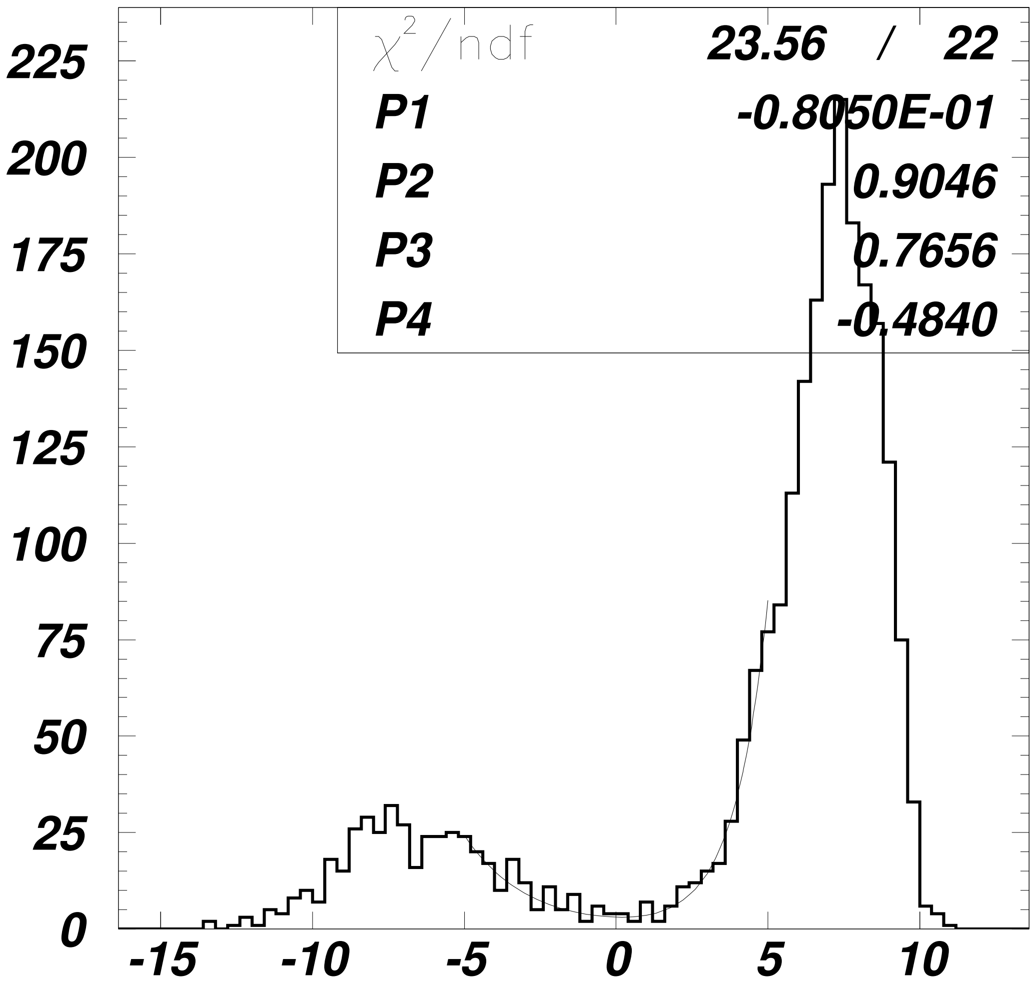

Figure 3-8: Number of events versus pid3+pid5 logarithmic likelihood variable for the positively charged particle in the event. Positive hadrons appear at negative pid3+pid5 and positrons at positive pid3+pid5. Two exponentials are fit to the data in the overlap region ($-5 <$ pid3+pid5 < 5) to estimate the positron tail. The cut in this variable is typically placed at pid3+pid5 $<$ -2 to isolate hadrons.

or photoproduction.

Another study regarding PID cut variation was carried out. The PID applied to the detected hadrons was changed from the likelihood method to the requirement that each of the four PID detectors separately cleanly identify hadrons. Both analyses yielded consistent results for the measured asymmetry. The minimum momentum required for each detected hadron was also varied, and found to have a negligible effect on $A_{||}$.

3.5.4 Cross Section Extraction

This section closely follows the measurement of the J/ψ cross section detailed in Refs. [94, 25].

In addition to the cuts specified in the previous section, only events where trigger 28 fired were used to identify the hadron pairs. The main difficulty in using trigger 21 for a cross-section measurement is that it has a kinematical dependence on e.g. the momentum of the hadron that triggers it. Also, since the prescale factor for trigger 28 was changed from time to time in 1996, only data from 1997 are used for the determination of the cross-section.

For the easy simulation of trigger 28 in Monte Carlo, an additional cut was applied to the data, that the two hadrons under consideration be observed in opposite detector hemispheres (as trigger 28 would ideally do). This cut has little additional impact, since, most of the time, the hadrons anyway appear in opposite detector halves.

Luminosity Determination

Two methods of determining the luminosity were checked against one another. DIS positron counting or the luminosity monitor rate can be used to determine the absolute luminosity.

Absolute Luminosity from DIS Positrons

The cuts used to define a DIS positron in section 3.5.2 were also used for this section to define a means to measure the luminosity accumulated for a given data set. Though the cuts used for this definition are slightly different than the ones used by F. Meiβner in Ref. [94], the difference in the rate should be negligible. This reference uses a cut of PID4 > 1.0, cuts on the slopes of the front track, and subtracts charge symmetric background from pair production by using electron events which pass DIS cuts.

The luminosity is determined from the number of DIS positrons detected:

$$L_{\mathrm{DIS}} = C_{\mathrm{DIS}} \frac{1}{\epsilon_{\mathrm{DAQ}}} N_{\mathrm{DIS}} \frac{\sigma_{^3\mathrm{He}}}{\sigma_{\mathrm{target}}}, \tag{3.11}$$

where the constant

$$C_{\mathrm{DIS}} = 21.8\ \mathrm{pb}^{-1}\ 10^{-6}\ \mathrm{DIS}^{-1} \tag{3.12}$$

was determined using a data-MC comparison of the DIS cross section for ^{3}He data collected in 1996. The other quantities necessary for a calculation of the luminosity are the DAQ live time ϵ_{DAQ} and the MC cross sections integrated over DIS kinematics for different targets. For ^{1}H and ^{3}He, these are $\sigma_{^1\mathrm{H}}$=60.9 nb and $\sigma_{^3\mathrm{He}}$=56.2 nb.

Therefore, for an atomic hydrogen target, the formula for the deadtime-corrected luminosity is:

$$\epsilon_{\mathrm{DAQ}} L_{\mathrm{DIS}} = 20.1 \mathrm{pb}^{-1}\ 10^{-6}\ \mathrm{DIS}^{-1} N_{\mathrm{DIS}}. \tag{3.13}$$

For the data selection applied to the 1997 data set, 1.47 $\times 10^6$ DIS events were found. This leads to a deadtime-corrected luminosity of $\epsilon_{\mathrm{DAQ}} L_{\mathrm{DIS}} = 29.5\ \mathrm{pb}^{-1}$.

Absolute Luminosity from the HERMES Luminosity Monitor

The luminosity monitor coincidence rate, with Monte Carlo input for the luminosity monitor efficiency and acceptance, can also be used to determine the absolute luminosity accumulated for a given data set:

$$L_{\text{lumi}} = C_{\text{lumi}} \sum_{\text{bursts}} (dL/dt) \cdot \Delta t. \tag{3.14}$$

The constant C_{lumi} was determined to be 0.448 μb^{-1}. The systematic error connected with this determination of the luminosity is about 6.5% [94, 81]. The deadtime-corrected luminosity can be calculated from quantities normally calculated for spin asymmetries:

$$\epsilon_{\text{DAQ}} L_{\text{lumi}} = C_{\text{lumi}} \sum_{\text{bursts}} (dL/dt) \cdot \epsilon \cdot \Delta t = C_{\text{lumi}}(L^+ + L^-). \tag{3.15}$$

For the data selection applied to the 1997 data set, $L^+ = 3.44 \times 10^7$ and $L^- = 3.43 \times 10^7$. Therefore, the deadtime corrected luminosity calculated by this method is $\epsilon_{\text{DAQ}} L_{\text{lumi}} = 30.7\ \text{pb}^{-1}$. This is in very good agreement with the value obtained using the DIS counting method.

Trigger Efficiency

The efficiency of trigger 28 was determined by comparing its rate to the those of triggers 18, 19, 20, and 21. The trigger logic of the relevant triggers is shown in table 3.3. In this table, a dot refers to the logical comparison "AND" and a "+" symbol refers to the logical comparison "OR". The subscripts "T" and "B" refer to the top and bottom halves of the detector. The abbreviations H0, H1, and H2 refer to pulses detected in the respective planes of hodoscopes. CA refers to the minimum energy row sum requirement in the calorimeter, and BC refers to the minimum multiplicity requirement in selected BC planes. These trigger requirements were described in

Trigger number	Logic
17	$(\mathrm{H0} \cdot \mathrm{H1} \cdot \mathrm{H2})_\mathrm{T}+(\mathrm{H0} \cdot \mathrm{H1} \cdot \mathrm{H2})_\mathrm{B}$
18	$(\mathrm{H1} \cdot \mathrm{H2} \cdot \mathrm{CA})_\mathrm{T}+(\mathrm{H1} \cdot \mathrm{H2} \cdot \mathrm{CA})_\mathrm{B}$
19	$(\mathrm{H0} \cdot \mathrm{H1} \cdot \mathrm{CA})_\mathrm{T}+(\mathrm{H0} \cdot \mathrm{H1} \cdot \mathrm{CA})_\mathrm{B}$
20	$(\mathrm{H0} \cdot \mathrm{H2} \cdot \mathrm{CA})_\mathrm{T}+(\mathrm{H0} \cdot \mathrm{H2} \cdot \mathrm{CA})_\mathrm{B}$
21	$(\mathrm{H0} \cdot \mathrm{H1} \cdot \mathrm{H2} \cdot \mathrm{CA})_\mathrm{T}+(\mathrm{H0} \cdot \mathrm{H1} \cdot \mathrm{H2} \cdot \mathrm{CA})_\mathrm{B}$
28	$(\mathrm{H0} \cdot \mathrm{H1} \cdot \mathrm{H2} \cdot \mathrm{BC})_\mathrm{T}\cdot(\mathrm{H0} \cdot \mathrm{H1} \cdot \mathrm{H2} \cdot \mathrm{BC})_\mathrm{B}$

Table 3.3: Trigger logic for HERMES triggers relevant to determination of the efficiency of trigger 28.

greater detail in section 2.5.

The trigger efficiencies of the hodoscopes are determined by comparing triggers 18 to 20 with trigger 21:

$$\epsilon(\mathrm{H0}) = \frac{T18 \cdot T21}{T18}, \quad \epsilon(\mathrm{H1}) = \frac{T20 \cdot T21}{T18}, \quad \epsilon(\mathrm{H2}) = \frac{T19 \cdot T21}{T18}. \tag{3.16}$$

Since these are top OR bottom triggers, the average efficiency of each of H0, H1, and H2 for hadrons was determined by considering events with containing a single hadron track (identified by pid3+pid5 < -2).

The trigger efficiency for the BC in trigger 28 would ideally be determined by comparing to trigger 17, since the only difference between the triggers 17 and 28 is the requirement of top AND bottom (as opposed to top OR bottom), and the BC requirement. Note also that trigger 28 has some additional requirements placed on the hodoscope H0, namely that it does not have a large multiplicity (H0<8).

However, trigger 17 was prescaled heavily due to its large rate, so trigger 21, with its own finite efficiency for hadron detection, must be used for comparison:

$$\epsilon(\mathrm{BC} \cdot \mathrm{H0} < 8) = \frac{T21 \cdot T28}{T21}. \tag{3.17}$$

The efficiency for each component of trigger 28 is displayed in Fig. 3-9. The

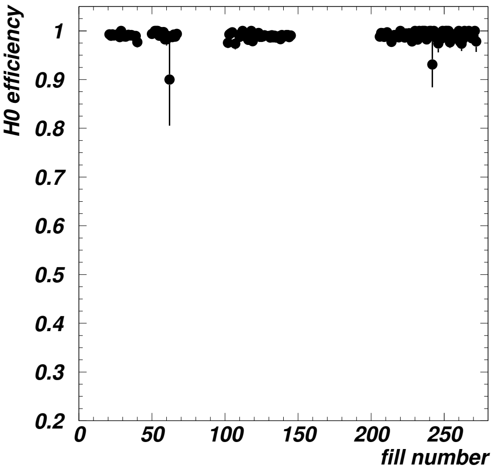

(a) ϵ(H0)

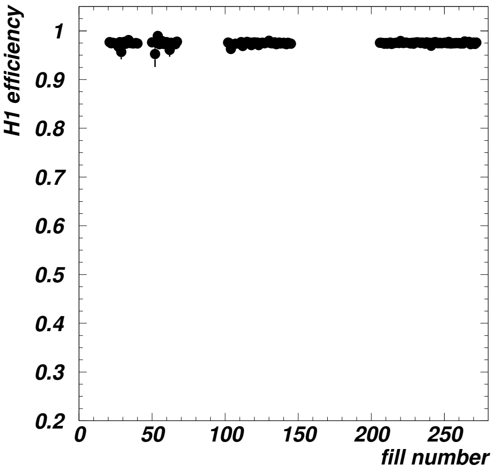

(b) ϵ(H1)

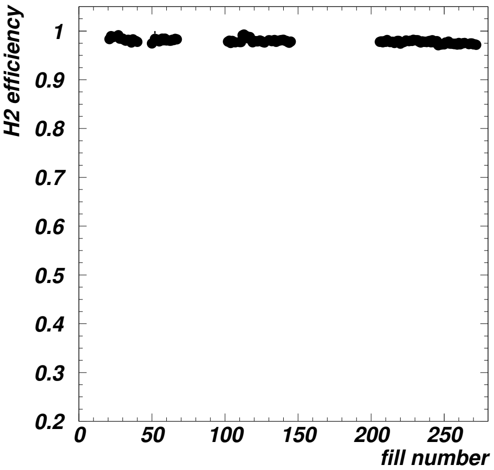

(c) ϵ(H2)

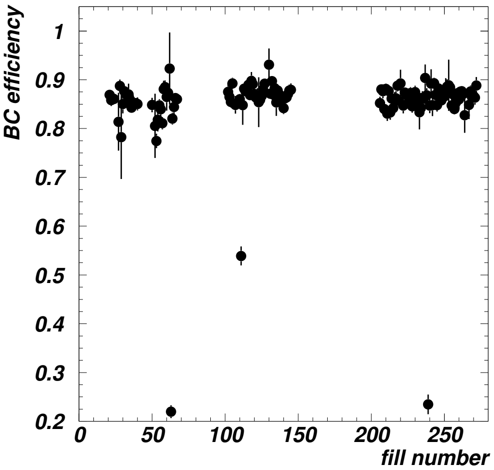

(d) $\epsilon(\mathrm{BC} \cdot \mathrm{H0} < 8)$

Figure 3-9: Efficiency for each piece of trigger 28 versus fill number.

average efficiency for each piece was: $\epsilon(\mathrm{H0}) = 0.991$, $\epsilon(\mathrm{H1}) = 0.975$, $\epsilon(\mathrm{H2}) = 0.980$, and $\epsilon(\mathrm{BC} \cdot \mathrm{H0} < 8) = 0.859$. Remember that the efficiencies for H0, H1, and H2 are for single hadrons, where the efficiency for the BC is for hadron pairs. Therefore, the efficiency of trigger 28 for hadron pairs was calculated from the partial efficiencies using the formula:

$$\epsilon(\mathrm{T28}) = \epsilon(\mathrm{H0})^2 \cdot \epsilon(\mathrm{H1})^2 \cdot \epsilon(\mathrm{H2})^2 \cdot \epsilon(\mathrm{BC} \cdot \mathrm{H0} < 8), \tag{3.18}$$

and had an average value of 0.759. A plot of the time dependence of $\epsilon(\mathrm{T28})$ is shown in Fig. 3-10. The uncertainty calculation for this quantity is complicated by the correlation between the errors on the efficiencies of the separate detectors, but is dominated by the statistical error of the determination of $\epsilon(\mathrm{BC} \cdot \mathrm{H0} < 8)$ which is roughly 1%. Aside from a few outlying points, the trigger efficiency is stable for the entire data set.

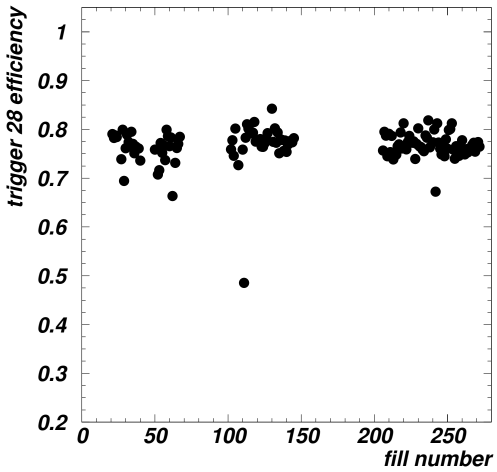

Figure 3-10: Efficiency of trigger 28 for hadron pairs as a function of fill number.

Acceptance and Tracking Efficiency

Tracking efficiencies were determined in Ref. [94] using the HERMES Monte Carlo program HMC. In this reference, the tracking efficiency within the HERMES acceptance for pions was found to be typically 98-99% for realistic detector efficiencies. Since two particles are required, the efficiency for this topology will therefore be roughly 96-98%. In independent studies with an older version of HMC, tracking efficiencies of the order 95% have been observed for single particles, giving two-particle efficiencies of order 90%. For simplicity, a typical two-track tracking efficiency $\epsilon(tracking)$ of 95% has been used, independent of the kinematics. A 5% systematic uncertainty will be assigned due to variation of this efficiency determined using the HERMES Monte Carlo.

Acceptance corrections were not performed on the data. Instead a simplified model of the HERMES acceptance was implemented in the Monte Carlo generator and used to predict the number of events expected to be seen by the experiment. The Monte Carlo will be described in further detail in Chapter 4. For now, the HERMES acceptance function is described and cross-sections measured with the HERMES acceptance folded in are displayed.

The acceptance function is dominated by angular cuts given by the acceptance of the front region of the HERMES spectrometer. The angular distribution of the events accepted by the analysis is shown in Fig. 3-11. The angular cuts that will be used to model the HERMES acceptance are:

- 40 mrad $< |\theta_y| <$ 140 mrad,
- $|\theta_x| <$ 170 mrad,

for all charged particles. Here θ_x is the angle of the front track measured with respect to the y plane and vice versa for θ_y. The locus of points selected by these cuts is superimposed over the data in Fig. 3-11. The upper and lower detector halves are seen quite clearly. The angular cuts match the edges of the acceptance quite well.

However, roughly 20% of the events selected by the current analysis fall outside the

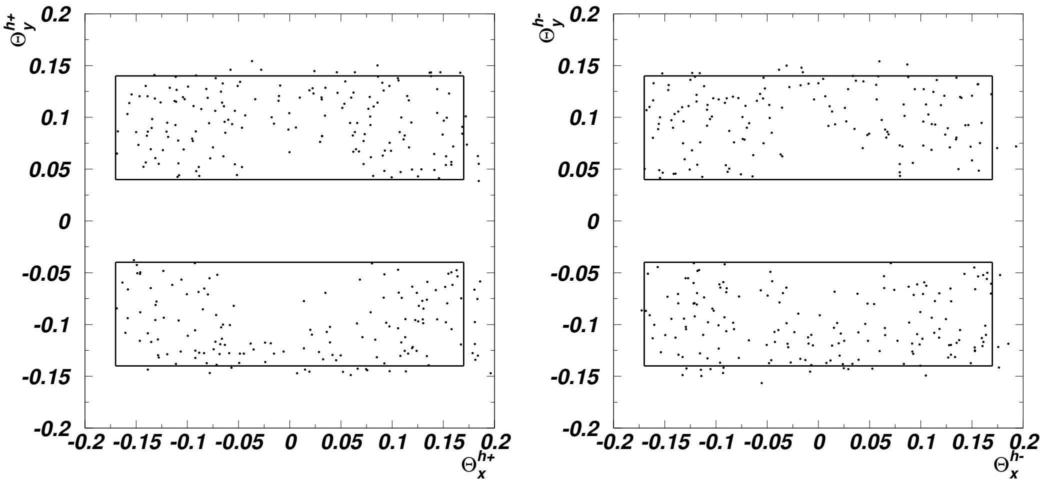

(a) (b)

Figure 3-11: θ_x vs. θ_y for (a) positive hadrons, (b) negative hadrons. Detector acceptance in the front region used in Monte Carlo is superimposed. Events were selected by the cuts $p_T^{h_1} > 1.5$ GeV/c and $p_T^{h_2} > 0.8$ GeV/c, in addition to the cuts defined in sections 3.5.1 and 3.5.4.

angular cuts. To reduce the systematic error associated with using the simplistic acceptance model, it was decided to apply the front region acceptance cuts to the data. (Note that this was only done for cross section comparisons, because in the asymmetry measurement, the acceptance effects tend to cancel.) Implementing these cuts improves the agreement between the real acceptance and the simple model.

Particles with low momenta (defined by $p \lesssim 2$ GeV/c) can be bent out of the HERMES acceptance in the back region (after passing through the magnet). This effect can be modelled by using a look-up table (used in the HERMES Monte Carlo, and similar to the look-up table used for fast momentum reconstruction in HRC) that determines the bend in the magnetic field for a given particle type [95]. However, for charged particles with momenta greater than 4.5 GeV/c (as selected by the present analysis), this effect is negligible.

The effect of momentum smearing (mentioned to be of the order of 1% in section 2.3.1) can also be neglected. The smearing in p_T was also found to be of the order 1% from independent Monte Carlo studies (though this could be deduced from the independent momentum and angular resolutions of section 2.3.1). The p_T resolution is shown in Fig. 3-12 for single pion events generated isotropically in θ_x and θ_y across the HERMES acceptance, and for pion momenta in the range 4.5-20 GeV/c. The RMS (standard deviation) and Sigma (from Gaussian fit) agree well. Therefore, the average p_T-resolution determined in this Monte Carlo model is 0.9%. This study

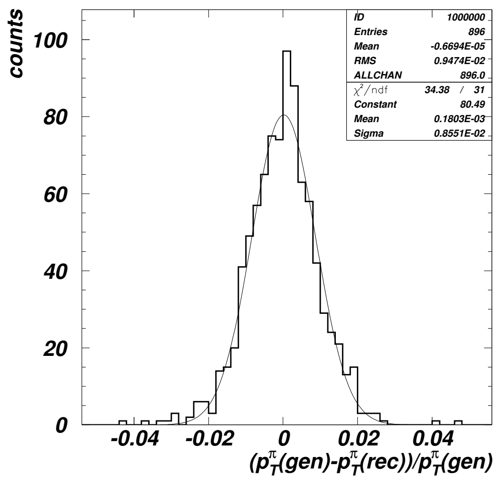

Figure 3-12: $(p_T^\pi(\text{gen}) - p_T^\pi(\text{rec}))/p_T^\pi(\text{gen})$ determined in HERMES Monte Carlo. The p_T resolution for pions is of the order 0.9% in this model.

was carried out using the HERMES Monte Carlo with a detector arrangement similar to that used in the 1997 data taking period.

The finite resolution with which p_T can be determined can therefore be safely neglected in the Monte Carlo studies, and the complicated acceptance can be simplified to a "box acceptance" where only angular cuts in the lab frame are placed on the charged particles produced.

The Cross Section

Aside from the acceptance correction, the cross section for the production of high-p_T can be deduced from the number of counts observed in the HERMES spectrometer:

$$\sigma A = \frac{N}{\epsilon(\mathrm{T28}) \cdot \epsilon(\mathrm{tracking}) \cdot \epsilon(\mathrm{DAQ}) L(\mathrm{lumi})}. \tag{3.19}$$

Here, σA signifies the that cross section still has the HERMES acceptance folded into it.

The measured number of events per unit p_T for each of the cases of a leading positive hadron or negative hadron is shown in Fig. 3-13, and given in tabular form in Table 3.4.

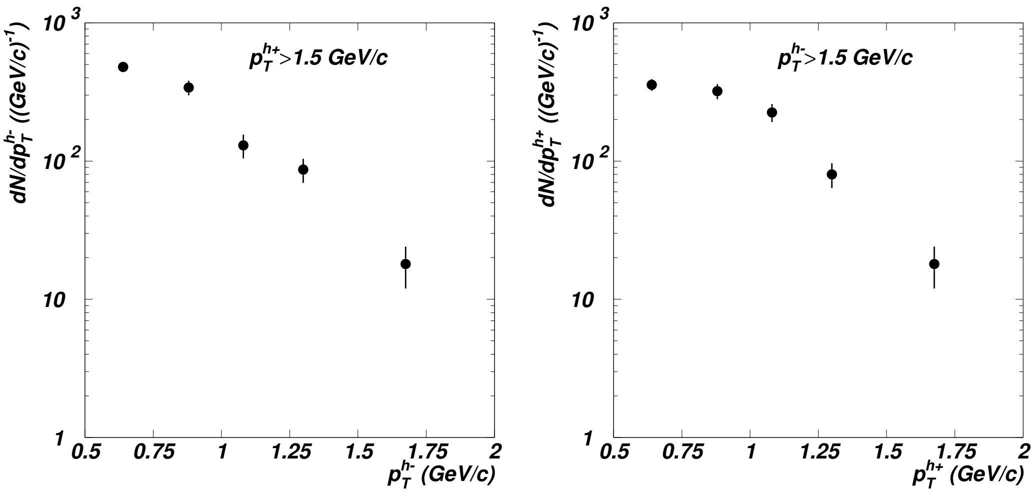

(a) (b)

Figure 3-13: Number of events seen in the HERMES spectrometer for the cases (a) $p_T^{h^+} > 1.5$ GeV/c and (b) $p_T^{h^-} > 1.5$ GeV/c.

Dividing each point in Fig 3-13 by the factor $\epsilon(\mathrm{T28}) \cdot \epsilon(\mathrm{tracking}) \cdot \epsilon(\mathrm{DAQ}) \cdot L(\mathrm{lumi})$ gives the acceptance weighted cross section. The acceptance weighted cross section

$p_T^{h^+}$ range (GeV/c)	$p_T^{h^-}$ range (GeV/c)	number of counts N
> 1.5	$0.5 - 0.8$	144
> 1.5	$0.8 - 1.0$	68
> 1.5	$1.0 - 1.2$	26
> 1.5	$1.2 - 1.5$	26
> 1.5	> 1.5	9
$0.5 - 0.8$	> 1.5	107
$0.8 - 1.0$	> 1.5	64
$1.0 - 1.2$	> 1.5	45
$1.2 - 1.5$	> 1.5	24

Table 3.4: Number of events in each bin shown in Fig. 3-13.

is shown in Fig. 3-14.

Systematic Errors in the Measurement of the Cross Section

The dominant systematic errors associated with the measurement of the cross section are catalogued in Table 3.5. The value for the luminosity monitor uncertainty (6%)

Error	Value
Determination of luminosity using luminosity monitor	6%
Normalized yield fluctuations	1.6%
Tracking efficiency	5%
Total	8%

Table 3.5: Dominant systematic errors associated with the measurement of the cross section.

is taken from Ref. [81]. This uncertainty is mainly due to the lack of knowledge of the exact beam position with respect to the luminosity monitor, and the fact that the cross section for the production of Bhabha pairs drops steeply with angle.

The value of the instrumental uncertainty due to normalized yield fluctuations

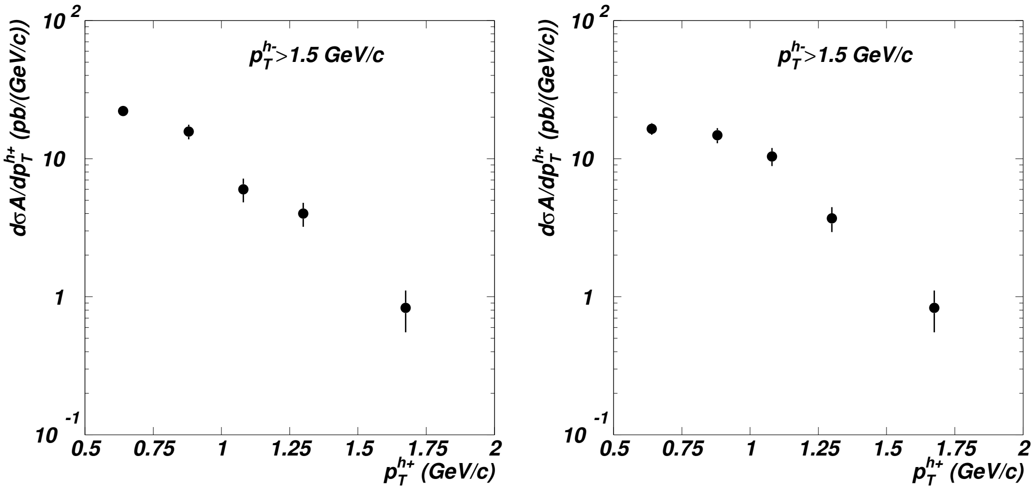

(a) (b)

Figure 3-14: Non-acceptance corrected cross section for the cases (a) $p_T^{h^+} > 1.5$ GeV/c and (b) $p_T^{h^-} > 1.5$ GeV/c.

was determined using the formula:

$$\sigma_Y^{\text{inst.syst.}} = \sqrt{\frac{\sum_{i=1}^{N_{\text{fills}}} \frac{(Y_i - \bar{Y})^2}{\sigma_i^2}}{(N_{\text{fills}} - 1) \sum_{i=1}^{N_{\text{fills}}} \frac{1}{\sigma_i^2}}} = \sqrt{\frac{\chi^2}{\text{d.o.f}}}\sigma_Y^{\text{stat.}}. \tag{3.20}$$

Here, $\bar{Y}$ and $\sigma_Y^{\text{stat.}}$ were determined using the formula for a weighted mean and error, respectively. The event selection for the yield was the same as the base-line cuts used for the cross section determination.

The yield fluctuation uncertainty and the luminosity monitor acceptance uncertainties may be correlated. It is suspected that the yield fluctuations seen when comparing different fills are due to differing beam conditions from fill to fill. The luminosity monitor is highly susceptible to slight differences in beam positions and slopes at the HERMES interaction point. However, searching for a correlation between beam parameters measured by beam position monitors in the HERMES region of the HERA ring and the luminosity monitor rate has proven fruitless [96]. It is likely that the resolution of the beam position monitors is insufficient to measure the beam position accurately enough to measure a correlation. Were there such a correlation, it would be maximal and including both would be redundant. Due the fact there is no knowledge of whether they are correlated, the pessimistic estimate that they are uncorrelated is taken, and they are added in quadature.

The value for the tracking efficiency uncertainty is taken from a comparison of different versions of Monte Carlo and reconstruction codes, as described earlier.

Adding the uncertainties in quadrature gives a relative systematic uncertainty of roughly 8% for the measurement of the cross section.

Chapter 4

Interpretation

In this chapter, the interpretation of the measurement of a negative asymmetry in this particular region of the high-p_T phase space is discussed. Most of this interpretation will be from within the framework of the Monte Carlo program PYTHIA [97]. Several results are relatively independent of the use of this code, however. For example, the fact that ΔG is positive in the particular x_G-range probed by the experiment, providing that the PGF process dominates in this region of phase space, is a statement that is independent of the Monte Carlo used.

4.1 Brief description of PYTHIA

PYTHIA is a Fortran code used to model high energy physics processes. Aspects of its photoproduction generator were used to model the photoproduction data accumulated at HERMES.

The PYTHIA Monte Carlo program is described in detail in a relatively out-of-date manual [97] which describes early versions of PYTHIA (version 5.7) and JETSET (version 7.4). JETSET is a portable piece of the code that is used to describe the fragmentation process using the string model. More recent versions of the code exist and in fact PYTHIA and JETSET have been combined into a single code "PYTHIA" whose current version is 6.129. Due to lack of documentation of this code, an older, relatively well documented version of the code was used. The Monte Carlo results for this paper were obtained using PYTHIA version 5.724 and JETSET version 7.410. This turns out to be an important consideration, as PYTHIA has evolved considerably since the writing of the manual in late 1993. For example, the photoproduction section of the code (at least in version 5.724) appears to have been tuned to e^+e^- collider experiments, despite the fact that it was once used to describe photoproduction [26, 27] and $\mathrm{e^+e^-}$ [98] processes down to typical HERMES energies $\sqrt{s} \simeq 7$ GeV.

4.1.1 Important PYTHIA and JETSET parameters

The parameters that were found to be important for studying photoproduction at HERMES are listed in Table 4.1. The values listed in the "Value" column of Table 4.1

PYTHIA Parameter	Value	Function
`CKIN(1-6)`	see text	phase space limits at partonic level
`MSEL`	2	automatically select processes to generate
`MSTP(14)`	10	use full model of photon (see section 1.2.4)
`MSTP(15)`	1	use same $\hat{p}_T^{\mathrm{min}}$ for anomalous as for hard VMD
`MSTP(51)`	5005	proton parton distribution functions (GRV94LO [99])
`MSTP(52)`	2	use PDFLIB [100] parton distributions
`MSTP(55)`	1	photon parton distribution functions
`MSTP(171)`	1	variable energies from one event to the next
`MSTP(172)`	2	for variable energies, try only one event configuration
`PARP(2)`	2.0 GeV	lower limit for total CM energy
`PARP(15)`	0.5 GeV/c	p_0 cut-off of Ref. [27]
`PARP(91)`	0.44 GeV/c	intrinsic k_T of initial state partons in hadron
JETSET Parameter	**Value**	**Function**
`PARJ(21)`	0.34 GeV	p_T width for primary hadrons
`PARJ(41)`	0.82 GeV^{-2}	a parameter in Lund fragmentation function
`PARJ(42)`	0.24 GeV^{-2}	b parameter in Lund fragmentation function

Table 4.1: PYTHIA and JETSET parameters relevant to photoproduction at HERMES and their values for the analysis presented in Ref. [101].

are those used to attain the results presented in the HERMES publication related to this analysis [101]. These parameters will also be used for sections 4.2 through 4.7. Possible variations of the parameters will be considered in section 4.8.

The values of the `CKIN` parameters are set automatically when running in the mode where `MSTP(14)=10`, as they mainly determine the efficiency of the generation. Note that this also automatically implies that `MSTP(57)` (parton distribution softening at low x and $\hat{p}_T^2$) is set to `1` (on).

Any perturbative QCD calculation requires a low energy cut-off to avoid infrared divergences. This is especially important for calculations in leading order. In the case of calculating the cross section for the production of two hadrons with high p_T, the relevant cut-off parameter is the minimum transverse momentum of the outgoing partons, $\hat{p}_T^{\min}$. In terms of the Mandelstam invariants for the subprocess $\hat{s}$, $\hat{t}$, and $\hat{u}$, and Q^2, the expression for $\hat{p}_T$ is:

$$\hat{p}_T^2 = \frac{\hat{s}\hat{t}\hat{u}}{(\hat{s}+Q^2)^2} \tag{4.1}$$

In the analysis presented here, this parameter has been chosen following Ref. [27], i.e., $\hat{p}_T^{\min} = 0.5$ GeV/c for the direct processes. In the PYTHIA code, this is altered by choosing `PARP(15)`, or by placing a cut on the generated $\hat{p}_T$ in the final analysis. The choice of $\hat{p}_T^{\min} = 0.5$ GeV/c is motivated by several arguments:

(a) When fixing the couplings for VMD and using the cut-off for the direct processes as a free parameter, both the total γp cross section (from previous experiments) and the cross section for two hadron production (from this analysis) are well described by a cut-off of 0.5 GeV/c.

(b) Direct processes should become important above the threshold for production of the heaviest vector meson used in the VMD model, i.e. $\hat{p}_T c > \frac{1}{2} m_\phi c^2 \simeq 0.5$ GeV.

(c) The QCD evolution of measured photon structure functions is consistent with the assumption that these structure functions are zero at scale 0.5 GeV.

It is argued in Ref. [27] that, at fixed target energies, effects from anomalous photon processes should be small. For this reason, all hard photon structure processes were switched off, allowing only softer processes to contribute. The selection was conducted by placing a cut on the number identifying the generated subprocess for each event, given by `MINT(1)` in PYTHIA. The cut placed was that `MINT(1)` be either `33` (QCDC), `54` (PGF), or greater than `89` (diffractive processes and multiple interaction phenomenology). The effect of attempting to include hard VMD and anomalous photon interactions was studied and will be discussed in greater detail in section 4.8.2.

PYTHIA makes use of the Lund string model implemented in the JETSET section of the code. Due to the use of the Lund model, PYTHIA cannot give a reliable description of low multiplicity events that are created from a hard subprocess. The cross section for such events has been shown to be related to the non-forward gluon distribution [102], and, for the kinematics selected by the present analysis, the contribution from such processes is expected to be negligible [103]. Within the limited statistics due to the small acceptance of the HERMES spectrometer, the result was found to be unchanged when requiring a higher observed charged hadron multiplicity [104]. Studies with PYTHIA in 4π have shown that the average multiplicity of charged hadrons in the forward hemisphere ($x_F > 0$) is typically 5.5, justifying JETSET simulation of the fragmentation.

4.2 Implementation of PYTHIA in genX

The PYTHIA Monte Carlo was implemented for the HERMES geometry and kinematics in a Fortran code called genX [105]. It was not necessary to use the full HERMES Monte Carlo HMC because of the simplicity of the HERMES acceptance, and the desire to generate many events quickly using different Monte Carlo settings. The main features of genX (in its interface to PYTHIA) are:

- Interface to the Histogram and Test Package [86]. Since this same output package is used by dk (the code used to analyze the data), this facilitates parallel analysis of the Monte Carlo output.

- Simple model of the HERMES acceptance.

- Expansion of PYTHIA photoproduction cross sections to leptoproduction at varying ν and Q^2 using the Weizsäcker-Williams approximation [11, 106], similar to that used in HMC. Rotation of each event so that the incident positron momentum was along the beam axis (defined to be the z-axis).

The expression for the Weizsäcker-Williams approximation used for the conversion of photoproduction cross sections to leptoproduction cross sections was [2]:

$$\frac{d^2\sigma^{eN\to X}}{dQ^2 d\nu} = \frac{\alpha_e}{2\pi}\frac{2(1-y)+y^2+Q^2/2E^2}{Q^2(Q^2+\nu^2)^{1/2}}\sigma^{\gamma N\to X}(\nu), \tag{4.2}$$

which is valid for low Q^2. Here, E is the electron beam energy. The arbitrary final state X indicates that the two cross sections $\sigma^{eN\to X}$ and $\sigma^{\gamma N\to X}$ can in principle be differentiated with respect to variables related to the hadronic final state, for example $\vec{p}^{h^+}$ and $\vec{p}^{h^-}$, the momenta of two produced hadrons. The bounds of integration in the variable Q^2 for a given ν are given by the expressions:

$$\begin{aligned} Q^2_{\text{min}} &= \tfrac{m_e^2\nu^2}{E(E-\nu)}, \\ Q^2_{\text{max}} &= 2m_p\nu, \end{aligned} \tag{4.3}$$

where the minimum possible Q^2_{min} is set by the scale of the electron mass and the maximum possible Q^2_{max} is set by the elastic scattering limit.

4.3 Comparison of the MC Cross Section to Data

Using the cuts specified in section 3.5.4, and the version of the Monte Carlo described above, the cross section generated by the PYTHIA Monte Carlo was compared to the two hadron cross section measured by HERMES. In particular, the number of events expected to be seen in the HERMES spectrometer in the high-p_T region of interest (as in Fig. 3-13) is compared in Fig. 4-1. Both cases are compared with MC predictions

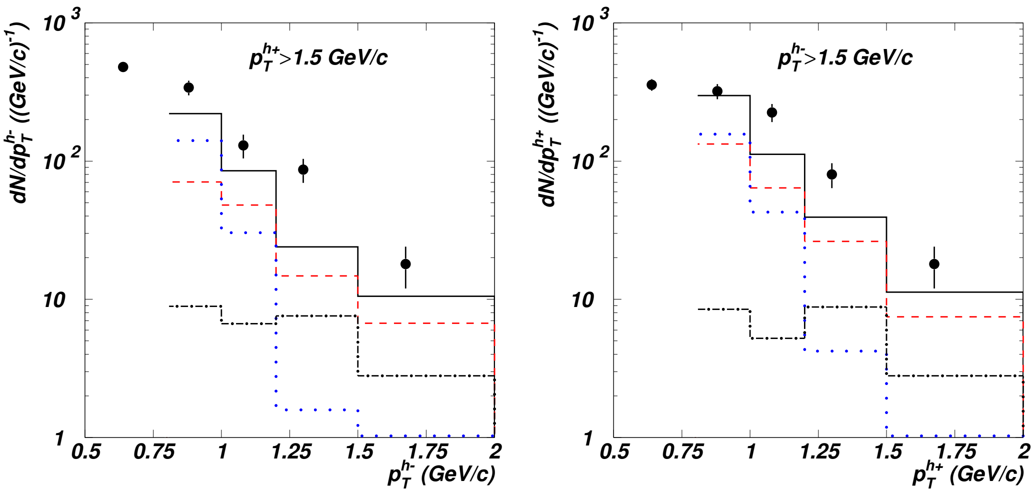

(a) (b)

Figure 4-1: Number of events seen in the HERMES spectrometer for the cases (a) $p_T^{h^+} > 1.5$ GeV/c and (b) $p_T^{h^-} > 1.5$ GeV/c, compared with MC predictions for 22 pb^{-1} of integrated luminosity. The systematic error is roughly 8% (not shown). The various curves are the total (solid) and the contributions from PGF (dashed), QCDC (dotted), and soft VMD (dot-dashed).

for roughly 22 pb^{-1} of integrated luminosity. This efficiency corrected luminosity was determined in section 3.5.4). The systematic error in the comparison is roughly 8%, dominated by the luminosity determination uncertainty. The contributions from each subprocess type (PGF, QCDC, and soft VMD) are also plotted along with the sum total.

From Fig. 4-1, it can be seen that the two hadron photoproduction cross section is underestimated by the Monte Carlo, by roughly a factor of two. Several possible explanations exist and will be addressed:

- Inability to use PYTHIA at HERMES energies.
- Neglect of possible contributions to the cross section. For example, hard VMD and anomalous photon structure have been neglected in this analysis.
- Higher order corrections, such as next-to-leading order (NLO) effects, could increase the cross section.
- It could be incorrect to use the HERMES fragmentation parameters which have been tuned to semi-inclusive data at considerably lower W^2.

Each of these possibilities is coupled to the next and the last three are symptomatic of studying cross sections at high-p_T. The possibilities are discussed in section 4.8. For now, a few additional estimates of possible contributing cross sections are discussed. Then, a result for $\Delta G/G$ is extracted in the "best" model of the data, using the measured asymmetries. No effort is made to further tune the Monte Carlo.

4.4 Checking the direct processes in PYTHIA using PEPSI

The contamination from virtual photoabsorption (here, denoted as "DIS") was estimated using the PEPSI Monte Carlo generator [107] with genX. In Fig. 4-2, the sum of QCDC and PGF parts of the two hadron cross sections from PYTHIA and PEPSI are compared in an overlap region of Q^2. The cross sections are integrated over the HERMES acceptance (σA). The cross sections have not been renormalized to one another. Even on an absolute scale, the cross sections agree well with one another.

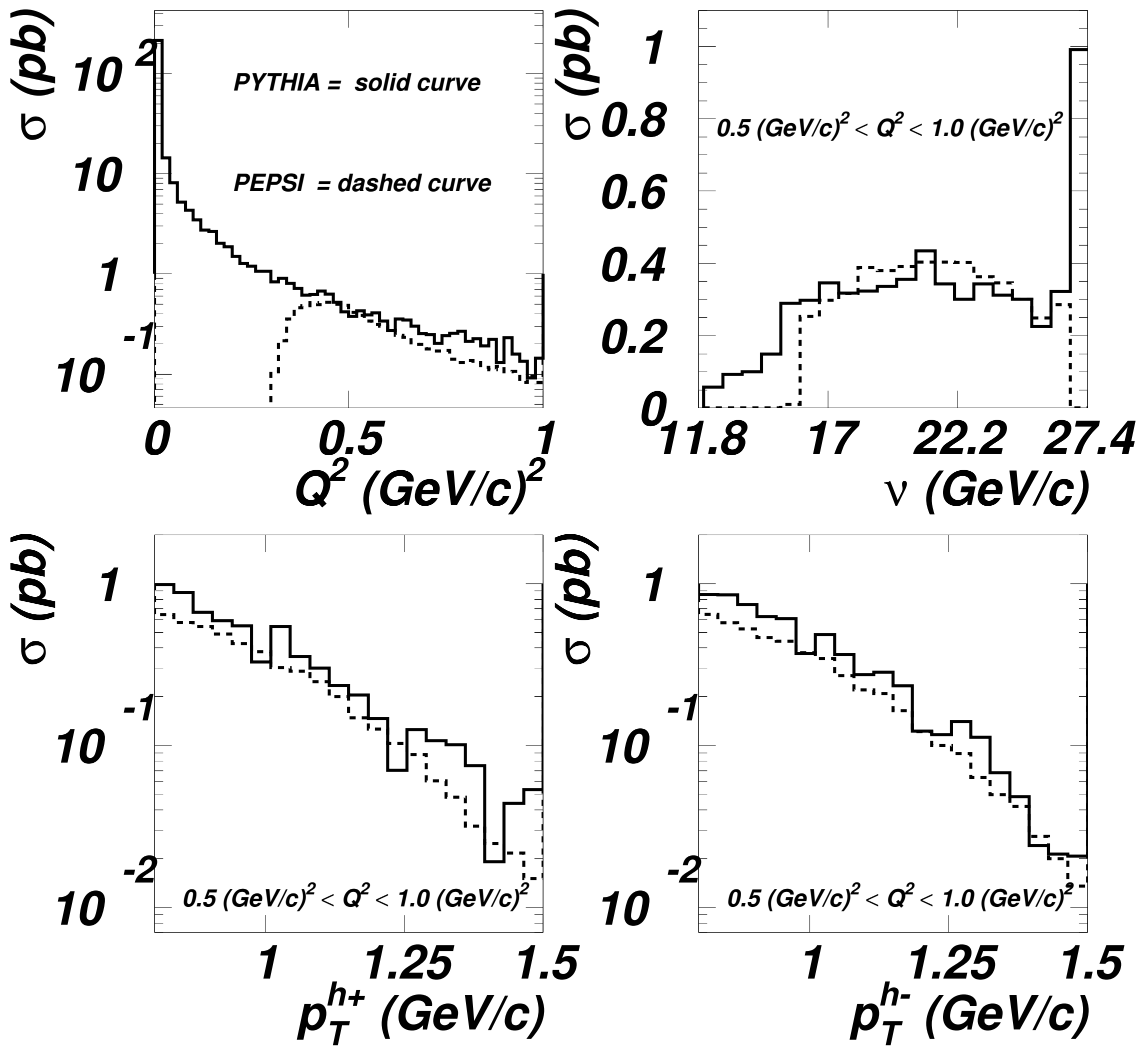

Figure 4-2: Absolute cross sections compared between PYTHIA and PEPSI in overlap region of Q^2 defined by 0.5 $(\mathrm{GeV/c})^2 < Q^2 < 1.0$ $(\mathrm{GeV/c})^2$.

The PYTHIA cross sections are higher by roughly 30%. The shapes of the distributions also agree quite well. Both these facts lend support to the belief that PYTHIA is doing a reasonable job of describing cross sections for these kinematics. The peak at high ν in PYTHIA is bothersome, but only seems to arise when such restrictive Q^2 cuts are applied. It is likely due to insufficient modeling of the acceptance for low momentum positrons.

Counting the number of virtual photoabsorption events seen in PEPSI (starting at the threshold of about $Q^2 = 0.3$ (GeV/c)^2, and comparing to the direct and soft VMD events in PYTHIA will therefore lead to an estimation of the contamination due to DIS. The following contaminations were determined: σ(DIS)/σ(direct)=2.1% and σ(DIS)/σ(direct + soft VMD)=1.4%. The uncertainties in the contaminations are of order the normalization difference of the PYTHIA and PEPSI Monte Carlos, i.e. roughly 30% relative uncertainty. The comparison was performed for the following cuts: no positron observed in acceptance, $M(2\pi) > 1.0$ GeV/c^2, $p_T^{h\pm} > 0.8$ GeV/c. The “no positron” requirement, which was included to attempt to suppress the DIS background, does not affect the cross section strongly and has little effect on the DIS contamination.

4.5 Contributions from charm production

It is important to study the rate of production of heavy quarks in photon gluon fusion because the subprocess asymmetry for heavy quark photon gluon fusion is positive [1], in contrast to the value -1 for light quark photon gluon fusion. The reason for this is that the larger mass of the produced charm quarks introduces another energy scale into the problem.

Contributions from charm production were modeled using the AROMA Monte Carlo generator [108]. The computation was performed [104] using a method similar to the one used in the preceding section. The ratio of heavy quark photon gluon fusion production to light quark photon gluon fusion is shown for each of the cases of a leading, high-p_T positive or negative hadron in Fig. 4-3. The contamination was

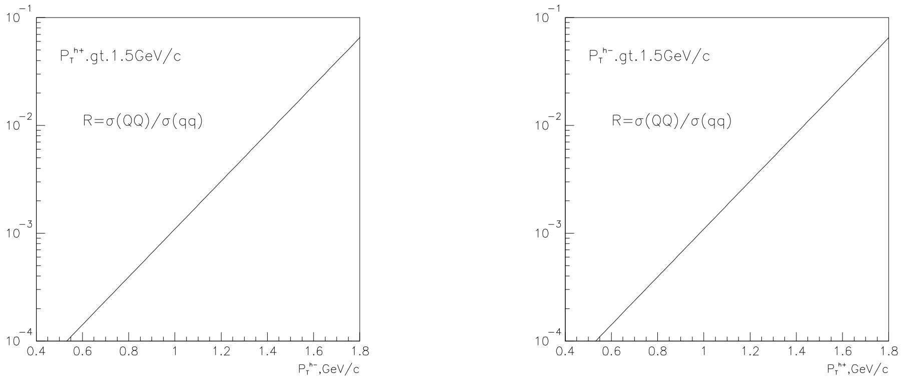

(a) (b)

Figure 4-3: Ratio of cross sections for heavy quark photon gluon fusion to light quark photon gluon fusion for (a) $p_T^{h^+} > 1.5$ GeV/c, (b) $p_T^{h^-} > 1.5$ GeV/c .

found to be always less than 5% of the light quark photon gluon fusion rate, reaching 5% only in the highest p_T bin, where statistics are negligible. The contribution to the cross section integrated over the region of interest is less than one percent.

It is also important to study the contribution from diffractive charm quark production via the J/ψ resonance. This is modeled to an extent in PYTHIA itself. Though the asymmetry for elastic J/ψ production is expected to be negligible [21, 22], it is necessary to know how much of a dilution it presents to the asymmetry.

The decay J/$\psi \rightarrow \mu^+\mu^-$ decay presents a background because the two muons produced in the decay have a similar kinematical signature to two high-p_T hadrons. Also, for the HERMES spectrometer setup in 1996 and 1997, there was no explicit muon identification. In the HERMES PID scheme, the muon therefore looks like a slightly lighter pion, which can't be easily separated from hadrons. The only difference is that the muons shower slightly more in the electromagnetic calorimeter and preshower particle identification detectors [94].

The J/$\psi \to \mu^+\mu^-$ contribution modeled in PYTHIA was found to be vastly overestimated [109]. For this reason, muons produced in the final state by PYTHIA were excluded from the Monte Carlo sample and the definition of a hadron was restricted to pions, kaons, and protons.

The number of J/$\psi \to \mu^+\mu^-$ decays found for the 1997 polarized trigger 28 data set was found to be 7.29 with a background of 1.29 events [94]. Compared to the 262 events found for the high-p_T region of interest (defined by $p_T^{h_1} > 1.5$ GeV/c and $p_T^{h_2} > 0.8$ GeV/c, in addition to the cuts of section 3.5.4), this is at most a 3% effect.

A similar upper bound on J/ψ decay contamination was placed by using typical J/ψ mass cuts in the high-p_T region of interest. For $M(2\mu)$ in the range 3.0 to 3.1 GeV/c^2, 11 events were found. The cuts chosen based on the cuts used for 1997 standard tracking in Fig. 9 of Ref. [94]. This gives an upper bound on the contamination from this effect of about 4%. However, since no peak at the J/ψ mass was seen, it is suspected that the true contamination is likely much smaller than this, of the order 1%.

4.6 Extraction of f_i from PYTHIA

The fraction of events arising from each subprocess is extracted directly from Fig. 4-1. One simply divides the number of events from each subprocess type by the total number as in e.g. equations (1.41) and (1.42).

The fraction of events arising from each process type in the model implemented in PYTHIA is shown in Fig. 4-4. Where the PGF cross section is found to dominate is where the more negative asymmetry is seen (comparing with Fig. 3-2). In order to extract $\Delta G/G$, points in the asymmetry space were chosen if the PGF part of the

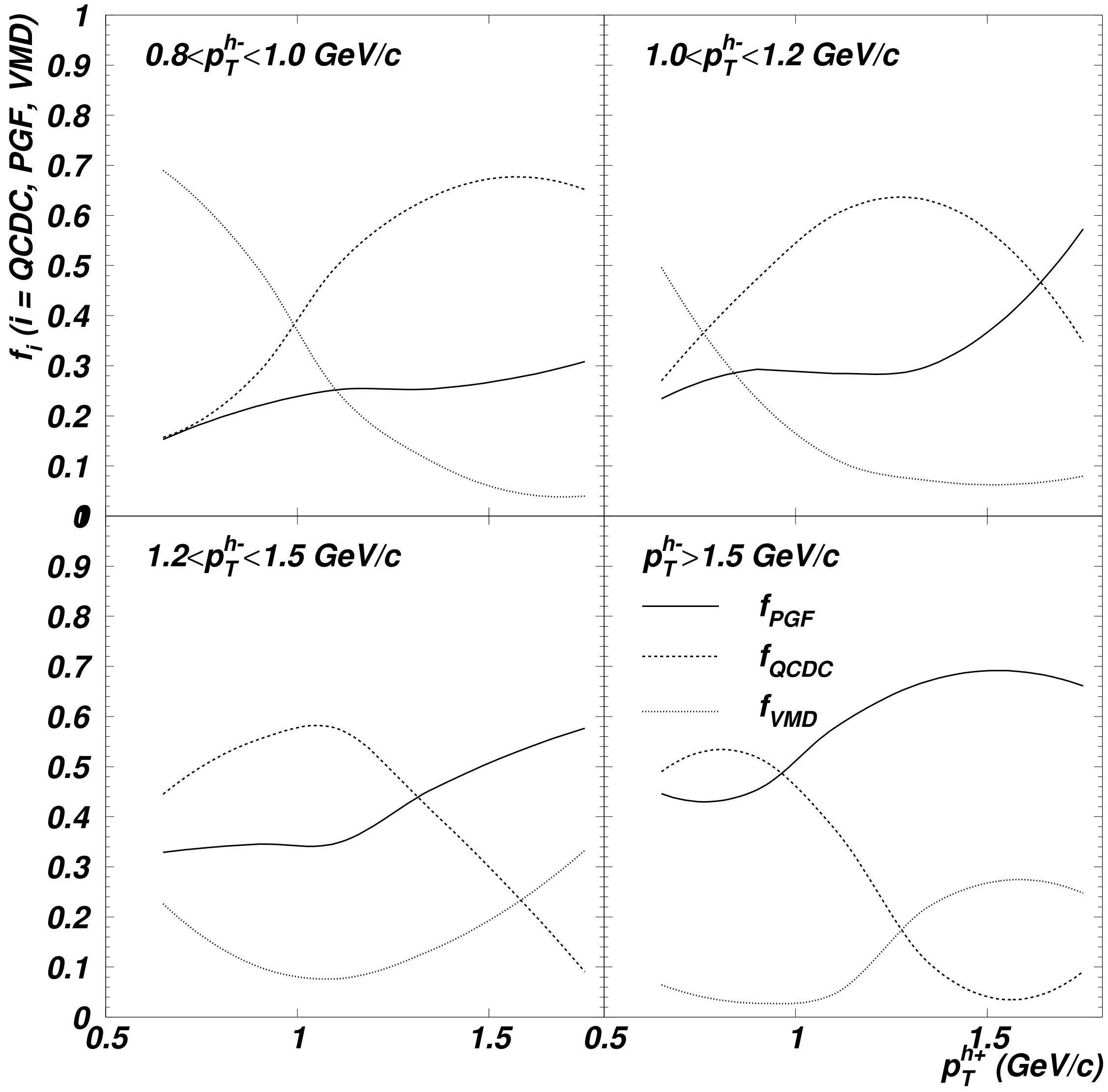

Figure 4-4: Monte Carlo prediction for fraction of events coming from each process type: PGF (solid line), QCDC (dashed), and soft VMD (dotted).

cross section was found to be significant in the Monte Carlo model. This turned out to be the same region where the Monte Carlo was found to be most stable under the variation of Monte Carlo parameters. The variation of these parameters will be discussed in further detail in section 4.8. The region selected for the analysis was $p_T^{h^\pm} > 1.5$ GeV/c and $p_T^{h^\mp} > 0.8$ GeV/c.

Figure 4-5 displays the result for f_i for each case ($p_T^{h^\pm} > 1.5$ GeV/c as a function of $p_T^{h^\mp}$). The background from QCDC is not significantly suppressed by the requirement

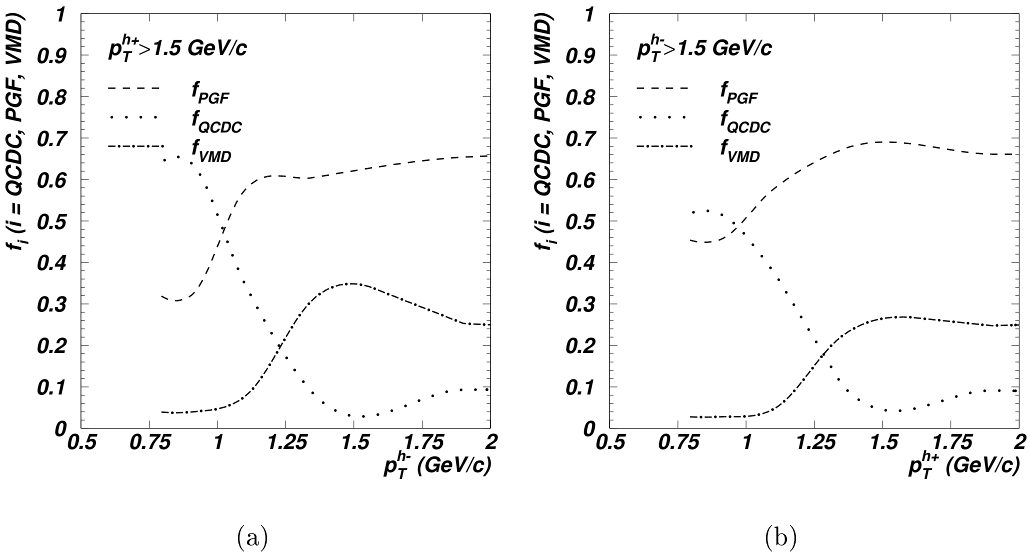

Figure 4-5: Fraction of events from each subprocess type for (a) $p_T^{h^+} > 1.5$ GeV/c, (b) $p_T^{h^-} > 1.5$ GeV/c. The three curves correspond to PGF (dashed), QCDC (dotted), and VMD (dot-dashed).

of a high p_T for the negative hadron, as opposed to a high p_T for the positive one. There is only a difference for $p_T^{h_2} \simeq 0.8$ GeV/c, where the QCDC background is more significant. This was unfortunate, as it was hoped that this background would explain why a less negative asymmetry was measured for $p_T^{h^+} > 1.5$ GeV/c compared to the case where $p_T^{h^-} > 1.5$ GeV/c.

Since the two plots are rather similar, they will be averaged. In this way, f_i is plotted as a function of $p_T^{h_2}$ for $p_T^{h_1}$. The result is shown in Fig. 4-6. Here, the

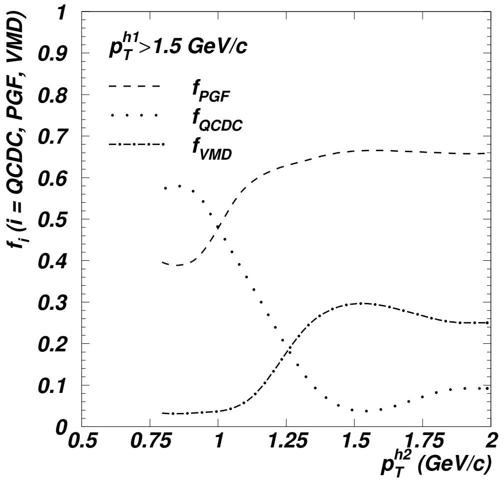

Figure 4-6: Fraction of events from each subprocess type for $p_T^{h_1} > 1.5$ GeV/c, as a function of $p_T^{h_2}$. The three curves correspond to PGF (dashed), QCDC (dotted), and VMD (dot-dashed).

designations h_1 and h_2 refer to the fact that there are two hadrons which carry opposite charge, the distinguishing characteristic being that one of them (h_1) has a p_T greater than 1.5 GeV/c. Note that this form of presentation is only for display purposes. The unaveraged in charge distributions are used for the actual extraction of $\Delta G/G$.

4.7 The result for $\Delta G/G$ in the "best" model

In the same way that f_i may be averaged over charge in this model, the data on $A_{||}$ can be averaged and the number of counts $dN/p_T^{h_2}$ can be summed. The result of doing so is shown in Figs. 4-7 and 4-8, respectively.

Performing the averaging for $A_{||}$ is reasonable since the measurements of corresponding bins are consistent, as seen in Fig. 4-7(a).

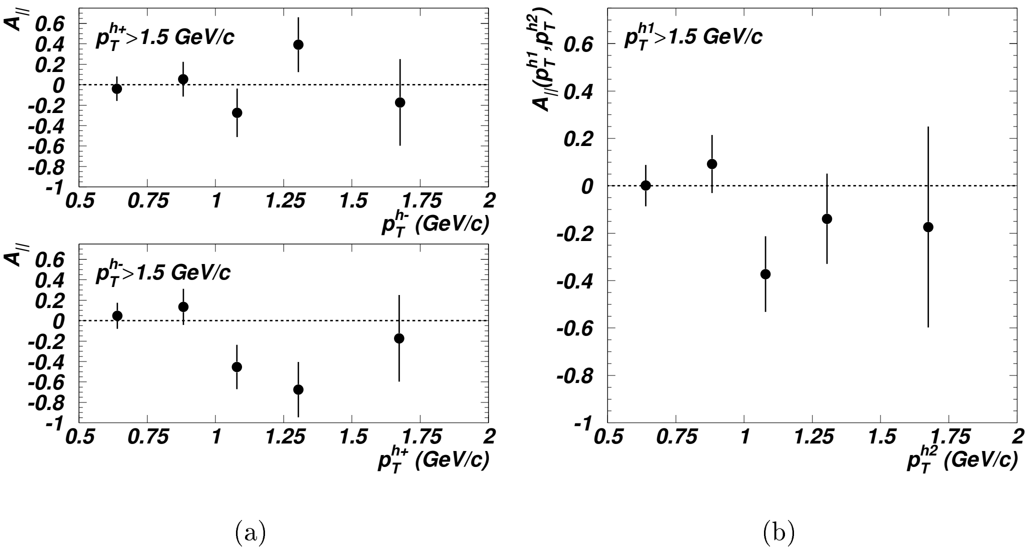

Figure 4-7: $A_{||}$: (a) for $p_T^{h^\pm} > 1.5$ GeV/c as a function of $p_T^{h^\mp}$, and (b) for $p_T^{h_1} > 1.5$ GeV/c as a function of $p_T^{h_2}$.

It is interesting to note that the averaged quantity $A_{||}(p_T^{h_1}, p_T^{h_2})$ is very nearly the quantity in two hadron photoproduction suggested by Fontannaz et al in Ref. [9] to be most sensitive to $\Delta G/G$. They found that, for only PGF and QCDC contributing to the real photoproduction cross section, the spin asymmetry

$$A^F(\vec{p}_1, \vec{p}_2) = \frac{F_{++}(\vec{p}_1, \vec{p}_2) - F_{+-}(\vec{p}_1, \vec{p}_2)}{F_{++}(\vec{p}_1, \vec{p}_2) + F_{+-}(\vec{p}_1, \vec{p}_2)} \tag{4.4}$$

with reasonable assumptions about the symmetry properties of fragmentation functions is directly related to the gluon polarization, viz:

$$A^F(\vec{p}_1, \vec{p}_2) = -\frac{\Delta G(x, Q^2)}{G(x, Q^2)}. \tag{4.5}$$

This is due to the fact that effects from QCDC cancel out for the suitably defined

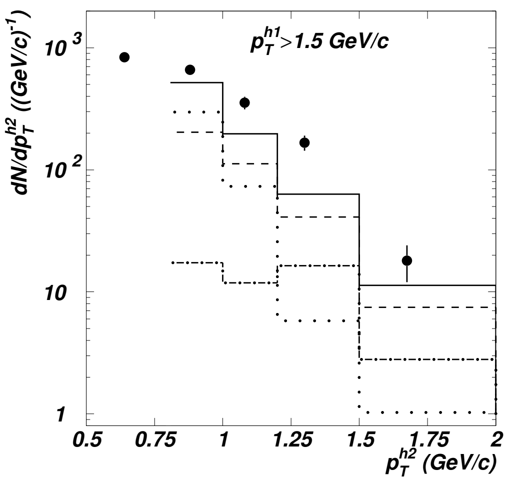

Figure 4-8: $dN/p_T^{h_2}$ for $p_T^{h_1} > 1.5$ GeV/c. The four curves correspond to Monte Carlo predictions for total (solid) PGF (dashed), QCDC (dotted), and VMD (dot-dashed). This is essentially the sum of Figs. 4-1(a) and (b), with the last bin in each not being double counted as it is identical in each figure.

"double inclusive cross section difference":

$$F(\vec{p}_1, \vec{p}_2) \equiv \frac{d\sigma(\gamma p \to \pi^+\pi^- X)}{d\vec{p}_{T1} dy_1 dp_{2x} dy_2} + \frac{d\sigma(\gamma p \to \pi^-\pi^+ X)}{d\vec{p}_{T1} dy_1 dp_{2x} dy_2} - \frac{d\sigma(\gamma p \to \pi^+\pi^+ X)}{d\vec{p}_{T1} dy_1 dp_{2x} dy_2} - \frac{d\sigma(\gamma p \to \pi^-\pi^- X)}{d\vec{p}_{T1} dy_1 dp_{2x} dy_2}. \tag{4.6}$$

Here, the ordering in the $\gamma p \to \pi^1 \pi^2 X$ shows which pions belong to the designations 1 and 2. In the limit that $d\sigma(\gamma p \to \pi^+\pi^+ X)$ and $d\sigma(\gamma p \to \pi^-\pi^- X)$ are small compared to the opposite charge combinations, $A_{||}(p_T^{h_1}, p_T^{h_2})/D(y)$ is equal to $A^F(\vec{p}_1, \vec{p}_2)$ integrated over the rapidities y_1 and y_2. The same charge combinations are found to have cross sections roughly a factor of 10 smaller than the opposite charge combinations. The same conclusion is reached in the PYTHIA model of these cross sections.

Ref. [9] unfortunately relies on event topologies and the relatively high p_T of the jets to separate these effects from photon structure effects. HERMES can certainly not do this due to its small forward acceptance, and must estimate the backgrounds in Monte Carlo.

4.7.1 Procedure for Extracting $\Delta G/G$

The procedure used to extract $\Delta G/G$ was to determine $\Delta G/G$ for each p_T bin in the region of interest separately (using equation (1.43)) and then to average the results. This turns out to be very nearly equivalent to calculating $A_{||}$ in the model for given $\Delta G/G$ ansatz, then varying the ansatz to find the best fit. This means that the averaging approximations made in equation (1.43) are rather good.

Note that in using equation (1.43), it is implicitly assumed that the contribution of the VMD processes has zero spin asymmetry. This is known to be a relatively good assumption, as the spin asymmetry measured in lower-p_T domains, where VMD processes are expected to dominate, is in good agreement with zero. The same result is naively expected from VMD considerations assuming s-channel helicity conservation (SCHC) [23]. This is apparently at odds with a recent HERMES result where the spin asymmetry in exclusive ρ^0 meson production was measured to be non-zero [110]: $A_{||} \simeq \langle D \rangle \langle A_1 \rangle \simeq 0.4 \times (0.30 \pm 0.13) = 0.12 \pm 0.05$. This measurement was performed with the scattered positron in the acceptance and therefore at finite $Q^2 \gtrsim 1.0$ (GeV/c)^2. The spin asymmetry in inclusive ρ^0 photoproduction (with scattered positron not observed in the acceptance) has been found to be in agreement with zero [104], in accord with SCHC and with the lower-p_T points in the asymmetry space displayed in this thesis (see Fig. 3-2).

Several other quantities that are needed in equation (1.43) to calculate $\Delta G/G$ must be determined in the Monte Carlo. The quantities and their values are catalogued in Table 4.2. The product $\langle D\hat{a}_{\mathrm{QCDC}} \frac{\Delta q}{q} \rangle$ was estimated using a polarized DIS generator (PEPSI) at low Q^2 ($Q^2 < 1$ (GeV/c)^2), resulting in a value of 0.15. This is consistent with determining $\langle D\hat{a}_{\mathrm{QCDC}} \rangle$ using PYTHIA and multiplying by $\Delta u/u$ at the average x_q probed. The result of this calculation is $\langle D\hat{a}_{\mathrm{QCDC}} \rangle \frac{\Delta u}{u}(\langle x_q \rangle) = 0.13$. The difference between 0.15 and 0.13 gives a negligible difference when applied to

Quantity	Value	Source
$\langle D(y)\hat{a}_{\mathrm{QCDC}}\frac{\Delta q}{q}\rangle$	0.15	PEPSI, PYTHIA, data
$\langle\hat{a}_{\mathrm{PGF}}\rangle$	-1	LO QCD
$\langle D(y)\rangle$	0.9	PYTHIA, WWA
A_{VMD}	0	see text
$f_{\mathrm{PGF}}, f_{\mathrm{QCDC}}, f_{\mathrm{VMD}}$	see plot	PYTHIA
$\langle x_G\rangle$	0.17	PYTHIA
$\langle\hat{p}_T^2\rangle$	2.1 GeV^2	PYTHIA
$\langle Q^2\rangle$	0.06 GeV^2	PYTHIA, WWA

Table 4.2: Quantities relevant to the extraction of $\Delta G/G$ and their sources.

the extraction of $\Delta G/G$ since the QCDC background is small in this region of phase space. Variations in this quantity due to using different phenomenological fits for the polarized quark distributions are expected to give an even smaller difference. The systematic error due to the determination of this quantity can therefore be safely ignored.

In the above discussion, x_q is defined as the fraction of the nucleon momentum carried by the initial quark which participates in the reaction, and x_G is the corresponding quantity for gluons. The quantities x_q and x_G can be determined by examining the kinematics of the underlying subprocess: $x_q = x_G = \frac{\hat{s}+Q^2}{2M\nu}$ where $\hat{s}$ is the photon-parton center of mass energy.

The subprocess asymmetry $\langle\hat{a}_{\mathrm{PGF}}\rangle$ is taken to be exactly -1, as it is for real photons, and $\langle D\rangle$ is 0.93.

The average y is expected to be large, as the total energy of the detected final state hadrons is 18.6 GeV on average for the selected events. Thus it is expected that $\langle y\rangle \gtrsim 18.6/27.5 = 0.68$. Indeed, this is in agreement with the Monte Carlo expectation of $\langle y\rangle = 0.86$ and the difference between these two quantities is also as expected. The difference is due to the small acceptance of the spectrometer and the consequent non-exclusiveness of the detection.

The average values of x_G, Q^2 and $\hat{p}_T^2$ for events with the selected kinematics have been determined from PYTHIA to be $\langle x_G \rangle = 0.17$, $\langle Q^2 \rangle = 0.06$ $(\mathrm{GeV/c})^2$, and $\langle \hat{p}_T^2 \rangle = 2.1$ $(\mathrm{GeV/c})^2$. Note that the hard scale of this process is not given by Q^2, but rather by $\hat{p}_T^2$, the transverse momentum of the outgoing quarks produced in photon gluon fusion.

For the four highest p_T values in each of the plots presented in Fig. 4-7(a), $\Delta G/G$ was extracted according to equation (1.43). The measurements probed essentially the same range of x_G, justifying averaging them together. Using the assumptions and model parameters described above, a value for $\Delta G/G$ was thus extracted. This value was determined to be 0.41 ± 0.18 (stat.) $\pm\, 0.03$ (exp. syst.). The experimental systematic uncertainty is dominated by target and beam polarization uncertainties.

As was mentioned already, the model chosen to extract $\Delta G/G$ does not describe the cross section well, and therefore cannot represent a complete description of the data. Several studies of the Monte Carlo were conducted in an attempt to at least partially resolve the discrepancy and quantify a model dependence systematic uncertainty for the value of $\Delta G/G$.

4.8 Additional PYTHIA studies

Several PYTHIA studies were carried out in an attempt both to quantify a theoretical systematic uncertainty on the determination of $\Delta G/G$, and to resolve the discrepancy between the Monte Carlo and the data in terms of the absolute normalization of the cross section. The additional studies that were performed include:

- variation of $\hat{p}_T^{\mathrm{min}}$ parameter. Quantification of dependence of $\Delta G/G$ extraction on the variation.

- inclusion of different processes from "anomalous" photon structure in PYTHIA.

- variation of intrinsic k_T of the initial state partons in the proton in PYTHIA.

- checks of the "leading particle effects". Attempt to determine whether or not PYTHIA can reproduce the naive expectation that PGF should dominate for high $p_T^{h^-}$ as opposed to high $p_T^{h^+}$ (since p_T is correlated to z).
- comparison of PYTHIA cross section predictions to other photoproduction data at similar energies.
- variation of JETSET fragmentation parameters in an attempt to recover missing cross section.

These studies will now be discussed.

4.8.1 Variation of the $\hat{p}_T^{\text{min}}$ parameter

The $\hat{p}_T^{\text{min}}$ parameter is the infrared cut-off for the LO QCD matrix elements that are required for the calculation of the cross section in PYTHIA. Any dependence of the result on the $\hat{p}_T^{\text{min}}$ parameter indicates a model dependence of the result due to the interpretation in leading order.

The $\hat{p}_T$ value for each event can be determined in the Monte Carlo. The PGF cross section as a function of $\hat{p}_T^{\text{min}}$ is presented in Fig. 4-9(a), and the QCDC cross section in Fig. 4-9(b). In each plot, the sharp, artificial cut-off at $\hat{p}_T^{\text{min}} = 0.5$ GeV/c can be seen. This indicates that if this cut-off parameter were changed, the cross section (integrated over this variable) would change significantly. However, in Fig. 4-9(a), for $p_T^{h^-} > 1.5$ GeV/c, the cross section becomes nearly independent of the p_T^{min} cut-off. The same observation is made for the case of $p_T^{h^+} > 1.5$ GeV/c (not shown). This also is in agreement with the rule-of-thumb expectation from experience with these type of simlulations that the p_T^{min} cut-off should be of the order three times smaller than the typical p_T scale involved in the problem [103]. However, Fig. 4-9(b) demonstrates that the QCDC cross section will have a residual dependence. To minimize the dependence, only points with $p_T^{h^\pm} > 1.5$ GeV and $p_T^{h^\mp} > 0.8$ GeV were used for the determination of $\Delta G/G$.

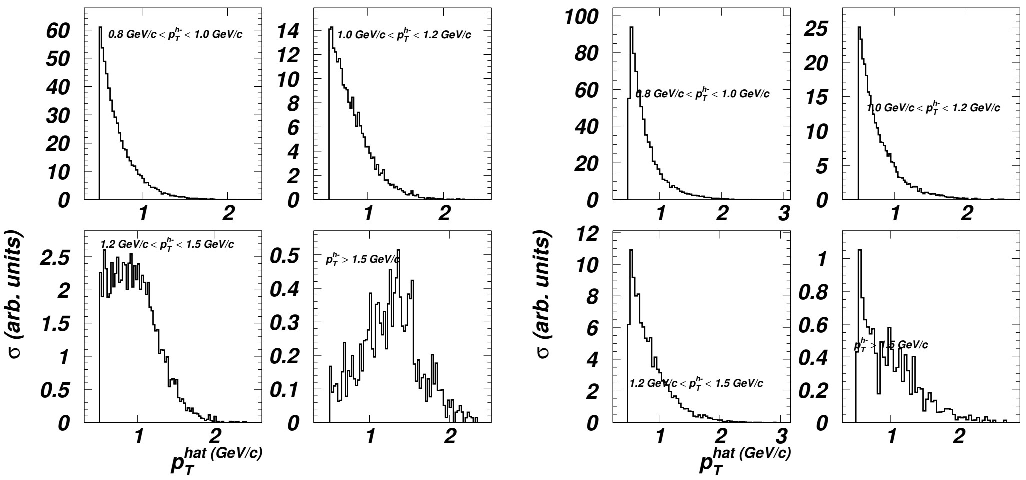

(a) PGF

(b) QCDC

Figure 4-9: $\sigma_{\rm PGF}$ and $\sigma_{\rm QCDC}$ vs. $\hat{p}_T$ for different cuts on hadronic variables. For all plots, the requirements $p_T^{h^+} > 0.5$ GeV/c and $M(2\pi) > 1.0$ GeV/c^2 have been enforced, in addition to the $p_T^{h^-}$ cut indicated on each graph.

Another way of looking at this question is to examine the dependence of the cross section determined in PYTHIA in the $p_T^{h^+}$-$p_T^{h^-}$ space for different $\hat{p}_T^{\rm min}$ cut-offs, as is done in Fig. 4-10. It can be seen that the PGF cross section is stable in the region $p_T^{h^\pm} > 1.5$ GeV and $p_T^{h^\mp} > 0.8$ GeV against variation of $\hat{p}_T^{\rm min}$ from 0.5 to 0.7 GeV/c. The QCDC cross section, shown in Fig. 4-10(b), exhibits some dependence. However, its contribution is also found to be subdominant compared to the PGF cross section.

The effect of changing $\hat{p}_T^{\rm min}$ within reasonable bounds on the result for $\Delta G/G$ is tabulated in Table 4.3. In all three cases, the same model of soft VMD processes is used. The result for $\Delta G/G$ is found to decrease slightly when increasing the $\hat{p}_T^{\rm min}$ cut-off from 0.5 to 0.7 GeV/c.

The fact that a region of the phase space can be found where the Monte Carlo is relatively stable against variations of the $\hat{p}_T^{\rm min}$ parameter implies that the Monte Carlo is applicable in this region of phase space.

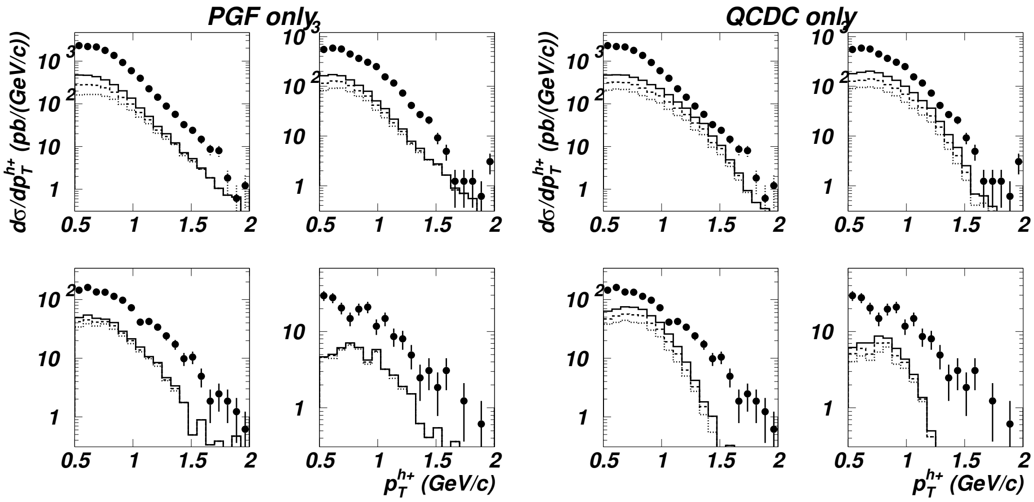

(a) PGF (b) QCDC

Figure 4-10: $d\sigma_{\mathrm{PGF}}/dp_T^{h^+}$ and $d\sigma_{\mathrm{QCDC}}/dp_T^{h^+}$ vs. $p_T^{h^+}$ for various bins in $p_T^{h^-}$. Three Monte Carlo predictions (curves) are compared with the data (points). The three curves correspond to $\hat{p}_T^{\mathrm{min}} = 0.5$ GeV/c (solid), 0.6 GeV/c (dashed), and 0.7 GeV/c (dotted) in the Monte Carlo.

4.8.2 Hard VMD Processes and Anomalous Photon Structure

The inclusion of anomalous photon structure and hard VMD processes was found to improve the agreement between the Monte Carlo cross section at high p_T and the data.

As described in Ref. [27], the VMD processes were included above $\hat{p}_T^{\mathrm{min,\ VMD}} = 1.0$ GeV/c.

In the version of PYTHIA employed for the task of describing the HERMES data [97], it was found that the default setting for the anomalous photon $\hat{p}_T^{\mathrm{min,\ anom.}}$ had been changed to the order of the direct cut-off $\hat{p}_T^{\mathrm{min,\ dir.}}$. The reason for the change was not clear, but was likely motivated by the desire to describe e^+e^- collider cross sections

Model	$\hat{p}_T^{\rm min}$ (GeV/c)	$\Delta G/G$
PT1	0.5	0.41 ± 0.18
PT2	0.6	0.39 ± 0.17
PT3	0.7	0.35 ± 0.16

Table 4.3: Dependence of result for $\Delta G/G$ on $\hat{p}_T^{\rm min}$ cut-off in PYTHIA. Soft VMD processes are included in all three cases in the same way.

instead of *ep* cross sections. This becomes apparent when reading the discussion of the relevant p_T scales in Ref. [27].

For ep scattering, however, it seems that reducing the $\hat{p}_T^{\text{min, anom.}}$ to $\hat{p}_T^{\text{min, dir.}}$ may even double count events, due to the fact that the subprocess topology of such events is essentially identical to direct events. For example, suppose an incident photon splits into a $q\bar{q}$ pair and one of these quarks scatters from a gluon. It is the scale at which the splitting and the scale at which the scattering occurs which determines whether this is an anomalous photon event, or a direct photon event. If these scales are equal, the event should be considered as photon gluon fusion.

The cross sections presented in this section therefore likely have little physical meaning, since (a) the anomalous photon scales used are of the order of the direct photon scale; and (b) the hard VMD cut-off is unphysically large for the processes under consideration. The hard VMD and anomalous processes in PYTHIA are used simply as a tool to describe the cross section, thereby estimating the background from possible missing processes. For example, it is possible that the background from VMD has been underestimated but is well modeled by these seemingly unphysical processes in PYTHIA.

The ability of these processes to make up the missing cross section is displayed in Fig. 4-11. The $\hat{p}_T^{\rm min}$ cut placed was constrained to be the same for the hard photon structure and direct processes.

The effect of including only the hard VMD processes (and not the anomalous processes) is shown in Fig. 4-12. The case where both hard and soft VMD processes

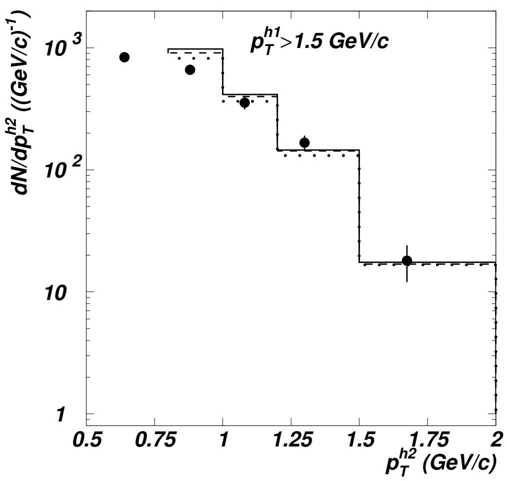

Figure 4-11: $dN/p_T^{h_2}$ for $p_T^{h_1} > 1.5$ GeV/c. The data (points) are compared to three different Monte Carlo predictions including anomalous and direct photons above $\hat{p}_T^{\text{min, anom., dir.}} = 0.5$ GeV/c (solid), 0.6 GeV/c (dashed) and 0.7 GeV/c (dot-dashed).

are included is interesting because, even though including the hard processes above $\hat{p}_T = 1.0$ GeV/c to describe physical p_T's of order 1.5 GeV/c makes no sense, the soft and hard overlap has supposedly been tuned to occur at this $\hat{p}_T$. Indeed, it was found that changing $\hat{p}_T^{\text{min, VMD}}$ from its value of 1.0 GeV/c had an effect on the soft VMD processes.

Another model including anomalous photons above the same $\hat{p}_T$ cut-off as the hard VMD processes was investigated, as this option is included in PYTHIA. This model gives a description of the cross section somewhere between the hard+soft VMD only model and the full anomalous models.

The effect of using the different models on the result for $\Delta G/G$ is shown in Table 4.4. Here, it is assumed that, as for soft VMD processes, the hard VMD and anomalous photon structure processes have zero spin asymmetry, presenting only a dilution to the measured asymmetry. This is the only assumption that can be made, as no experimental data on the spin structure of the photon exist. Current theo-

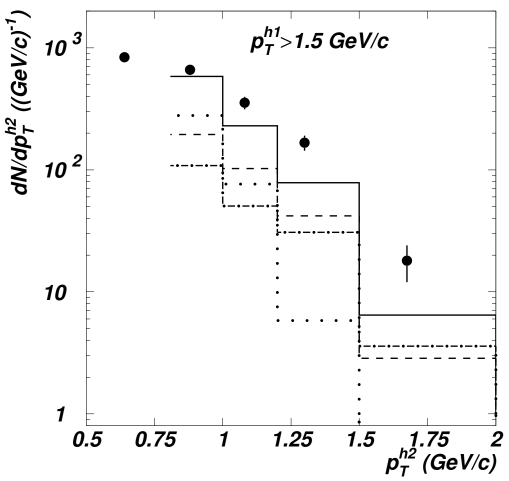

Figure 4-12: $dN/p_T^{h_2}$ for $p_T^{h_1} > 1.5$ GeV/c. Anomalous photons are removed, but hard VMD processes are included above $\hat{p}_T^{\mathrm{VMD}} = 1.0$ GeV/c. The various curves are the total (solid) and the contributions from PGF (dashed), QCDC (dotted), and "soft+hard" VMD (dot-dashed).

retical predictions for the polarized photon structure functions $\Delta f^{\gamma}(x)$ indicate that this should be a good estimate [111, 112]. Note that the significance of the result $\delta(\Delta G/G)/(\Delta G/G)$ therefore does not change.

If it is claimed that none of the anomalous, hard, or soft VMD photons are correctly described in PYTHIA, the direct processes in PYTHIA can still be used to make an extraction of $\Delta G/G$. However, the cross section will still be low by roughly a factor of two. The result for $\Delta G/G$ in this model is 0.33 ± 0.14. This is the minimal possible result for $\Delta G/G$, unless the model of the direct photon changes significantly.

4.8.3 Variation of fragmentation parameters

The JETSET parameters `PARJ(21)`, `PARJ(41)`, and `PARJ(42)` are used to control the model of the fragmentation process. As mentioned briefly earlier, these parameters have been tuned to describe HERMES semi-inclusive deep-inelastic scattering cross

Model	$\hat{p}_T^{\text{min, direct}}$ (GeV/c)	anom. on? (yes/no)	$\hat{p}_T^{\text{min, anom.}}$ (GeV/c)	hard VMD on? (yes/no)	$\hat{p}_T^{\text{min, VMD}}$ (GeV/c)	$\Delta G/G$
ANM1	0.5	yes	0.5	yes	1.0	0.83 ± 0.38
ANM2	0.6	yes	0.6	yes	1.0	0.79 ± 0.37
ANM3	0.7	yes	0.7	yes	1.0	0.73 ± 0.35
ANM4	0.5	yes	1.0	yes	1.0	0.64 ± 0.24
ANM5	0.5	no	–	yes	1.0	0.46 ± 0.20

Table 4.4: Dependence of result for $\Delta G/G$ on inclusion of different levels of anomalous and hard VMD processes. VMD processes are included in all cases in the same way, but differ from previous sections in that hard VMD processes are now included in addition to soft VMD.

sections for hadrons [113, 114, 115].

It is not clear that the parameters used for semi-inclusive physics are relevant to photoproduction, though ideally they should be the same. They could be different due to the fact that the average W^2 for the DIS processes is considerably lower than that for the photoproduction processes. To study the effect of varying the fragmentation parameters, a Monte Carlo study was carried out where these parameters were returned to their default values in JETSET (tuned to fragmentation at EMC with parton showers included).

The agreement between the MC cross section and that measured in the data improves when using the default fragmentation parameters. However, the MC cross section still underestimates the data. This is demonstrated in Fig. 4-13. When using the EMC parameters, the result for $\Delta G/G$ changed to 0.32 ± 0.16. This will be referred to as model FRAG in the following sections.

4.8.4 Variation of Intrinsic k_T

The PYTHIA parameter `PARP(91)` can be used to control the intrinsic k_T of the initial state partons inside the nucleon. From deep-inelastic scattering experiments, this quantity has been determined to be $k_T = 0.44$ GeV/c [28, 29], though the parameter

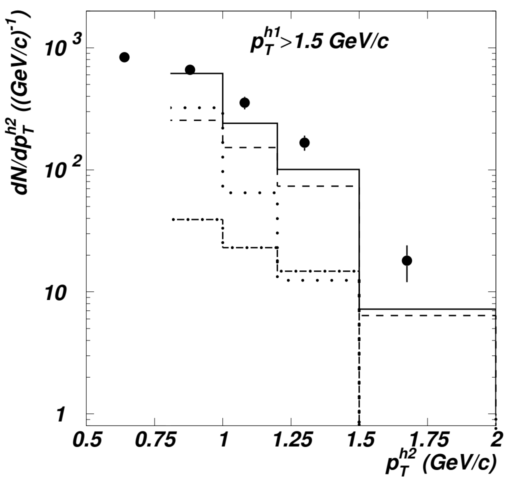

Figure 4-13: $dN/p_T^{h_2}$ for $p_T^{h_1} > 1.5$ GeV/c using default fragmentation parameters for JETSET. Contributions from PGF (dashed), QCDC (dotted), and soft VMD (dot-dashed) are displayed.

needed to be increased to 0.88 GeV/c if parton showers were not included in the model of fragmentation. Current parton shower codes have been found not to work for HERMES kinematics [113]. However, the fragmentation parameters described in section 4.8.3 were tuned to describe the fragmentation process [113, 114, 115]. The value 0.44 GeV/c is the default setting used in PYTHIA, and this setting was held fixed when tuning the HERMES semi-inclusive hadron distributions to LEPTO generated cross sections.

Increasing the intrinsic k_T was found to improve the agreement between the Monte Carlo and data cross sections at high p_T. This is demonstrated in Fig. 4-14, where the setting for k_T has been increased to 1.0 GeV/c. The value of $\Delta G/G$ determined in this model is 0.41 ± 0.18. This will be referred to as model KT in section 4.9.

It is interesting to note that increasing the intrinsic transverse momentum significantly, as high as scales of order 1.2-1.3 GeV/c has been found to bring NLO calculations of the prompt photon and hadron production cross section in proton

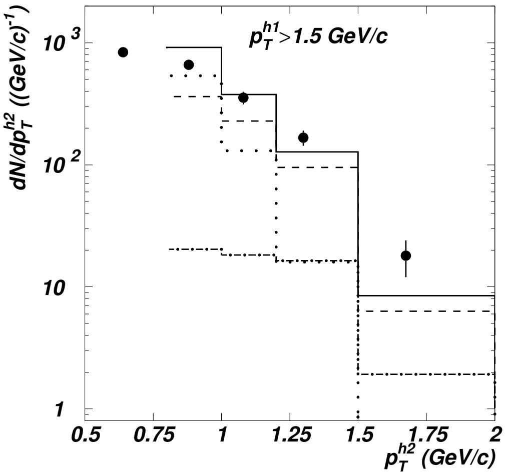

Figure 4-14: $dN/p_T^{h_2}$ for $p_T^{h_1} > 1.5$ GeV/c using HERMES tuned fragmentation parameters, but with intrinsic k_T (`PARP(91)`) set to 1.0 GeV/c. Contributions from PGF (dashed), QCDC (dotted), and soft VMD (dot-dashed) are displayed.

scattering from light targets into agreement with data [116, 117]. However, resummation of the NLO contributions also tends to bring the prompt photon cross sections into better agreement [118].

4.8.5 The relationship between $\hat{p}_T^{\min}$, Anomalous Photons, Intrinsic k_T, fragmentation parameters and NLO Effects

The effects that have been discussed so far are modifications of the usual soft VMD plus direct photon model in an attempt to better describe cross section dependences with p_T. It is possible that these are all embodiments of the same physical effect that cannot be described by LO QCD.

NLO contributions are another possibility to aid in the description of the cross section. As mentioned briefly at the end of the preceding section, contributions from NNLO resummations to high-p_T prompt photon production in pp collisions have been found to bring theory and data cross sections into better agreement, where these contributions were once assigned to intrinsic k_T effects.

NLO corrections to photoproduction cross sections may in principle be large [119]. In such calculations, it is typical to introduce a "K-factor" which is the ratio of the NLO cross section to the LO cross section. For the corrections presented in Ref. [120], K-factors of order 0.5 to 1 are seen at for COMPASS kinematics (at $\sqrt{s} = 20$ GeV, rapidity $\eta_{\rm CM} = 0$, and $p_T \gtrsim 2.0$ GeV/c). The range is based not on scale variations, but rather on variations of the unpolarized gluon structure function used at high x. The resolved photon NLO corrections to the cross section were not computed.

NLO computations have not been carried out for HERMES kinematics, but corrections to the unpolarized cross section are likely to be large. It is however possible that a partial cancellation of NLO terms in the polarized $\Delta\sigma$ and unpolarized σ cross sections may lead to a smaller change in the asymmetry $A_{||}$.

For reasons of simplicity, the analysis in this thesis was conducted in leading order. Estimates of NLO effects based on the literature mentioned above indicate that they could in principle be large, but the effect on the measured asymmetry $A_{||}$ is not at all clear.

From the studies presented above with variation of intrinsic k_T and fragmentation function parameters, it has been found that the description of the cross section can be improved, with minimal effect on the result for $\Delta G/G$. Inclusion of other processes, with an emphasis on possible missing processes such as hard VMD or anomalous photon contributions, has indicated that these could also play a role in making up the missing cross section. Assuming such processes present only a dilution of the PGF process, the result for $\Delta G/G$ increases. The spin structure of such processes is unknown, but it is expected that spin asymmetries of such processes should at least be vastly diluted compared to those for QCDC, PGF, or DIS [111, 112].

A model dependence uncertainty will be assigned to the result for $\Delta G/G$ based on these studies, in section 4.9.

4.8.6 Leading Particle Effects

The other studies conducted were used as checks of the plausibility of the information provided by the PYTHIA Monte Carlo.

In the data, it was observed that the measured asymmetry tends to be more negative for large $p_T^{h^-} > 1.5$ GeV/c as opposed to the case for large $p_T^{h^+}$. The significance of the difference is not great. The asymmetry measured for $p_T^{h^-} > 1.5$ GeV/c and $p_T^{h^+} > 0.8$ GeV/c is $A_{||} = -0.19 \pm 0.12$, whereas for $p_T^{h^+} > 1.5$ GeV/c and $p_T^{h^-} > 0.8$ GeV/c, it is $A_{||} = -0.01 \pm 0.13$. For a slightly larger cut on the lower-p_T hadron, the difference becomes more noticeable: $p_T^{h^-} > 1.5$ GeV/c and $p_T^{h^+} > 1.0$ GeV/c gives $A_{||} = -0.47 \pm 0.16$, where $p_T^{h^+} > 1.5$ GeV/c and $p_T^{h^-} > 1.0$ GeV/c gives $A_{||} = -0.03 \pm 0.17$. Since the transverse measured by the spectrometer tends to be closely related to the momenumtum of the track, this could be viewed as an effect based on which detected particle has higher momentum or is "leading".

The reason why a leading particle effect might be expected is due to the interplay of photon gluon fusion with its dominant background, the QCD Compton effect. In photon gluon fusion, a $q\bar{q}$ pair is produced in the final state; therefore, this process is expected to be charge symmetric for the production of h^+h^- pairs. The QCD Compton effect, however, directly probes the polarized quark distributions, leaving the struck quark and a radiated gluon in the final state. For a proton target, the cross section is dominated by scattering from u quarks, giving a positive asymmetry of roughly 0.15 for HERMES kinematics. The outgoing u quark fragments dominantly to positive hadrons, while the outgoing gluon has equal probability to fragment to a positive or negative hadron. It is therefore expected that leading positive hadrons will be a better tag of the QCDC process than leading negative hadrons. Assuming that PGF gives a negative asymmetry (i.e. that $\Delta G/G$ is positive), the asymmetry for leading positive hadrons should have a more positive asymmetry than that for leading negative hadrons.

Several tests were conducted to study leading particle effects in the Monte Carlo.

The initial indication that there is little or no leading particle effect in the PYTHIA Monte Carlo (at least based on the p_T of a given hadron) was presented in Figs. 4-5(a) and (b). These figures are repeated in Figs 4-15(a) and 4-16(a), along with predictions for the asymmetry $A_{||}$ compared with data, assuming a value for $\Delta G/G$ of 0.41 in Figs 4-15(b) and 4-16(b). The plots of f_i are slightly different than those in Fig. 4-5 due to the fact that a different method of smoothing the curves drawn through the bins was used. A leading particle effect is expected to arise based on the fact that

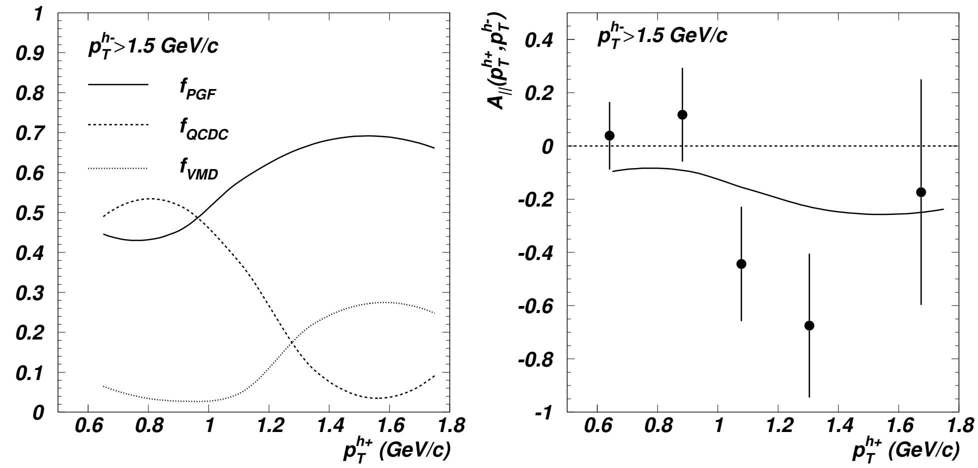

(a) (b)

Figure 4-15: f_i and $A_{||}$ compared with data, for $p_T^{h^-} > 1.5$ GeV/c.

the higher p_T of a given particle should be correlated to a higher momentum, and therefore a higher z for that particle. As described in section 1.2.3, this should lead to a suppression of QCDC for higher $p_T^{h^-}$ compared to the case for higher $p_T^{h^+}$. From Figs 4-15 and 4-16 it can be seen that the expected leading particle effect may be at most a 10% effect in the asymmetry, for the given binning. This seems at odds with the experimentally measured asymmetry which is apparently much more negative for higher $p_T^{h^-}$.

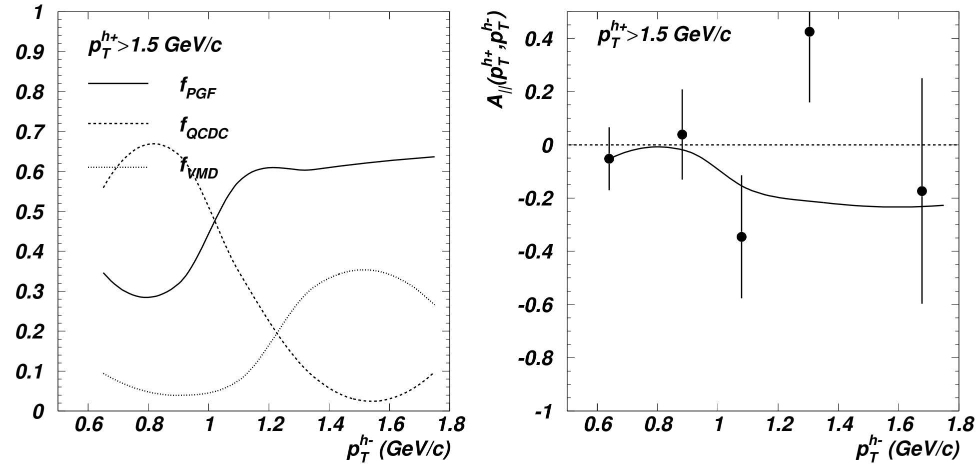

(a) (b)

Figure 4-16: f_i and $A_{||}$ compared with data, for $p_T^{h^+} > 1.5$ GeV/c.

A parallel analysis [90, 92] had chosen a different binning that seemed to show a leading particle effect in both the Monte Carlo and the data. The validity of the other analysis was verified in Ref. [91]. The results of the other analysis are displayed in Fig. 4-17 (courtesy Ref. [104]). In the other analysis, similar to the analysis in this thesis, a high-p_T cut (in this case set at 1.4 GeV/c) was made on one of the two hadrons under consideration. Then the cut on $M(2\pi)$ was varied to study the effect on the asymmetry. This is analogous to the variation of the p_T of the other particle. The value determined for $\Delta G/G$ in the other analysis (0.45 ± 0.20) is very consistent with the value determined in the analysis in this thesis.

Why is the leading particle effect evoked so nicely in the other analysis? The differences between the other analysis and the analysis of this thesis, aside from the binning, were the fact that it used an explicit leading particle cut ($p^{h^\pm} > p^{h^\mp}$) and the fact that it used only pions. The leading particle cut and the "pions only" cut were applied to both data and Monte Carlo to study the possible improvements to

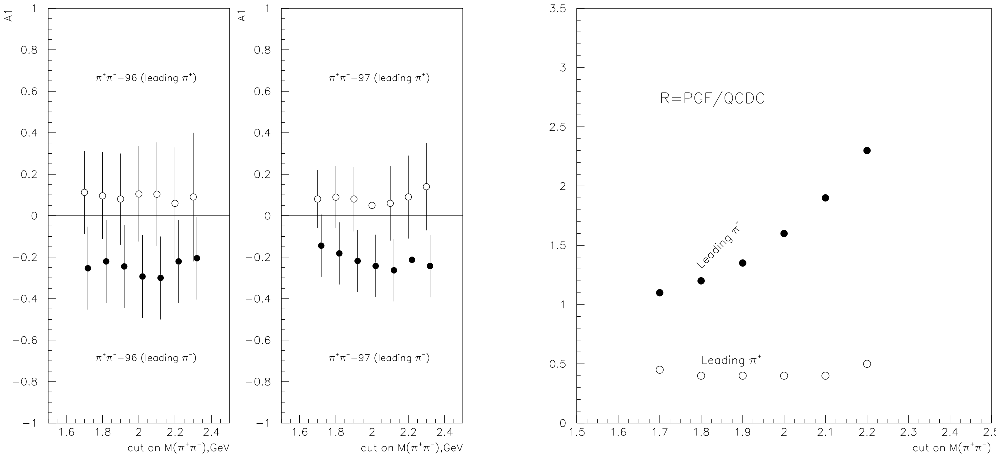

(a) (b)

Figure 4-17: (a) $A_{||}$ and (b) R for different leading particles [92]. Here, $R = \sigma_{\mathrm{PGF}}/\sigma_{\mathrm{QCDC}} = f_{\mathrm{PGF}}/(1 - f_{\mathrm{PGF}})$ and it was assumed that only PGF and QCDC contribute to the cross section.

the expected leading particle effects.

In Figs. 4-18 and 4-19, the leading particle cut has been applied. As expected, f_{PGF} changes slightly for both cases, having little effect on the predicted asymmetry. The case for the "pions only" cut was similar, having little effect on the suppression of the QCDC background compared to the "all hadrons" case.

A significant leading particle effect can be seen in regions of phase space where the background from QCDC is significant. For instance, the bin with $p_T^{h^-} > 1.5$ GeV/c, 0.8 GeV/c $< p_T^{h^+} < 1.0$ GeV/c has a considerably higher f_{PGF} and lower f_{QCDC} than the bin with $p_T^{h^+} > 1.5$ GeV/c, 0.8 GeV/c $< p_T^{h^-} < 1.0$ GeV/c, as expected from arguments regarding which particle is leading. The parallel analysis was determined to probe dominantly this region of phase space.

The conclusion of the comparison of the two binnings and the PYTHIA-based model is that leading particle effects are indeed correctly reproduced. However, for the

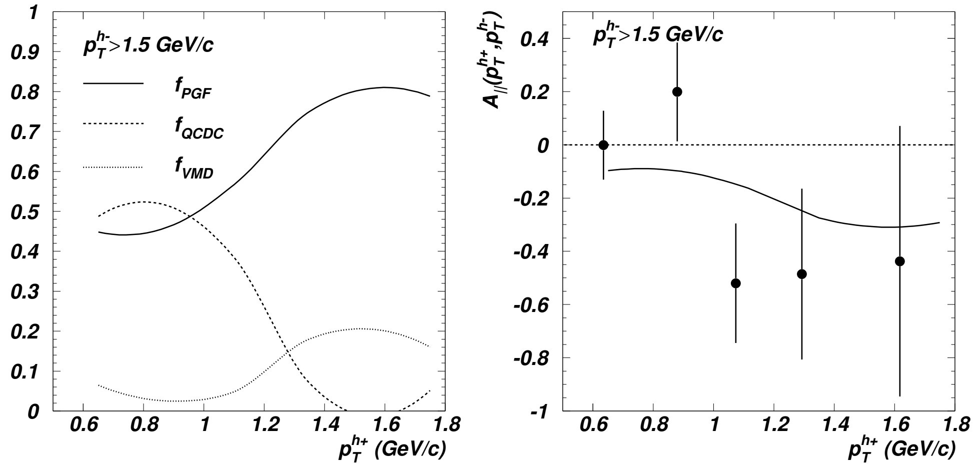

(a) (b)

Figure 4-18: f_i and $A_{||}$ compared with data, $p^{h^-} > p^{h^+}$, $p_T^{h^-} > 1.5$ GeV/c.

region of phase space selected by this analysis, the leading particle effects are small due to the fact that the QCDC background is found to be small. Though this is apparently at odds with the effect measured in $A_{||}$, no systematic uncertainty could be assigned due to the fact that the difference in $A_{||}$ for each leading charge type is not significant. In the worst case the difference is (for $p_T^{h^\pm} > 1.5$ GeV/c and $p_T^{h^\mp} > 1.0$ GeV/c) $(-0.47 \pm 0.16) - (-0.03 \pm 0.17) = -0.44 \pm 0.23$, which is 1.9 σ from zero. Comparing the data for which the fitting of $\Delta G/G$ is carried out ($p_T^{h^\pm} > 1.5$ GeV/c and $p_T^{h^\mp} > 0.8$ GeV/c) the difference is even less: $(-0.19 \pm 0.12) - (-0.01 \pm 0.13) = -0.18 \pm 0.18$ in good agreement with zero. Note that there is a slight correlation of the events in these data sets due to overlap in the region $p_T^{h^+} > 1.5$ GeV/c and $p_T^{h^-} > 1.5$ GeV/c; however, the overlap is small due to the small number of events in this bin and the correlation can therefore be ignored.

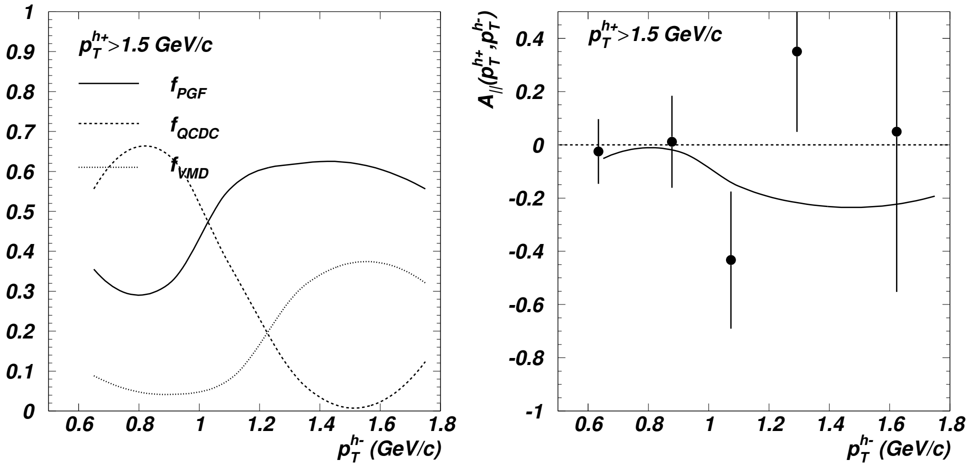

(a) (b)

Figure 4-19: f_i and $A_{||}$ compared with data, $p^{h^+} > p^{h^-}$, $p_T^{h^+} > 1.5$ GeV/c.

4.8.7 Comparison of PYTHIA to Other Experimental Data

Predictions from PYTHIA, using the default tuning of the code, were compared to inclusive hadron spectra from the WA69 experiment conducted by the OMEGA Photon Collaboration at CERN, and phenomenological predictions of the cross section. Both are reported in Ref. [121]. The main goal of WA69 was to understand the hadronic structure of the photon, and extract the contribution of direct photon processes. Pion, kaon, and photon beams of energies 80 and 140 GeV were scattered from a liquid-hydrogen target. The πp and Kp data were used to estimate the VMD background to the direct processes in the γp cross sections.

The relevant plots (Figs. 7, 10, and 12) from Ref. [121] may be found in Fig. 4-20. For the purpose of comparison to PYTHIA, the 80 GeV πp, Kp and γp data were used (left plot in each figure contained in Fig. 4-20). These plots correspond to:

- Fig. 7: $d\sigma/dp_T$ for all photoproduced hadrons in the forward hemisphere $x_F > 0$ (closed circles), compared with the VMD background deduced from the hadropro-

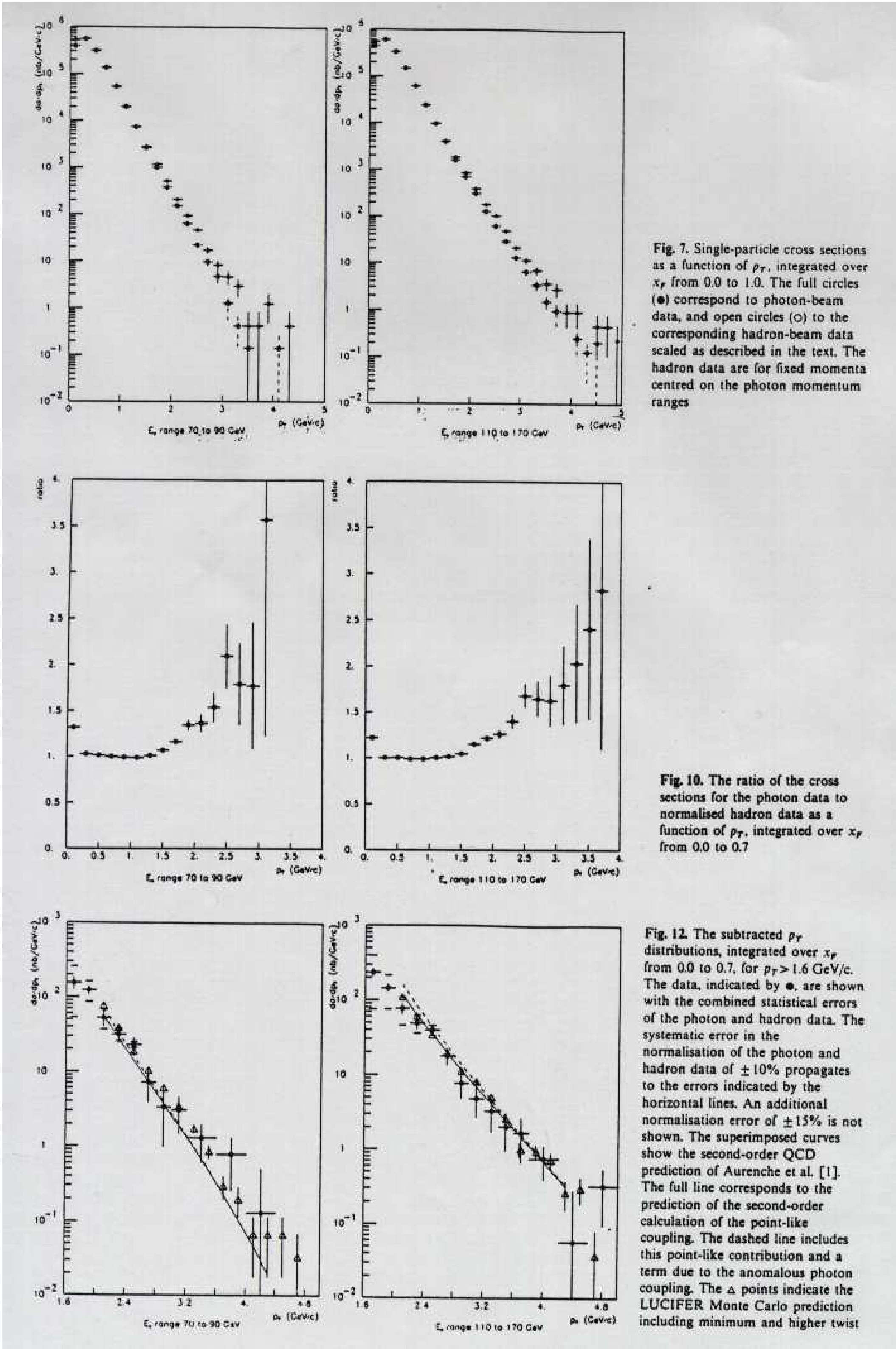

Figure 4-20: Figs. 7, 10, and 12 of Ref. [121]. The left plot in each (80 GeV data) was used for comparison.

duction data (open circles),

- Fig. 10: ratios of the cross sections in Fig. 7,
- Fig. 12: difference of the cross section in Fig. 7, compared to predictions for the direct photon cross section.

Since the curves in Fig. 12 of this publication agree so well with the data, one conclusion is that direct processes are well described by perturbative QCD. Another possible conclusion is that, since anomalous photon processes are not included in these calculations, anomalous photons are not necessary (to the level of statistics of the experiment) for describing high-p_T cross sections at fixed target energies.

To be compared with these plots are the predictions from PYTHIA for forward hadron photoproduction at 80 GeV. These predictions are shown in Figs. 4-21, 4-22 and 4-23, under different assumptions. The conclusion is that PYTHIA describes the WA69 data very well. Also, hard VMD and anomalous photon processes must be included in order to describe the cross section well.

4.9 Quantification of a Model Uncertainty

From the Monte Carlo studies of section 4.8, it is possible to quantify a partial model uncertainty. This uncertainty reflects the size of the effects in the Monte Carlo that have been studied so far.

Table 4.5 shows the range of models considered in section 4.8 and their effect on the result for $\Delta G/G$. In this analysis the "best" model refers to the most reasonable model of the photon at HERMES energies, as described in Ref. [27] and used early on in this chapter.

Rather than tune the processes included in the "best" model to fit the cross section data using $\hat{p}_T^{\min}$, fragmentation, or intrinsic k_T parameters, the effect of changing these parameters has been studied. Also, effects from unknown dilutions which may

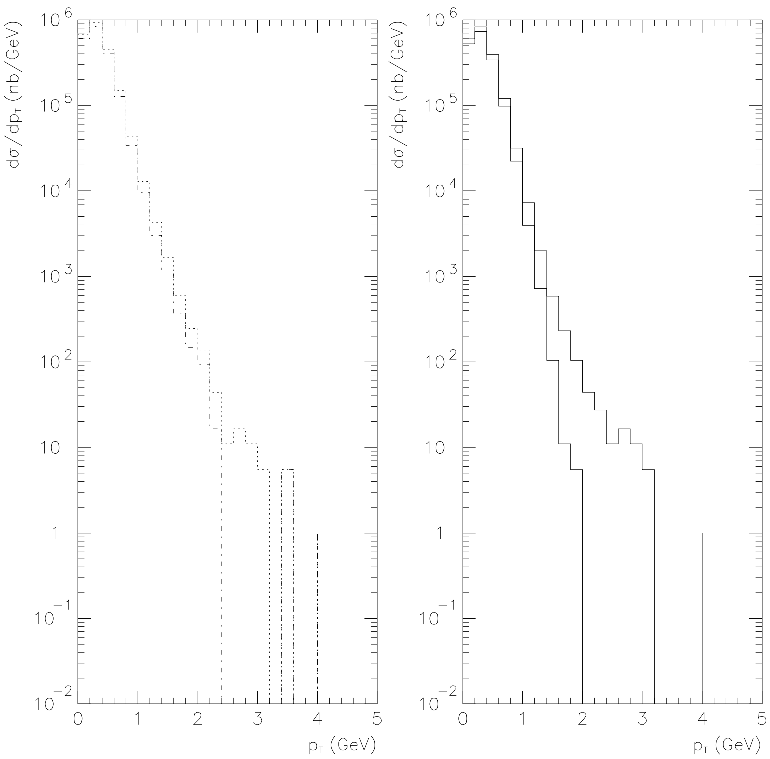

Figure 4-21: $d\sigma/dp_T$ for inclusive single charged particle production at 80 GeV (lab). This is to be compared with the left-hand plot of Fig. 7 of Ref. [121]. **Left plot**: upper curve is total $d\sigma/dp_T$ from PYTHIA (PGF+QCDC+VMD+anom.), lower curve is VMD+anom. **Right plot**: upper curve is PGF+QCDC+VMD(soft), lower curve is VMD(soft) only. The left plot agrees better with the WA69 data, implying that hard VMD processes are necessary to describe the single hadron cross section for these kinematics.

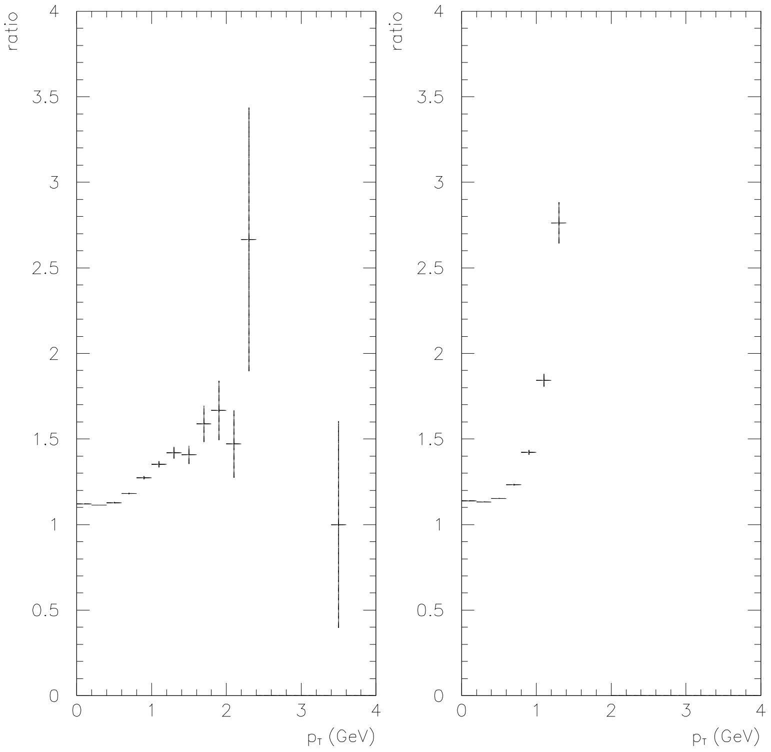

Figure 4-22: Ratios of $d\sigma/dp_T$ for inclusive single charged particle production at 80 GeV (lab). For PYTHIA this corresponds to (photon model)/(VMD model). This is to be compared with the left-hand plot of Fig. 10 of Ref. [121]. **Left plot**: ratio of curves in Fig. 4-21 left plot. **Right plot**: ratio of curves in Fig. 4-21 right plot. The left plot agrees better with the WA69 data.

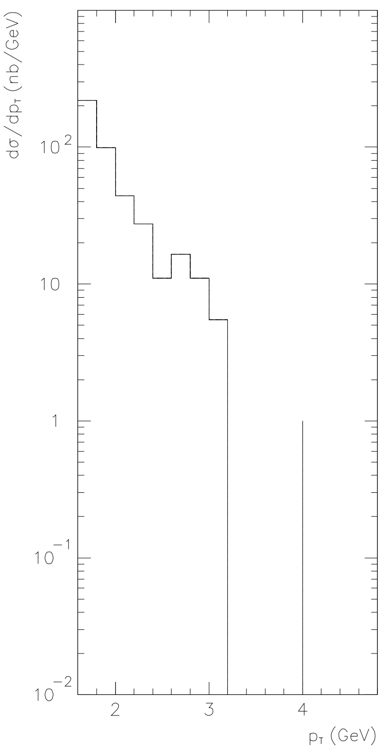

Figure 4-23: $d\sigma/dp_T$ for inclusive single charged particle production at 80 GeV (lab), PGF+QCDC only. This is to be compared with Fig. 12 of Ref. [121]. This shows that the direct processes extracted from the WA69 data are well described by the model implemented in PYTHIA, and that PYTHIA agrees with the models used in Ref [121].

Model	$\Delta G/G$	$\Delta G/G - (\Delta G/G)_{\text{best}}$
PT1	0.41 ± 0.18	0.00
PT2	0.39 ± 0.17	-0.02
PT3	0.35 ± 0.16	-0.06
ANM1	0.83 ± 0.38	$+0.42$
ANM2	0.79 ± 0.37	$+0.38$
ANM3	0.73 ± 0.35	$+0.32$
ANM4	0.64 ± 0.24	$+0.23$
ANM5	0.46 ± 0.20	$+0.05$
FRAG	0.32 ± 0.16	-0.09
KT	0.41 ± 0.18	0.00

Table 4.5: Effect of different PYTHIA models on result for $\Delta G/G$.

make up the missing cross section, possibly from anomalous photons or hard VMD processes, were quantified. In magnitude, the effects of varying the fragmentation, k_T, and $\hat{p}_T$ parameters are small compared to the effect when adding possible dilutions. To cover the range of possibilities due to the lack of understanding of the cross section in the model in PYTHIA, an asymmetric error bar due to the possibilities studied so far has been assigned. Thus, the final result for $\Delta G/G$ is $\Delta G/G = 0.41 \pm 0.18 \pm 0.03^{+0.42}_{-0.09}$ where the first error is the statistical uncertainty, the second the experimental systematic uncertainty, and the third an estimate for the model dependence uncertainty.

The main effect that has not been quantified is the inclusion of possible NLO effects. The corrections due to such effects are known to be large for photoproduction cross sections at energies similar to the HERMES experiment. Due to a lack of quantitative predictions for the HERMES experiment, such effects could not be quantified. It is hoped that due to the powerful experimental method used to determine $\Delta G/G$, the method of measuring an asymmetry, NLO contributions could partially cancel in the polarized and unpolarized cross sections, leaving $A_{||}$ relatively unchanged.

Model	χ^2/d.o.f.
$\Delta G/G$ =constant (0.4)	4.5/4
$\Delta G/G$ =constant (0.0)	10./4
$\Delta G/G$ =constant (1.0)	27/4
GSA	4.3/4
GSB	4.3/4
GSC	13/4

Table 4.6: χ^2 test for several of the curves in Fig. 4-24. Also shown is the χ^2 for the assumption of a constant $\Delta G/G$ of 0.4.

4.10 Comparison to LO QCD phenomenological fits

The extracted value of $\Delta G/G = 0.41 \pm 0.18 \pm 0.03^{+0.42}_{-0.09}$, determined at $\langle x_G \rangle = 0.17$ and scale $\langle \hat{p}_T^2 \rangle = 2.1$ (GeV/c)^2, can be compared with a variety of LO QCD phenomenological fits to deep-inelastic scattering data on $g_1(x, Q^2)$.

In Fig. 4-24, the LO QCD fits of Ref. [47] for $\Delta G/G$ are compared with HERMES data for $A_{||}$. The fits were converted to $A_{||}$ using the "best" model in PYTHIA. In general, the fits agree quite well with the data. The reduced chi-squared χ^2_ν for each assumption for $\Delta G/G$ is displayed in Table 4.6. No model error was included for the calculation of χ^2_ν.

In Fig. 4-25, the extracted value of $\Delta G/G$ is compared with the fits of Refs [47, 48]. The range of x_G probed was determined to be roughly 0.06 to 0.28. This was based on the standard deviation of the x_G distribution seen in the Monte Carlo when the relevant p_T cuts were applied. Each p_T bin was found to probe roughly the same range of x_G.

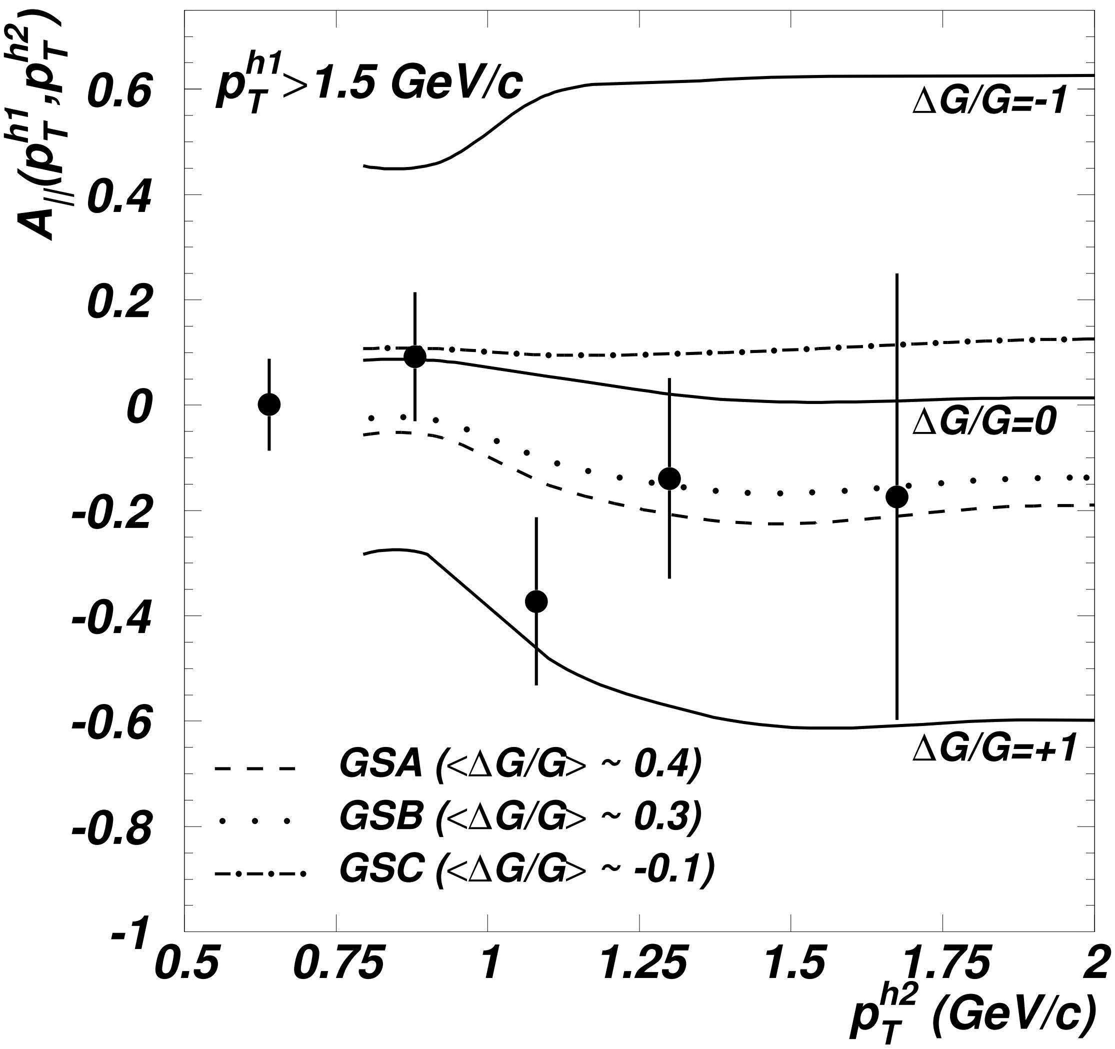

Figure 4-24: Comparison of measurements for $A_{||}$ with $\Delta G(x, \hat{p}_T^2)$ from Gehrmann-Stirling sets LO Gluon A (dashed), B (dotted), and C (dot-dashed) of Ref. [47]. Also shown are the positivity limits ($\Delta G/G = \pm 1$) and the curve for $\Delta G/G = 0$. The different models for $\Delta G/G$ are converted to $A_{||}$'s using the "best" model in PYTHIA.

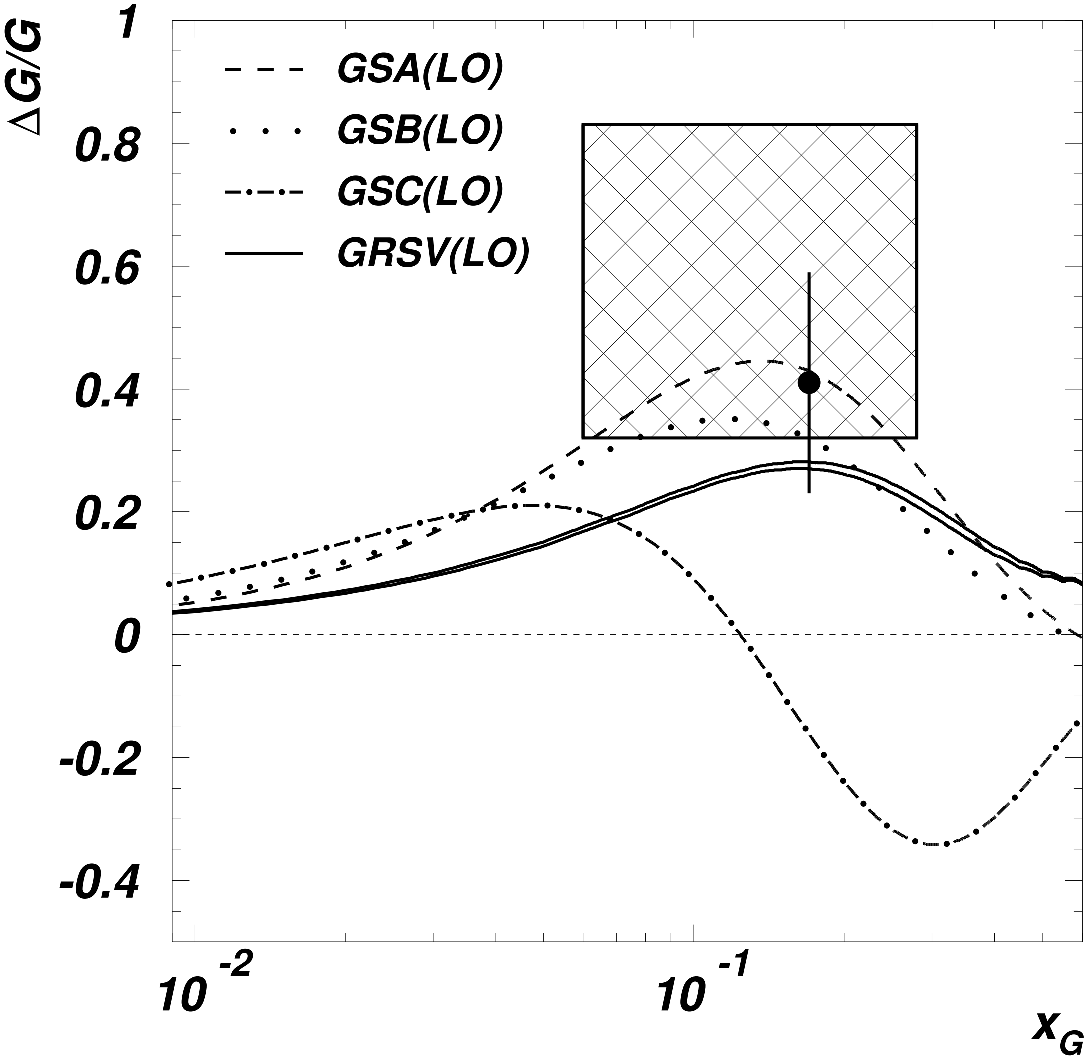

Figure 4-25: The extracted $\Delta G/G$ compared with phenomenological QCD fits to a subset of the world's data on $g_1(x, Q^2)$. The displayed error bar corresponds to the statistical and experimental systematic uncertainties added in quadrature. The height of the filled box corresponds to the model uncertainty, whereas the width corresponds to the range of x_G probed. The three GS curves are from Ref. [47]. The two GRSV curves shown correspond to the "standard" (upper) and "valence" (lower) scenarios of Ref. [48].

4.11 Future High-p_T Measurements at HERMES

In 1998 and 1999, HERMES has been running with a polarized deuterium target. In addition to collecting new data on spin asymmetries in charm production (described in section 1.4.1), HERMES will continue to study high-p_T photoproduction.

In May 2000, a long shutdown of the HERA machine is planned for a luminosity upgrade. HERMES will consequently be unable to take data and will concentrate on its own upgrades. When data taking resumes, HERMES plans to run with its target polarization oriented perpendicular to the beam polarization direction. This allows the study of other transverse structure functions of the nucleon which are independent from the longitudinal structure functions studied intensively by most DIS experiments so far.

It expected that by May 2000 HERMES will have accumulated roughly 2.5 million DIS events. This number can be compared with the number of DIS events accumulated in 1996 and 1997 and used to make a prediction of the ultimate May 2000 statistical precision with which HERMES will be able to determine $\Delta G/G$. For the data used by this thesis, 0.74 million DIS events were accumulated in 1996 and 1.47 million in 1997 giving a total of about 2.2 million DIS events. Simply rescaling the error bar on the current measurement gives an ultimate statistical precision of $\delta(\Delta G/G)^{2000}_{\text{stat.}} = 0.18 \times \sqrt{\left(\frac{2.5}{2.2+2.5}\right)} = 0.13$.

This is of course the simplest possible estimate. Should the asymmetry from deuterium be unexpectedly different from the data taken so far with the polarized hydrogen target, it may be discovered that QCDC background effects have been underestimated (as hinted by the leading particle effects currently observed in the asymmetry). New data from the FQS (also mentioned in section 1.4.1) will hopefully give a better understanding of photoproduction cross sections in general at HERMES.

Other possible reinterpretations of the result and the calculation of polarized NLO effects for the specific case of the HERMES experiment will hopefully be pursued by theoreticians. This will increase theoretical confidence in the result which is currently quantified in the rather large model dependence uncertainty.

Chapter 5

Conclusion

A measurement of the spin asymmetry in quasi-real photoproduction of hadron pairs at high transverse momenta was carried out by the HERMES experiment. For h^+h^- pairs with $p_T^{h_1} > 1.5$ GeV/c and $p_T^{h_2} > 1.0$ GeV/c, the measured asymmetry is negative with a value $A_{||} = -0.28 \pm 0.12$ (stat.) $\pm$ 0.02 (syst.). The cross section of hadron pair production in the same range of transverse momenta was also measured in order to provide additional information to compare with possible models of the photon at intermediate energies.

The cross section was demonstrated to be in relatively good agreement in shape with a simulation based on a LO QCD model implemented in the PYTHIA Monte Carlo generator. However, the cross section calculated with the "best" model with the HERMES tuned fragmentation parameters was found to be low by roughly a factor of two. The "best" model is the model that is expected to be the most complete representation of the data. To attempt to resolve this discrepancy, and to study the effect of possible missing processes, several Monte Carlo studies were carried. These studies entailed varying $\hat{p}_T$ cut-offs, adding hard hadronic photon processes, and varying fragmentation parameters and the intrinsic k_T of the quarks. A model dependence error was assigned on $\Delta G/G$ based on the variation of the extracted value on these effects. NLO effects have not been estimated but may turn out to be small for the measured asymmetry. Studies of leading particle effects and a comparison to a real photoproduction experiment were also conducted.

In the "best" model, in the region of phase space where the negative asymmetry is observed, the simulated cross-section is found to be dominated by the photon-gluon fusion process. A value of the gluon polarization has been extracted using this model: $\Delta G/G = 0.41 \pm 0.18$ (stat.) $\pm\, 0.03$ (exp. syst.)$^{+0.42}_{-0.06}$ (model) at $\langle x_G \rangle = 0.17$ and scale $\langle \hat{p}_T^2 \rangle = 2.1$ (GeV/c)^2.

Bibliography

[1] HERMES Collaboration, M. Amarian et al., The HERMES Charm Upgrade Program: A Measurement of the Double Spin Asymmetry in Charm Leptoproduction, DESY-PRC 97-037, January 1997.

[2] COMPASS Collaboration, Common Muon and Proton Apparatus for Structure and Spectroscopy, CERN/SPSLC 96-14, March 1996.

[3] PHENIX/Spin Collaboration, Proposal on spin physics using the RHIC polarized collider, BNL-PROPOSAL-R5, August 1992.

[4] R.D. Ball, S. Forte and G. Ridolfi, Phys. Lett. B378 (1996) 255.

[5] E154 Collaboration, K. Abe et al., Phys. Lett. B405 (1997) 180.

[6] SMC Collaboration, B. Adeva et al., Phys. Rev. D58 (1998) 112002.

[7] R.L. Jaffe, Phys. Lett. B365 (1996) 359.

[8] A. Bravar, D. von Harrach and A. Kotzinian, Phys. Lett. B421 (1998) 349.

[9] M. Fontannaz, D. Schiff and B. Pire, Z. Phys. C8 (1981) 349.

[10] A. Afanasev, C.E. Carlson and C. Wahlquist, Phys. Rev. D58 (1998) 054007.

[11] F. Halzen and A.D. Martin, Quarks and leptons: an introductory course in modern particle physics (John Wiley and sons, New York, 1984).

[12] T. Pussieux and R. Windmolders, Internal Spin Structure of the Nucleon: Proceedings, edited by V.W. Hughes and C. Cavata, p. 212, New Haven, CT, 1994, World Scientific, DAPNIA-SPHN-95-10.

[13] D. de Florian, C.A.G. Canal and R. Sassot, Nucl. Phys. B470 (1996) 195.

[14] H1 Collaboration, S. Aid et al., Nucl. Phys. B472 (1996) 3.

[15] H1 Collaboration, S. Aid et al., Nucl. Phys. B472 (1996) 32.

[16] ZEUS Collaboration, J. Breitweg et al., Z. Phys. C76 (1997) 599.

[17] ZEUS Collaboration, J. Breitweg et al., Phys. Lett. B407 (1997) 402.

[18] New Muon Collaboration, D. Allasia et al., Phys. Lett. B258 (1991) 493.

[19] H1 Collaboration, C. Adloff et al., Nucl. Phys. B545 (1999) 21.

[20] H1 Collaboration, C. Adloff et al., Z. Phys. C72 (1996) 593.

[21] M. Vanttinen and L. Mankiewicz, Phys. Lett. B434 (1998) 141.

[22] M. Vanttinen and L. Mankiewicz, Phys. Lett. B440 (1998) 157.

[23] F.J. Gilman et al., Phys. Lett. 31B (1970) 387.

[24] ZEUS Collaboration, J. Breitweg et al., Z. Phys. C75 (1997) 215.

[25] F. Meiβner, PhD thesis, DESY-Zeuthen, 1999.

[26] G.A. Schuler and T. Sjöstrand, Phys. Lett. B300 (1993) 169.

[27] G.A. Schuler and T. Sjöstrand, Nucl. Phys. B407 (1993) 539.

[28] European Muon Collaboration, M. Arneodo et al., Phys. Lett. B149 (1984) 415.

[29] T. Sloan et al., Phys. Rep. 162 (1988) 45.

[30] E665, M.R. Adams et al., Phys. Rev. D48 (1993) 5057.

[31] E665, M.R. Adams et al., Z. Phys. C71 (1996) 391.

[32] H1 Collaboration, S. Aid et al., Nucl. Phys. B449 (1995) 3.

[33] H1 Collaboration, C. Adloff et al., DESY-98-076, Eur. Phys. J. (in press) .

[34] ZEUS Collaboration, J. Breitweg et al., Eur. Phys. J. C1 (1998) 109.

[35] ZEUS Collaboration, M. Derrick et al., Phys. Lett. B348 (1995) 665.

[36] H1 Collaboration, C. Adloff et al., Eur. Phys. J. C1 (1998) 97.

[37] H1 Collaboration, C. Adloff et al., DESY-98-148, Eur. Phys. J. C (in press) .

[38] M. Anselmino, A. Efremov and E. Leader, Phys. Rept. 261 (1995) 1.

[39] B. Lampe and E. Reya, (1998), hep-ph/9810270.

[40] J. Ellis and R.L. Jaffe, Phys. Rev. D9 (1974) 1444; Phys. Rev. D10 (1974) 1669.

[41] R.L. Jaffe and A. Manohar, Nucl. Phys. B337 (1990) 509.

[42] S.J. Brodsky and F. Schlumpf, Phys. Lett. B329 (1994) 111.

[43] HERMES Collaboration, K. Ackerstaff et al., Flavor Decomposition of the Polarized Quark Distributions in the Nucleon from Inclusive and Semi-inclusive Deep-inelastic Scattering, hep-ex/9906035, Phys. Lett. (in press).

[44] B.E. Tipton, Measurement of Polarized Parton Distributions with Spin-dependent Deep-Inelastic Scattering, PhD thesis, Massachusetts Institute of Technology, 1999.

[45] EMC, J. Ashman et al., Phys. Lett. B206 (1988) 364.

[46] J. Ellis and M. Karliner, Phys. Lett. B341 (1995) 397.

[47] T. Gehrmann and W.J. Stirling, Phys. Rev. D53 (1996) 6100.

[48] M. Glück et al., Phys. Rev. D53 (1996) 4775.

[49] R.D. Carlitz, J.C. Collins and A.H. Mueller, Phys. Lett. B214 (1988) 229.

[50] G. Altarelli et al., Nucl. Phys. B496 (1997) 337.

[51] E.M. Kabuβ, Czech. J. Phys. 49/S2 (1999) 137.

[52] SMC, D. Adams et al., Phys. Rev. D56 (1997) 5330.

[53] N. Hayashi, Y. Goto and N. Saito, Proc. of the "6th International Workshop on Deep Inelastic Scattering and QCD (DIS 98)", p. 675, Brussels, Belgium, 1998.

[54] STAR Collaboration, T.J. LeCompte, Presented at 1996 Annual Divisional Meeting (DPF 96) of the Division of Particles and Fields of the American Physical Society, Minneapolis, MN, 10-15 Aug 1996, ANL-HEP-CP-96-97.

[55] A.D. Roeck and T. Gehrmann, Proc. of the "Workshop on Physics with polarized protons at HERA", p. 523, Hamburg, Germany, 1997, DESY-97-233.

[56] V.W. Hughes and A. Deshpande, Proc. of the "Proceedings of the 7th International Workshop on Deep Inelastic Scattering and QCD (DIS 99)", Zeuthen, Germany.

[57] V.A. Korotkov and W.D. Nowak, Proc. of the "Workshop on Polarized Protons at High Energies - Accelerator Challenges and Physics Opportunities", Hamburg, Germany, 1999.

[58] A.A. Sokolov and I.M. Ternov, Sov. Phys. Doklady 8 (1964) 1203.

[59] W. Lorenzon, Proc. of the Workshop "Polarized gas targets and polarized beams", edited by R.J. Holt and M.A. Miller, p. 181, Urbana-Champagne, USA, 1997, AIP Conf. Proc. 421.

[60] D. DeSchepper et al., Nucl. Instrum. Meth. A419 (1998) 16.

[61] J. Stewart, Proc. of the Workshop "Polarized gas targets and polarized beams", edited by R.J. Holt and M.A. Miller, p. 69, Urbana-Champagne, USA, 1997, AIP Conf. Proc. 421.

[62] T. Shin, The Structure Function Ratios and Flavor Asymmetry of Light Quark Sea, PhD thesis, Massachusetts Institute of Technology, 1999.

[63] HERMES Collaboration, K. Ackerstaff et al., Phys. Rev. Lett. 82 (1999) 3025.

[64] M. Kolstein, Exclusive ρ^0-Meson Electroproduction at HERMES, PhD thesis, Vrije Universiteit Amsterdam, 1998.

[65] M.F. Sutter, A Study of Spin Transfer in Fragmentation in the Leptoproduction of the Λ, PhD thesis, Massachusetts Institute of Technology, 1999.

[66] H. Kolster, The HERMES Gaseous Internal Polarized Proton Target and its use in the HERA Positron Storage Ring, PhD thesis, Ludwig Maximilians Universität München, 1998.

[67] C. Baumgarten, Proc. of "13th International Symposium on High-Energy Spin Physics (SPIN98)", Protvino, Russia, 1998.

[68] B. Braun, Proc. of the Workshop "Polarized gas targets and polarized beams", edited by R.J. Holt and M.A. Miller, p. 156, Urbana-Champagne, USA, 1997, AIP Conf. Proc. 421.

[69] J.W. Martin, "Results of Recent Low-α Running", HERMES Collaboration Meeting, August 1997.

[70] T. Shin, private communication.

[71] K. Ackerstaff et al., Nucl. Instrum. Meth. A417 (1998) 230.

[72] H. Avakian et al., Nucl. Instrum. Meth. A417 (1998) 69.

[73] T.A. Shibata et al., Nucl. Instrum. Meth. A411 (1998) 75.

[74] S. Bernreuther et al., Nucl. Instrum. Meth. A416 (1998) 45.

[75] W. Wander, Rekonstruktion hochenergetischer Streuereignisse im HERMES Experiment, PhD thesis, Universität Erlangen-Nuernberg, 1996.

[76] GEANT Detector Description and Simulation Tool, CERN Program Library, Long Writeup W5013, 1994.

[77] J.D. Jackson, Classical Electrodynamics (2nd ed.) (John Wiley and sons, New York, 1975).

[78] E.C. Aschenauer, Proc. of the "13th Lake Louise Winter Institute", edited by A. Astbury et al., p. 288, Lake Louise, Alberta, Canada, 1998, World Scientific.

[79] M.J. Amarian and A.E. Avetisyan, Low Momenta Charged Particle Identification with Time-of-Flight at HERMES, HERMES Internal Note 98-022.

[80] A.V. Airapetian et al., Time of Flight Technique for HERMES experiment, HERMES Internal Note 98-044.

[81] T. Benisch, Polarisierte Bhabha-Streuung und Luminositätsmessung im HERMES-Experiment, PhD thesis, Universität Erlangen-Nürnberg, 1998.

[82] W. Brückner, hermes.daq file, and private communication.

[83] W. Wander et al., Proc. of "Computing in High-Energy Physics (CHEP) '95", p. 18, Rio de Janeiro, Brazil, 1995, Additional information available at `http://www-hermes.desy.de/dad`.

[84] S.M. Fisher and P. Palazzi, The ADAMO Data System. Programmer's Manual - Version 3.2, CERN-ECP and Rutherford Appleton Laboratory, Additional information available at `http://www.cern.ch/Adamo`.

[85] B.E. Tipton, darKnight analysis code (dk).

[86] A.O. Mateos, Histogram and Test Package (HAT).

[87] HERMES Collaboration, A. Airapetian et al., Phys. Lett. B442 (1998) 484.

[88] B. Fox, ADAMO Data Definition Language file defining the structure of the version of μDST's used, and private communication.

[89] B. Bains et al., Preliminary Extraction of the g_1^p structure function from the 1996 HERMES polarized proton data, HERMES Internal Note 97-048.

[90] M. Amarian, Gluon Polarization from Spin Asymmetry of Correlated High-P_t Pions at HERMES, HERMES Internal Note 98-019.

[91] J.W. Martin, Photoproduction of High-p_T Hadrons at HERMES, HERMES Internal Note 98-039.

[92] M. Amarian, Systematic Study of Correlated High-P_t Events at HERMES, HERMES Internal Note 98-040.

[93] M. Amarian and J.W. Martin, Notes on "Measurement of the Spin Asymmetry in the Photoproduction of High-p_T Hadrons", Supplement to first draft of "Measurement of the Spin Asymmetry in the Photoproduction of High-p_T Hadron Pairs at HERMES", 1999.

[94] F. Meiβner, Measurement of the Total J/ψ Cross Section in Lepton-Nucleon Scattering at HERMES with the Data from 1995 to 1997, HERMES Internal Note 98-051.

[95] M.A. Funk, private communication.

[96] M.F. Sutter, private communication.

[97] T. Sjöstrand, Comp. Phys. Comm. 82 (1994) 74.

[98] P. Aurenche et al., Physics at LEP2, vol. 1, p. 291, Geneva, Switzerland, 1995, hep-ph/9601317.

[99] M. Glück, E. Reya and A. Vogt, Z. Phys. C67 (1995) 433.

[100] H. Plothow-Besch, Comput. Phys. Commun. 75 (1993) 396.

[101] HERMES Collaboration, A. Airapetian et al., Measurement of the Spin Asymmetry in the Photoproduction of Pairs of High-p_T Hadrons at HERMES, hep-ex/9907020, submitted to Phys. Rev. Lett.

[102] B. Lehmann-Dronke et al., Phys. Lett. B457 (1999) 207.

[103] A. Schäfer, private communication.

[104] M. Amarian, private communication.

[105] A.O. Mateos, genX toy Monte Carlo with interface to PEPSI polarized DIS physics generator. The analysis of this thesis uses PYTHIA, which had to be interfaced to the original genX code by JWM.

[106] E. Fermi, Z. Phys. 29 (1924) 315. C. F. Weizsäcker, Z. Phys. 88 (1924) 612. E. J. Williams, Phys. Rev. 45 (1934) 729.

[107] L. Mankiewicz, A. Schafer and M. Veltri, Comput. Phys. Commun. 71 (1992) 305.

[108] G. Ingelman, J. Rathsman and G.A. Schuler, Comput. Phys. Commun. 101 (1997) 135.

[109] V. Korotkov, private communication.

[110] F. Meiβner, Proc. of the "7th Int. Workshop on Deep Inelastic Scattering and QCD DIS99", 1999, HERMES Internal Note 99-028.

[111] S.D. Bass, S.J. Brodsky and I. Schmidt, Phys. Lett. B437 (1998) 417.

[112] M. Stratmann and W. Vogelsang, Phys. Lett. B386 (1996) 370.

[113] H. Ihssen, private communication.

[114] H.A. McL. Tallini, private communication.

[115] H.A. McL. Tallini, A Measurement of the Quark Spin Distributions of the Nucleon at HERMES, PhD thesis, University of Liverpool, 1998.

[116] Fermilab E706 Collaboration, L. Apanasevich et al., Phys. Rev. Lett. 81 (1998) 2642.

[117] L. Apanasevich et al., Phys. Rev. D59 (1999) 074007.

[118] S. Catani et al., JHEP 03 (1999) 025.

[119] D. de Florian and S. Frixione, Phys. Lett. B457 (1999) 236.

[120] D. de Florian and W. Vogelsang, Phys. Rev. D57 (1998) 4376.

[121] OMEGA Photon Collaboration, R.J. Apsimon et al., Z. Phys. C43 (1989) 63.

List of Figures

List of Tables